The Algol-type binary CX Draconis: numerical models of ultraviolet observations

A thesis submitted for the Degree

of

Doctor of Philosophy of the University of London

by

David Wonnacott

Department of Physics & Astronomy

University College London

University of London

1990

To the two wonderful people who taught me that if you reach for the heavens, you can have the stars.

To my parents.

...every strong intellect...is a guardian of integrity.

Dr. Jacob Bronowski — The Ascent of Man

Acknowledgements

It is my great pleasure to thank the following people, without whom this work would have been immeasurably lessened.

I should like to offer my sincerest thanks to Ian Howarth for the supervision he has bestowed upon me in the years since I set out to produce this thesis. It wouldn't have been the same without him. My grateful thanks also go to Raman Prinja, Ian's more-than-able stand-in during my third year, and to Professor Sir Robert Wilson who had the foresight to place me under their guidance.

Thanks too, go to Ian, Raman, Nicole, Julie, Dave P. and Keith for being such able proof-readers and spotters-of-mistakes, and to my friends and colleagues at U.C.L. and at R.A.L. for their time, sufferance and encouragement, notably Paul (atomic physics) and Mike (spectroscopy).

I must not fail to mention the indomitable squaddies from 'E3' (lately of 'A25'). Daily life with Keith, Des and 'Barry' was a permanent source of debate, education, fun and sticky buns. I could not have wished for more stimulating companions to pass my time with. I only hope that they remember me with the same fondness.

Finally, there are three people for whom I cannot express the full extent of my gratitude in words: Julie, my fiancée, who had (and still has) the soundness of mind to make me work when I really didn't want to and who was always there when I needed her to be, and my Mother and Father who have contributed to this thesis more than they could ever know and to whom I shall be more grateful than I can ever say.

Abstract

International Ultraviolet Explorer satellite spectra of the Algol-type interacting binary system CX Dra (B2.5 Ve + F?) have been analysed in detail, revealing a new phenomenon, to whit, CX Dra possesses a matter stream which at certain orbital phases disappears from the line-of-sight almost entirely. This has been dubbed 'stream dipping'.

Two possible alternative interpretations of these observations have been examined. Either the stream is undergoing a rapid change in its ionization balance, or the stream is collapsing towards the orbital plane as it gains speed. More complex models involving, for example, variable stellar winds or distortion of the stream trajectory by magnetic forces can be excluded to varying degrees by the velocity structure seen in the resonance lines.

Several scale-independent numerical models of interacting binary systems have been generated and applied to CX Dra in order to gain an insight into the geometry which is responsible for this effect. U Cep, with its well-known system parameters, has been used as a benchmark for the models. Those models with inviscid streams have failed to reproduce the observations, but the viscous streams, modelled using a cell-averaging technique, reproduce not only the observed velocity structure but the phase-dependency of the profiles too. Profile fitting then yields the chemical composition of the stream (these results indicate a high degree of CNO-processing), and allows a lower limit to be placed on the inclination of the orbital plane.

The density structure of the models has also been used to predict the variations

Attention is drawn to the inclusion of an addendum which contains the results of a detailed investigation into the properties and possible failings of the numerical model employed in this work, in particular to the non-conservation of angular momentum. The results derived from this model are, however, largely insensitive to this flaw.

Contents

List of Tables

List of Figures

Chapter 1

To Be or not to Be...

The gods did not reveal, from the beginning,
All things to us; but in the course of time,
Through seeking we may learn, and know things better.

Xenophanes

1.1 Introduction

Be stars are classified under the (admittedly broad) criterion of "non-supergiant B-type stars whose spectra have, or have had at one time, one or more Balmer lines in emission" (e.g. Collins 1987). They form a wide class of stars covering the temperature range B0 to B9, occasionally taking in O9 and A0 stars, constitute about 20 % of all B-type stars, and have a population peak near spectral type B2.5.

As their definition suggests, Be stars are primarily classified on the basis of the appearance of their visual spectra where some or all of the Balmer lines are in emission and typically have two peaks. This 'doubled' emission is subject to erratic variations on timescales ranging from minutes to decades (e.g. π Aqr, M^{c}Laughlin 1961). Further complications arise with the unpredictable appearance of sharp 'shell' absorption lines of some metals (predominantly Fe II) whose widths are small in

comparison with the very broad lines of the Balmer series. Be stars are also known to be abnormally rapid rotators for their spectral types (Slettebak 1976).

Early work on understanding these objects includes that of Otto Struve (1931), in which he proposed that the broad emission profiles were due to the observed rapid rotation of the Be stars. This rotation was supposed sufficient to trigger or enhance mass loss about the equatorial regions of these stars, thus creating and sustaining an elliptical, precessing ring of material of variable thickness which gives rise to both the variable hydrogen emission and, when optically thick, to the 'shell' lines. This concept, although now known to be considerably more complex than originally proposed, embodies the key elements of the generally-accepted, modern picture of an equatorially-confined disc of plasma girdling these objects.

The odd behaviour of Be stars is not restricted to the visual region of the spectrum. In the ultraviolet they exhibit anomalously high ionization stages for their photospheric temperatures, the former appearing as broad, outflowing 'wind' lines (e.g. Marlborough & Peters 1986), often with narrow components superimposed (Grady, Bjorkman & Snow 1987). Some Be stars are also X-ray sources[1] (e.g. γ Cas, Bradt *et al.* 1977). At lower energies, they often show large infrared excesses (Allen 1973) and are strongly polarized (up to 3 %, Jones 1979). 'Classical' Be stars have only recently been found to be very weak radio sources (Taylor *et al.* 1990), but Be-binaries were not detected in this survey.

The above definition of the Be class is not very specific and it is hardly surprising to find that it encompasses several different types of object which appear superficially similar. The Be phenomenon probably arises by one of (at least) two mechanisms: one taking place in single stars (the 'classical' Be stars) and another being associated with mass transfer from a binary companion. The division into these two groups arises because although it has been suggested that *all* Be stars are binary systems

[1] Be stars form two separate classes of X-ray sources: 'weak' sources with low X-ray luminosities, $L_X \lesssim 10^{33}$ erg s^{-1}, which appear as normal Be stars, and 'strong' sources, $L_X \gtrsim 10^{33}$ erg s^{-1}, which are known to be composed of a Be star and a neutron star in a binary system. Only the weak sources are the concern of this work.

(Harmanec & Křiž 1976), the population statistics of these objects are such that there are far too few *eclipsing* Be stars for all Be stars to be members of this class (Plavec 1976). Nevertheless, the presence of radial velocity shifts which repeat with a well-defined period in the spectra of some of this class of stars is strongly indicative that at least *some* Be stars are Be-binaries (e.g. HR 2142, Peters 1982).

Plavec (1987) has also pointed out that non-eclipsing Algol systems with primaries earlier than A0 would most likely be observed as Be stars, and in fact many Be-binaries are expected to occupy the same evolutionary niche as Algol systems, with an evolved, less luminous companion filling its Roche lobe and transferring processed material to a hotter and more massive main-sequence primary. (The naming convention used here is that the star which accretes the transferred mass will be referred to as 'the primary' whilst the mass-losing star will be called 'the secondary'). The mass transfer rate in these systems can be highly variable (sometimes changing by orders of magnitude) and so, by altering the structure of the circumstellar envelope, this leads to the erratic or episodic strengthening and fading of the Be $\rightarrow$ B $\rightarrow$ Be phases which are so characteristic of these stars.

This chapter will review the status of multi-wavelength observations of Be stars (and to a lesser extent of Algol systems) in some depth, making reference to some of the current weaknesses in the interpretation of the data where unrealistic or oversimplified models have been used. This will be followed by a description of the model of Be-binaries that is implied by the observations. The aims of this work will then be presented, the current state of understanding of the system under primary study, CX Dra, will be reviewed, and the purpose of each chapter in turn outlined.

1.2 The present state of play

1.2.1 The optical spectrum

For Balmer lines that are optically thin, the separation of the emission peaks gives twice the $v \sin i$ of the emitting part of the circumstellar disc (Huang 1972). This,

if assumed to be in a Keplerian orbit, gives an estimate of M_*/R_{disc}. Thus the double peaks are characterised by quite narrow velocity distributions, or equivalently, discs not much larger than the primary. Dachs *et al.* (1986) compute 'cylindrical', homogeneous disc sizes displaying this tendency in a number of Be stars including the binary ϕ Per. It might be expected that in reality the discs would be substantially larger than their primaries as they will certainly *not* have density distributions which are uniform, as assumed in the above analysis, and are likely to be spread more tenuously on their outer edges. This is in agreement with the ten Algol systems observed by Peters (1989) who showed from the disc eclipses that the Hα-emitting region fills a significant portion ($\gtrsim 90\,\%$) of the Roche lobes of the primaries.

1.2.2 The infrared spectrum

Extension of the optical continuum photometry into the infrared allows the photometric excesses there to be modelled. Gerhz, Hackwell & Jones (1974) by using spherical shells, and Dachs, Engels & Kiehling (1988) by using cylindrical discs, predict very similar emission measures ($E = \int_V n_e^2\, dV$) of $2.3 \times 10^{60}\,cm^{-3}$ (ϕ Per) and $1.1 \times 10^{60}\,cm^{-3}$ (HR 2142) respectively. The former group also show from the slope of the infrared continuum that the excesses are due to free-free emission; the possibility of significant thermal emission from dust grains is excluded as no 'dust features' are observed near $10\,\mu m$.

Infrared photometry by Ashok *et al.* (1984) has shown that the emitting volume of the infrared radiation is much larger than that of the optical (e.g. $V_{IR}/V_{H\alpha} \sim 12$ for ϕ Per).

Most significantly, perhaps, the work of Waters, Coté & Lamers (1987) with *IRAS* data extending out to at least $60\,\mu$m, has shown that the mass loss rate from Be stars as seen in the infrared is up to a hundred times greater than that observed in the ultraviolet. They postulate a wind which escapes freely from the polar regions of the star at a rate $\dot{M}_{UV} \sim 10^{-9}\,M_\odot/yr$, and a cylindrically-symmetric equatorial disc through which material flows at a rate of $\dot{M}_{IR} \sim 10^{-7}\,M_\odot/yr$. This model could

obviously apply to the accretion disc in an interacting binary system as well as to a lone, 'classical' Be star, but it should be remembered that the infrared outflow is an assumption of their model rather than an observational fact. The infrared excesses only measure the *amount* of circumstellar material, not its velocity structure.

1.2.3 The radio frequencies

Taylor *et al.* (1990) have very recently completed observations of a sample of Be stars at 2 cm. They conclude that the typical size of the emitting volume is generally of the order of $100\,R_{\odot}$, continuing the trend noted by Ashok *et al.* (1984) of larger emitting volumes being seen at longer wavelengths; this being most probably due to the circumstellar material becoming optically thick to longer-wavelength emission at larger stellar distances. Further, they postulate that their observed lack of radio-active Be-binaries is due to the disruption of the large emitting volume by tidal action of the companion.

1.2.4 The ultraviolet spectrum

The majority of Be stars are of earlier B-types and emit most of their flux in the ultraviolet, making this spectral region particularly important for the study of these objects, principally because the resonance transitions of C^{3+}, N^{4+}, Si^{3+}, and Al^{2+} appear there.

Snow, Peters & Mathieu (1979) have compared *Copernicus* scans of Be and shell stars with those of supergiants and point out considerable similarities, notably, the large number of Fe II lines present. They remark that, in supergiants at least, these lines could be indicators of extended atmospheres, a result which agrees well with the canonical picture of Be stars' envelopes.

Studies of the wind structure of Be stars using *IUE* observations show that the wind lines observed in hotter stars (e.g. N V, C IV *etc.*) persist to much later spectral types and are stronger than in normal B stars, and also that the wind profiles appear to arise increasingly from 'blobs' with a discrete, rather than a continuous,

distribution of velocities. The first of the aforementioned observations would be a natural consequence of an impacting stream in a close binary system, whilst the turbulence thus caused could easily produce 'blobs' of material moving with discrete velocities. Such effects are readily seen in Algol systems; for example, U Cep has been extensively observed by Kondo, M^{c}Cluskey & Stencel (1981) who show many profiles of Mg II which exhibit the above properties more or less continuously in time.

1.2.5 The X-ray spectrum

There is a paucity of work in the X-ray region on both Be stars and on Algols (Bolton 1989). What little research has been done seems to indicate that the source of the X-rays in these objects, at least in the Be-binaries, is the chromospheric activity of the late-type secondary. This is presumed to be due to enhanced dynamo action caused by the synchronous rotation of the secondary.

Simple computations by Harnden *et al.* (1977) indicate that the matter stream which is thought to be present in Algol (β Per) can easily penetrate the photosphere of the primary if the mass transfer rate is greater than $\dot{M} \sim 10^{-9}\,M_{\odot}/yr$. If the shock front does form at depth in the primary's outer layers, then it is quite reasonable to expect the X-ray emission to be substantially blanketed by the overlying material (e.g. a column of hydrogen $\lesssim 0.1\,R_{\odot}$ at a density of $n_{H} \sim 5 \times 10^{10}\,cm^{-3}$ would be sufficient to absorb most of the soft X-rays; Fireman 1974). Even so, this shocked region could be an important source of the highly-ionized species observed in the ultraviolet, as Auger ionization turns N^{+2} into N^{+4} and C^{+1} into C^{+3}, followed by turbulent mixing to the surface. The short recombination times in a region of such (relatively) high density argue against much N^{+4} or C^{+3} reaching the surface, but as the details of the geometry and the energy deposition by the stream are highly uncertain, this mechanism cannot be entirely discounted.

1.2.6 Polarimetry

Coyne & McLean (1982) stress that "The mere fact that the optical radiation from Be stars is observed to be intrinsically linearly polarized provides perhaps our most conclusive clue that the circumstellar shells of these stars are disklike in nature". Strong variations in the polarization are often observed, and this can be attributed most naturally to the perceived (or real) changes in the structure of the circumstellar material as the stars rotate past on their axes (in the case of 'classical' Be stars) or progress along their orbital paths (as in Be-binaries). Models of circumstellar discs are often invoked (Rudy & Kemp 1976, 1978) but no-one has yet explicitly attempted to allow for the effects of a gas stream on the polarized light from an interacting binary. Typical derived parameters are $R_{disc} \sim 5\,R_*$ and $n_e \sim 10^{11}\,\mathrm{cm}^{-3}$.

1.2.7 Evolutionary status

Interpretation of the position of Be stars on the H-R diagram is hampered by the fact that rapid rotation can, via gravity-darkening of the star's distorted atmosphere, move a Be star away from the Zero-Age Main Sequence (Collins & Sonneborn 1977). Many Be stars are also found to be intrinsically reddened (e.g. Mermilliod 1982), presumably due to their extended circumstellar envelopes. Be stars have been found everywhere between the ZAMS and the giant region, appearing on average between 0.5 and 1.0 magnitudes above the Main Sequence. As mentioned before, they are very abundant comprising $\sim 20\,\%$ of all B-type stars, and they closely follow the spatial distribution of normal B stars. However, this preponderance of Be stars has not served to elucidate their evolutionary status as a group of objects. Nevertheless, for the case of Be-binaries formed from a Be star and a late-type giant or subgiant, a strong case can be made for believing that they are equivalent to non-eclipsing Algol-type systems (as discussed in section 1.1), especially as the apparent lack of eclipsing Be-binaries could be due to their classification as Algol systems.

1.2.8 The Be Phenomenon as the product of binary star interaction

The circumbinary material, as proposed above, divides naturally into three components: the stream of matter from the inner Lagrangian (L1) point down onto the primary, the impact zone over which the effects of the photospheric impact are felt, and the circumprimary accretion disc (if one forms).

The stream consists of material which evaporates from the Roche Lobe of the secondary and is accelerated down into the gravitational well of the primary. The speed of the gas rapidly becomes hypersonic (Mach numbers of the order of 20–40 are expected) and by the time the stream strikes the primary, it is highly ionized by numerous interparticle collisions and turbulent shocks.

The impact zone is the region of the primary's surface where the stream will deposit most of its kinetic energy and, as the stream is travelling with a significant fraction of the escape velocity of the star (many hundred km/s), this amounts to a substantial injection of mechanical energy into the photosphere. The X-ray emission from Be-binaries may be produced in this region (and by coronal activity in the secondary, if there is any), but the object itself may not appear X-ray-bright if the circumstellar material is rich in metals and/or dense enough to blanket the radiation. This region is also likely to be very bright in the ultraviolet and optical, and further ionization can occur locally. The effects of this extra heating on the photosphere are unknown. Ulrich & Burger (1976) attempt a simplified analysis and conclude that apart from a small increase in radius, the primary is unaffected. However, they omit several important processes which are certain to have an effect, such as the input of angular momentum into the photosphere of the accreting star.

If, by some combination of viscous and geometric effects, the stream is able to avoid complete accretion onto the primary, an accretion disc can form. The outer disc is likely to rotate with an approximately Keplerian velocity profile and so give rise to the Doppler-broadened emission and absorption lines, and the viscosity of the plasma will cause the material to spiral in and join the primary. The shape and

width of the ultraviolet resonance lines are the product of the stream impact and of turbulence, the observed polarization arises automatically from electron scattering in the flattened geometry of the disc, and the large number of absorptions in the plasma will reprocess the radiation to lower energies (via bound-free and free-free interactions) to produce the infrared excesses seen in Be-binaries.

1.3 Summary and aims

Be stars, both single and in binary systems, have been studied at almost all wavelengths for decades, yet no definitive model(s) exist for these objects. Much has been made of general arguments in deducing the structure of the flattened distributions of circumstellar material, but in terms of obtaining accurate values of the physical parameters that describe the non-stellar material about Be stars, to date only simplified models have been tested against the data (e.g. Lubow & Shu 1975). Whilst the usefulness of these models cannot be denied, there is a definite need to improve on them as modern observations become more precise and make more demands on theory. Only the work of Prendergast & Taam (1974) deals with mass transfer in Algol systems in sufficient detail to be properly tested against the observations. Unfortunately, the details of the calculations have never been published in full.

The aim of this work is to produce credible models of Be-binaries which are detailed enough to be used to extract reliable and meaningful information from data obtained in a variety of ways. By focussing attention on the reduction of the data for a single, relatively-unstudied Be-binary, CX Draconis, the continuity of the analysis has been maintained and the adopted requirement that the models be rigourously tested on systems with more firmly-known parameters, has ensured that both models and methods retain a high degree of flexibility.

1.4 CX Draconis

CX Draconis (HD 174237, B2.5 Ve + F?) was first listed as a Be star in 1949 by Miczaika in a spectrographic study of selected Be and Ae stars. Lacoarret subsequently reported rapid spectral variations in 1962. In 1978, Koubský gathered sufficient spectroscopic observations to identify it as a binary and deduce a period of $6.^{d}69728$. The period was later revised slightly to $6.^{d}69606$ (Koubský *et al.* 1980). He also attributed the variations seen in Hα and other species to matter streaming from the (unseen) cool companion onto the B star. The scatter in the radial velocity curve is almost as large as the velocity variations themselves and certainly suggest that a strong, erratic source of absorption and emission is present, superimposed on the more regular stellar motions. If such a stream exists, it must be highly variable or give rise to some circumstellar structure which is only quasi-static.

This variability has been demonstrated to occur on widely different timescales by Percy *et al.* (1988) who undertook long-term *BV* monitoring of selected Be stars. They observed CX Dra over two seasons of 50 and 70 days and noted random variations with an amplitude of about $0.^{m}1$ in both B and V in one season, and, in complete contrast, they observed a smooth decline of about $0.^{m}2$ in both magnitudes a year later.

Only one study of any depth exists of CX Dra in the ultraviolet. Peters & Polidan (1984) used *IUE* spectra taken at various phases to deduce the presence of a low-density, high-temperature ($n_e \sim 10^9\,\mathrm{cm}^{-3}$, $T_e \sim 10^5\,\mathrm{K}$) region located on the trailing hemisphere of the primary, probably caused by the impact of the matter stream. Their phase coverage is incomplete however, and so their investigation of the circumstellar material is restricted to one half of the orbital cycle between $\phi \sim 0.4$ and $\phi \sim 0.9$.

Apart from the near-infrared measurements of Schuster & Alvarez (1983) which indicate an infrared excess, the only measurement of the far-infrared spectrum of CX Dra comes from the *IRAS* survey at 12 μm where an excess of $+1.^{m}06$ was found (Coté & Lamers, 1987). These, in addition to the visual excess of $E(B-V) = 0.^{m}05$,

make the case for the presence of circumstellar material is quite compelling.

Einstein observations of CX Dra (Guinan, Koch & Plavec 1984) are best fitted by a thermal bremsstrahlung source of X-rays with a characteristic temperature of 9.6×10^6 K. No short-timescale variations (between 6 and 30 minutes) are seen, and as the X-ray luminosity, $L_X \sim 10^{31}\,\mathrm{erg\,s^{-1}}$, is comparable to the X-ray luminosity of single late-type stars, it is probable that the principal source of the X-rays in CX Dra is coronal activity in the secondary rather than hot shocks in the accreting stream. Very similar results have been found for Algol (White *et al.* 1986) and the identical conclusion is confirmed by the absence of an X-ray eclipse in this system.

CX Dra has only recently been observed polarimetrically and substantial variations in both the degree of polarization and in the position angle have been found (Huang, Hsu & Guo 1989).

1.5 Thesis outline

Chapter 2 attempts to obtain the parameters describing the orbital motion of CX Dra using radial velocity curves derived from various ions present in the *IUE* SWP spectral range ($\lambda\lambda$ 1150–2000). Disturbances in the profiles of many lines of differing ionization potential are found to distort the orbital solution from that expected on the grounds of physical arguments. To overcome this problem, spectra of CX Dra with the disturbed lines removed are cross-correlated with the spectrum of a standard star, thus utilizing the information in the whole binary spectrum and producing a much more reliable solution. The solution is used to correct the velocity shift of the standard relative to CX Dra prior to division of the spectra to produce 'stream only' profiles which are then examined for the effects of the streaming matter alone. A physical model of the mass distribution is discussed.

In chapter 3, a simplified model of mass transfer based on three-body motion is compared to the data. An acceptable fit is found for the radial velocity curve deduced from Fe III lines, but it is shown that whilst the fit agrees with the observations, it does not constrain them sufficiently to produce a reliable solution. In fact, it implies

a contradictory set of physical properties for the primary and secondary. On these grounds the simple model is rejected.

Chapter 4 extends the simple models using a hydrodynamic, viscous treatment to simulate the spreading of material by the viscous transport of linear and angular momenta. The model is tested successfully against the interacting binary system U Cep, and the model of CX Dra is found to be in good qualitative agreement with a general model deduced from the *IUE* observations.

Chapter 5 deals with the application of the models of chapter 4 to the problem of the distortions observed in the profiles of atomic transitions occurring in the ultraviolet. Two extreme models of the radiation transfer are tested; the absorption model being rejected, the scattering model being preferred. Line profiles are fitted to many of the available lines in the observations of CX Dra to deduce a strong limit on the inclination of the orbital plane of the binary system, to infer the spatial distribution of ionization and to obtain the chemical abundances of several important elements from a model of the ionization balance. The quality of the profile fits increases confidence that the model is correct.

Chapter 6 is concerned with the analysis of polarimetric data. Using the models of chapter 4, predictions of polarization variations are compared with the data for CX Dra. Interpretations are aided by comparison with polarization data from other known systems (Algol and U Sge). The models are appropriately revised and recalculated before being fitted to observations of several systems to derive parameters related to the geometry of the systems and to their mass transfer rates.

In chapter 7, the derived data on CX Dra are reviewed and discussed, as is the usefulness of the models and techniques used, and the potential for extending this work to a whole range of objects.

Chapter 2

IUE observations

> ...the spectroscope, to which he had at once resorted, indicated a mass of flaming gas, mostly hydrogen, moving with enormous velocity...
>
> *H. G. Wells — The War of the Worlds*

2.1 Introduction

Several important phenomena of interacting binary systems are visible in the ultraviolet region of the spectrum, making *IUE* a particularly powerful tool for their study. Many of the primaries of interacting binary systems are early-type stars which emit most of their flux in the *IUE*-sensitive region. Another important aspect of their ultraviolet spectra lies in the appearance of particular ground-state transitions of many-times ionized species, specifically, the resonance transitions of the so-called superionic states which often require temperatures far in excess of the available photospheric temperatures to produce them (e.g. N V does not appear in normal B-stars later than B0 V, an effective temperature of $\sim 30\,000$ K, but it *is* seen in B2.5 Ve stars). Superions found within the *IUE* spectral range are given below in table 2.1.

N V	$\lambda\lambda$ 1238.81, 1242.80
Si IV	$\lambda\lambda$ 1393.76, 1402.77
C IV	$\lambda\lambda$ 1548.20, 1550.77
Al III	$\lambda\lambda$ 1854.72, 1862.78

Table 2.1: *Superion lines observable with IUE.*

Since these transitions are observed to be quite strong in stars whose temperatures are too low to produce them by normal thermal processes, there must be some other non-thermal process(es) operating. Superions can easily be manufactured by collisional ionization, so it may be supposed that the binary system in question has a region where the plasma is strongly shocked or mechanically heated in some, as yet unspecified, manner.

The analysis of this chapter is concerned with gaining some insight into the velocity structure of the superionized regions and of their overall geometry. To do this, a baseline for comparison is required; this will be the binary motion of the primary. Subsequent analysis will use the observed variations in the orbital characteristics (e.g. phase lags, velocity semi-amplitudes, eccentricities) to derive a self-consistent geometry for CX Dra. Furthermore, an attempt will be made to isolate the structure of the high-energy region more precisely by removing the photospheric contribution to the line profiles.

2.2 Reduction of the *IUE* data

In total, forty short-wavelength (SWP), high-dispersion spectra of the binary system CX Dra were recovered from the World Data Centre archive spanning the period

from March 1980 to October 1986 (see appendix B).

The data were reduced using the STARLINK software package IUEDR (Hook & Giddings 1985; Rees 1987). The appearance of scattered light in the spectrograph and in the échelle inter-order overlap was corrected for by setting the cores of the Lyα lines to be completely black (some geocoronal emission was noted but this was also dealt with as above). The order-dependent wavelength shifts were removed by forcing the wavelengths of several interstellar lines (N I λ1220, Fe II λ1608, Si II λ1808) to have their laboratory values, thus placing them at rest.

2.3 The velocity-phase variations

Preliminary examination of the data indicates that there is a great deal of time-variation in the structure of many of the line profiles of CX Dra, notably in the metastable Fe III lines near 1900 Å, and in the lines of the superionized species (N V, Si IV, C IV and Al III).

The velocity shifts of the centre of the profiles of these ions at half their depth were measured (by eye) using the STARLINK package DIPSO (Howarth & Murray 1987) and were found to be repeatable to within 3 km/s. The velocities of the Si III line at λ1296 were obtained for comparison with the other lines. It was expected that this line and the neighbouring Si II/Si III features near 1300 Å are formed in the photosphere of the primary and so should be useful for extracting the binary motion. The resultant velocity curves are shown in figures 2.1, 2.2, and 2.3. N V and C IV have not been included in figure 2.3 as their profiles become very shallow at some phases, making the velocities hard to determine; their behaviour is, however, entirely consistent with by the motions seen in the other superions. Superimposed on these figures is the binary orbital solution of the Si III data as computed by the program STERNE II (Dworetsky 1989). The Heliocentric Julian dates of each observation were computed from the *IUE* spacecraft logs and are accurate to $\pm 1^s$, but the images are 'smeared' over the 300^s exposure time. The phases of the velocity curves, ϕ_{UV}, are derived from the period obtained from the fit; the orbital parameters

	This work	Koubský (1978)
Period, P	$6.^{d}6935 \pm 0.^{d}0011$	$6.^{d}69827 \pm 0.^{d}00005$
Epoch of primary minimum, E_0 (HJD − 2440000)	4326.9 ± 0.4	2181.79 ± 0.14
Eccentricity, e	0.53 ± 0.14	0.0
Systemic velocity, γ (km/s)	-0.8 ± 3.9	-2.27 ± 0.81
Velocity semi-amplitude, K_1 (km/s)	33.5 ± 4.5	35.6 ± 1.2
Primary orbital radius, $a_1 \sin i\,(\mathrm{R}_\odot)$	3.77 ± 0.63	4.716
Longitude of periastron, ω	$-11.^{o}2 \pm 16.^{o}5$	—

Table 2.2: *Si III* λ 1296 *orbital parameters of CX Dra.*

and their standard errors are presented in table 2.2. The residuals on the fit have a standard deviation of 15.51 km/s.

The photospheric velocity curve shows a periodic variation which is moderately accurately repeated over many ($\sim$ 350) cycles. Both the period, P, and the velocity semi-amplitude, K_1, agree well with parameters based on helium-lines in the optical region (Koubský 1978). Subsequent re-analysis of these data (Koubský 1980) leads to a downward revision of the 1978 period to $6.^{d}69606$, in closer agreement with the above orbital solution. The centre-of-mass velocities are not expected to agree, however, because the *IUE* wavelength (and hence velocity) scale has no accurate absolute (i.e. rest-frame) calibration for spectra such as these which were taken through the large aperture. The value for the primary orbital radius is in reasonable agreement with that of Koubský, bearing in mind that the eccentricity is not equal to zero. The two seriously *discrepant* parameters are the epoch of primary minimum (defined by Koubský as the time of superior conjunction of the primary with the

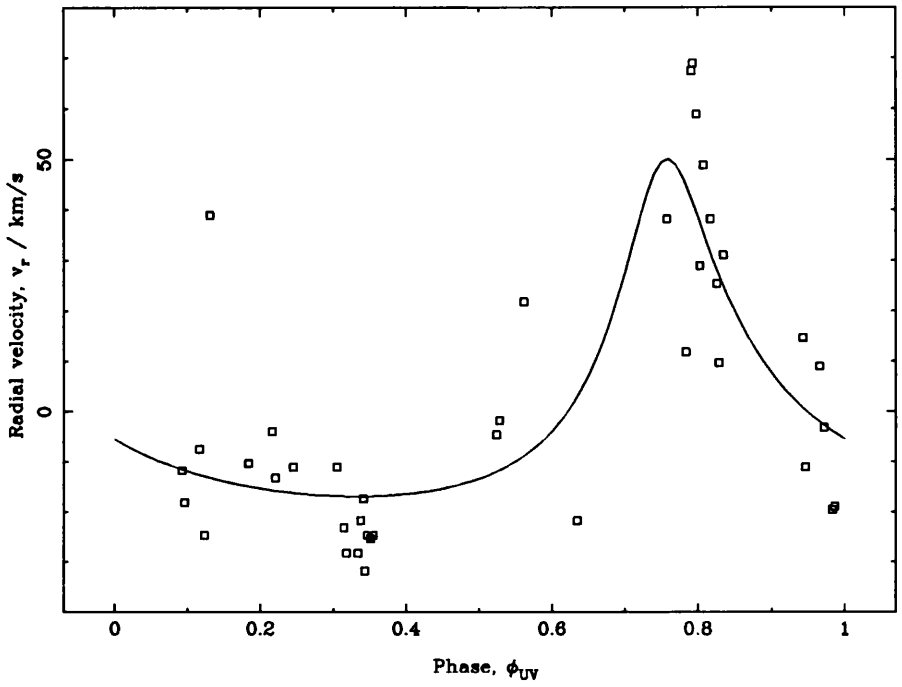

Figure 2.1: *Fitted radial velocity curve to CX Dra Si III* λ 1296 *velocity data.*

secondary), and the non-zero eccentricity of the orbit. The eccentricity of CX Dra is expected to be very close to zero because of tidal circularization of the stellar orbits in this close binary system occurring on timescales much shorter than the evolutionary timescales of the stars (Zahn 1966; Tassoul & Tassoul 1990 and references therein). However, the derivation of both the eccentricity and the epoch of primary minimum are almost certainly affected by absorption by circumstellar material which distorts the line profiles.

Comparison of the Fe III velocity measurements with the determined Si III orbit (figure 2.2) shows very poor agreement, yet two important details are immediately apparent. Firstly, the Fe III velocity variation is generally several times greater than the velocity semi-amplitude of the Si III curve and secondly, the maximum Fe III velocity *lags* the Si III value by 0.25 in phase. Clearly, the Fe III lines have a substantially different origin to the Si III lines.

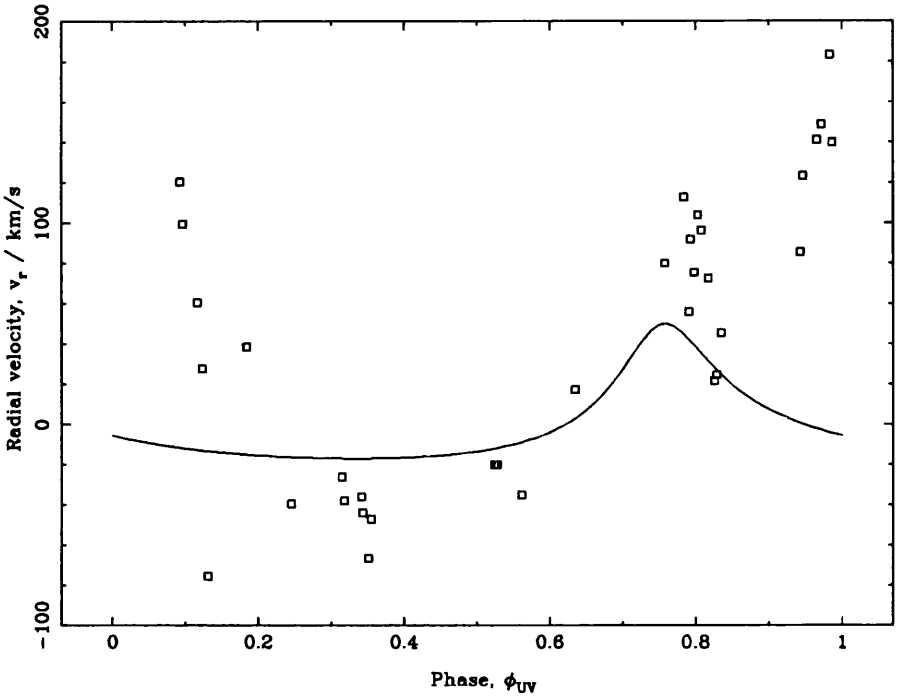

Figure 2.2: *Fe III* λ 1895 *data from CX Dra with Si III solution curve for comparison.*

Deviations of Si IV and Al III from the Si III curve (figure 2.3) are even more extreme. The superions maintain the same period and phasing as the Fe III but they vary from deep, narrow profiles to shallow broad ones, they do not maintain their equivalent widths, implying a considerable range of column densities, and near $\phi_{UV} \sim 0.3$ they exhibit multiple components with very strong blueshifts.

This effect, whereby different geometries (e.g. eccentricities) are seen in different ions, is not unknown; Niemela & Sahade (1980) derived orbital eccentricities between 0.24 and 0.5 for the WR binary γ^2 Vel and attribute this variation to the massive stellar wind which pollutes the line profiles. Light-curves of U Cep, an eclipsing Algol system, have yielded values for its eccentricity ranging from 0.20 to 0.47 (see Batten 1974 for a review). This has been attributed to a ring or disc of circumstellar material about the primary (Struve 1944), which is responsible for the distortion of the light-curve when, in fact, the orbit has an eccentricity which is close to zero.

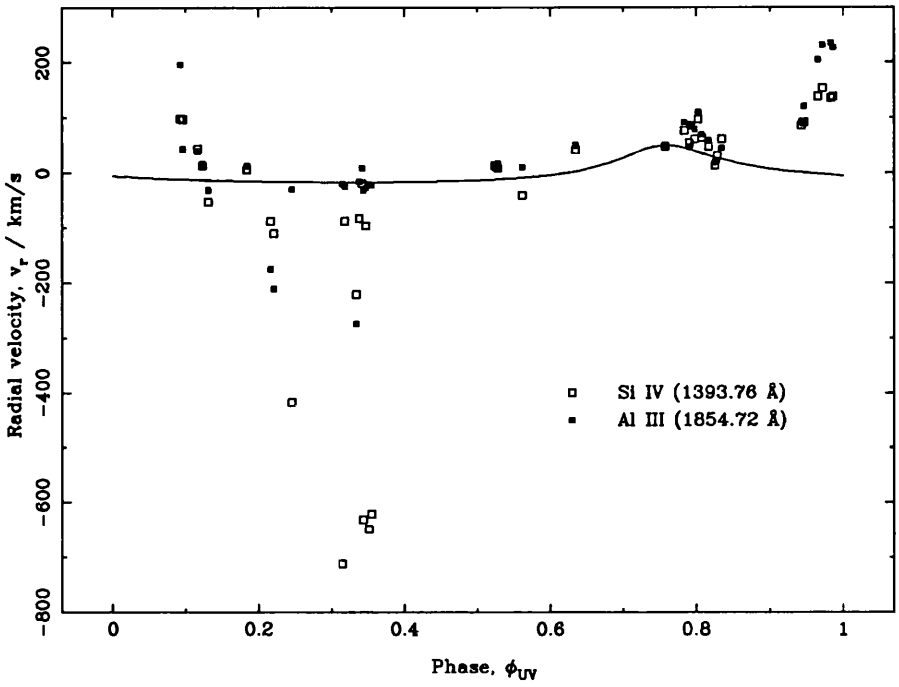

Figure 2.3: *Superion data from CX Dra with Si III solution curve. Notice the large blueshifted feature in* both *superions.*

Both the overall appearance of the velocity-phase curves of the higher-ionization species, and the magnitude of the velocities involved (some of which are probably greater than the escape velocity of the system), make it unlikely that the observed variations are due to simple binary motion; coupled with the peculiar phasing of the blueshifted feature, the supposition that profile distortions are due to, say, an isotropic wind from the primary, is improbable. To pin down the source of these effects more accurately, a more detailed view of the velocity structure and geometry of the circumstellar material (CSM) alone is required.

2.4 Extraction of the stream profiles

To gain a clearer picture of the velocity structure of the CSM alone, the photospheric contribution must be removed. To do this properly would require the deconvolution of the photospheric source function from the total flux integral. In practice, this is impossible and something less rigorous must be settled for. It is assumed, therefore, that the CSM acts like a simple, plane-parallel slab of absorbing material, producing no emission, and with no radiative coupling to the photosphere. Thus, given a suitable reference photosphere, it may be divided out of the total profile to yield, at least to first order, the line profile due only to the CSM.

The secondary of CX Dra is given the spectral type of F5–G0 by Peters & Polidan (1984) and a value of $T_{\rm eff} \sim 6500\,{\rm K}$ by Guinan, Koch & Plavec (1984), based on the thirteen-colour photometry of Shuster & Alvarez (1983). This means that it will not contribute significantly to the ultraviolet spectrum of CX Dra, leaving only the spectrum of the primary to be matched and removed.

2.4.1 The choice of the standard

The list of MK standard stars (Morgan & Keenan 1973) includes several which have been observed by *IUE*. From these, three were chosen to bracket the expected spectral type of CX Dra (B2.5 Ve): 22 Sco (B2 V), σ Sgr (B2.5 V), and η Aur (B3 V). Comparison of the photospheric regions of each of these spectra with CX Dra, showed that σ Sgr provides the best agreement with CX Dra (see figures 2.4 and 2.5), both in terms of their spectral types and their rotational velocities ($v \sin i$ = 180 and 201 km/s for CX Dra and σ Sgr respectively): σ Sgr was therefore adopted as the standard for comparison.

Seven SWP images of σ Sgr were acquired from the World Data Centre Archive, processed as above, rectified, and merged to increase the S/N using their exposure times as linear weights.

It is important that the standard spectrum is accurately aligned with each CX Dra spectrum prior to division. To achieve this most reliably, the template

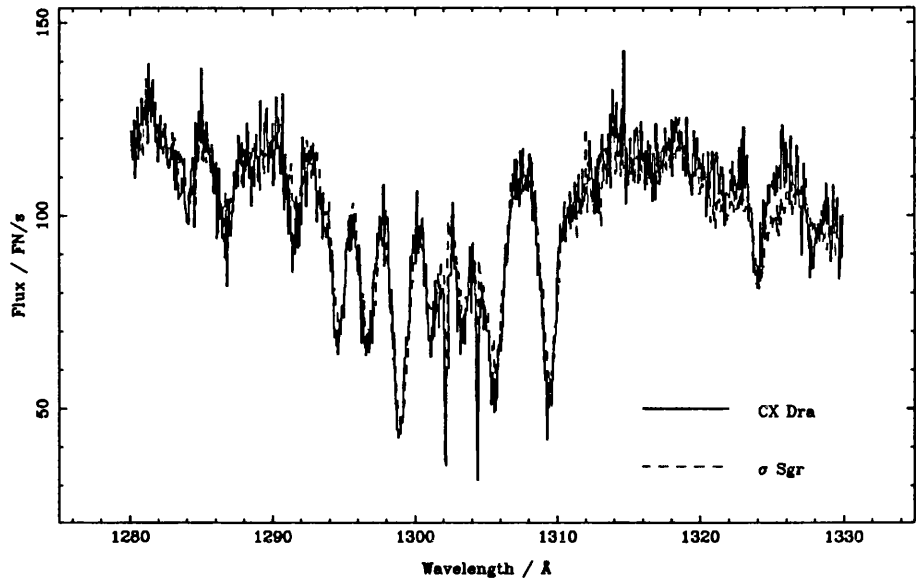

Figure 2.4: *A comparison between the silicon photospheric feature in CX Dra and the standard σ Sgr.*

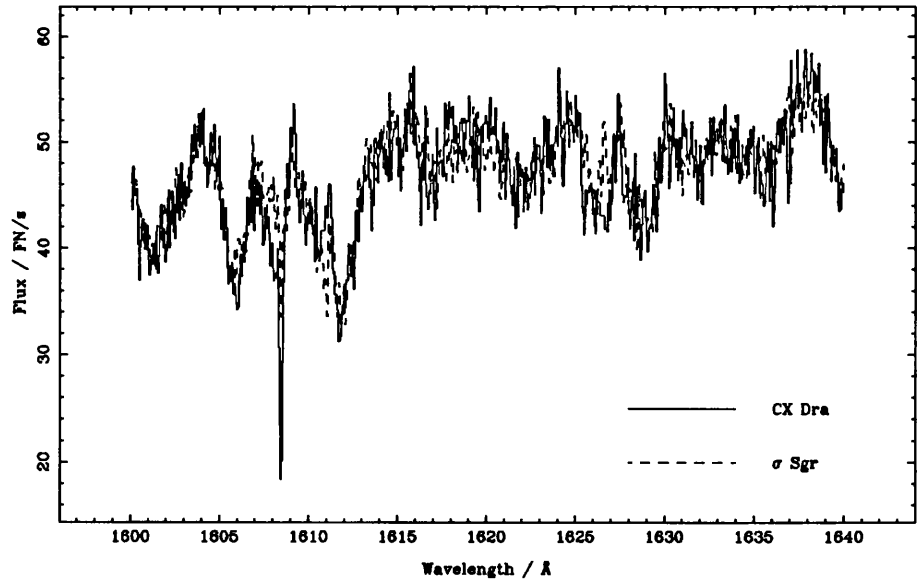

Figure 2.5: *A comparison between a photospheric region in CX Dra and the standard σ Sgr.*

	This work	Koubský (1978)
Period, P	$6.^d6946 \pm 0.^d0019$	$6.^d69827 \pm 0.^d00005$
Epoch of primary minimum, E_0 (HJD − 2440000)	4329.4 ± 0.3	2181.79 ± 0.14
Eccentricity, e	0.07 ± 0.15	0.0
Systemic velocity, γ (km/s)	-13.1 ± 3.2	-2.27 ± 0.81
Velocity semi-amplitude, K_1 (km/s)	30.0 ± 4.3	35.6 ± 1.2
Primary orbital radius, $a_1 \sin i\,(R_\odot)$	3.96 ± 0.57	4.716
Longitude of periastron, ω	$-71.^\circ5 \pm 68.^\circ8$	—

Table 2.3: *Cross-correlation orbital parameters of CX Dra.*

and subject spectra were cross-correlated using the IUEXCOR program of Rees (1987). To maximize the efficiency of the program, all lines which are obviously non-photospheric in origin (e.g. interstellar lines, superions etc.) were removed. This helps to ensure that it is the photospheres that are compared, with as little contamination as possible. The derived relative shifts can also be used to extract the binary motion of the primary (relative to the template) and hence provide a more reliable check on the orbital parameters than those found from the profiles of an individual line. The data in table 2.3 are from an orbital fit to the cross-correlation shifts; the residuals from the fit have a standard deviation of 15.37 km/s.

As before, the period and the velocity semi-amplitude are in excellent agreement with both Koubský (1978, 1980) and the previous results based on Si III velocities. The systemic velocity is only a measure of the mean velocity shift between the ISM lines in the template and the data and should not be expected to agree with other observations, and the longitude of periastron becomes indeterminate as the

eccentricity approaches zero and so should not be regarded as reliable.

The most important deviations from the earlier parameters derived in the ultraviolet (from the Si III lines) are the changes in the epoch of primary minimum and in the eccentricity. The epoch now deviates by 0.05 and 0.11 in phase from Koubský's 1978 and 1980 ephemerides respectively, as compared to the previous results of 0.28 and 0.22 for the fit to the Si III data. For the eccentricity, the cross-correlation gives a value which is zero to within the errors, and is in excellent agreement with the optical data of Koubský [1].

The σ Sgr template was shifted by a velocity appropriate to that of the derived binary model at the phase of observation before dividing it into each CX Dra spectrum to yield a 'CSM only' profile. Montages of these reduced spectra are given for each of the superionic lines N V, Si IV, C IV and Al III in appendix A where the quality of the *photospheric* match can be readily judged from the constancy of the spectral regions away from the resonance lines, at phases where the CSM is expected to be localized in velocity space (e.g. $0.0 \lesssim \phi \lesssim 0.2$; see section 2.5). In general this division is more than satisfactory; any deviations from uniformity due to template mismatch are small, with the other variations being ascribable to the presence of the CSM.

2.5 Interpretation

The profiles divide naturally into several distinct types (see figure 2.6). There are symmetric lines pointing to a natural symmetry to the flow pattern (e.g. Al III,

---

[1] Although the agreement of both *IUE*-based datasets with the optical data of Koubský is quite good, for the purposes of assigning a phase to each *IUE* observation, the ephemeris of the latter work will be used because of the far greater S/N available with optical data and the greater phase-coverage used for the analysis making such measurements inherently more reliable. Koubský's 1980 ephemeris is:

$$\text{HJD (primary minimum)} = \text{HJD } 2442551.2932 + 6.^{\text{d}}69606\,\phi_{\text{K80}}.$$

$\phi = 0.4799$), and some profiles are 'sawtooth' in appearance (e.g. N V, $\phi = 0.9466$) indicating a decrease in the column density of absorbers (due to a density and/or ionization change) with increasing magnitude of velocity. Some profiles display multiple components (e.g. Si IV, $\phi = 0.3578$) implying a fragmentary flow, probably due to shock disruption of an otherwise well-ordered streaming, and many exhibit an 'emission' component (e.g. Al III, $\phi = 0.8613$) which, it must be stressed, probably appears because of a *lack* of absorption in the data over the template and so is *not necessarily* due to a real emission process.

Whilst no two observations have been taken at precisely the same phase, the above-listed forms of profile are consistently seen to repeat at or near the phases given; thus the velocity structure depends almost entirely on the phase of an observation, and only weakly on its epoch.

Is there a simple, consistent model which explains this cycle-independent phase distribution of velocities?

Consider the 0.25 phase-lag of the redshifted lines behind the orbital motion of the primary. This implies that the CSM apparently moves (approximately) along the line-of-centres of the stars, towards the primary where it probably accretes. This requires that it originates either from, or in the vicinity of, the evolved secondary. The blueshifted components meanwhile, lead the binary motion and are multiple, which may be due to turbulent material leaving the system in a direction 0.25 ahead of the infalling flow in phase, i.e. at right-angles to the latter and in the direction of motion of the primary in its orbit.

The most natural way of linking these two streamers is to allow the flow to loop behind the primary as it falls in from the L1 point, before being ejected. Most of the matter is then moving tangentially to the line-of-sight between phases 0.50 and 0.75, accounting for the observed symmetry of the profiles formed in this region. The appearance of high-ionization potential species like C IV and N V, and the increase in the strength of the lower species (Si IV, Al III) at phases 0.55–0.85 agrees with the occurrence of the stream impact region on the stellar photosphere at these phases.

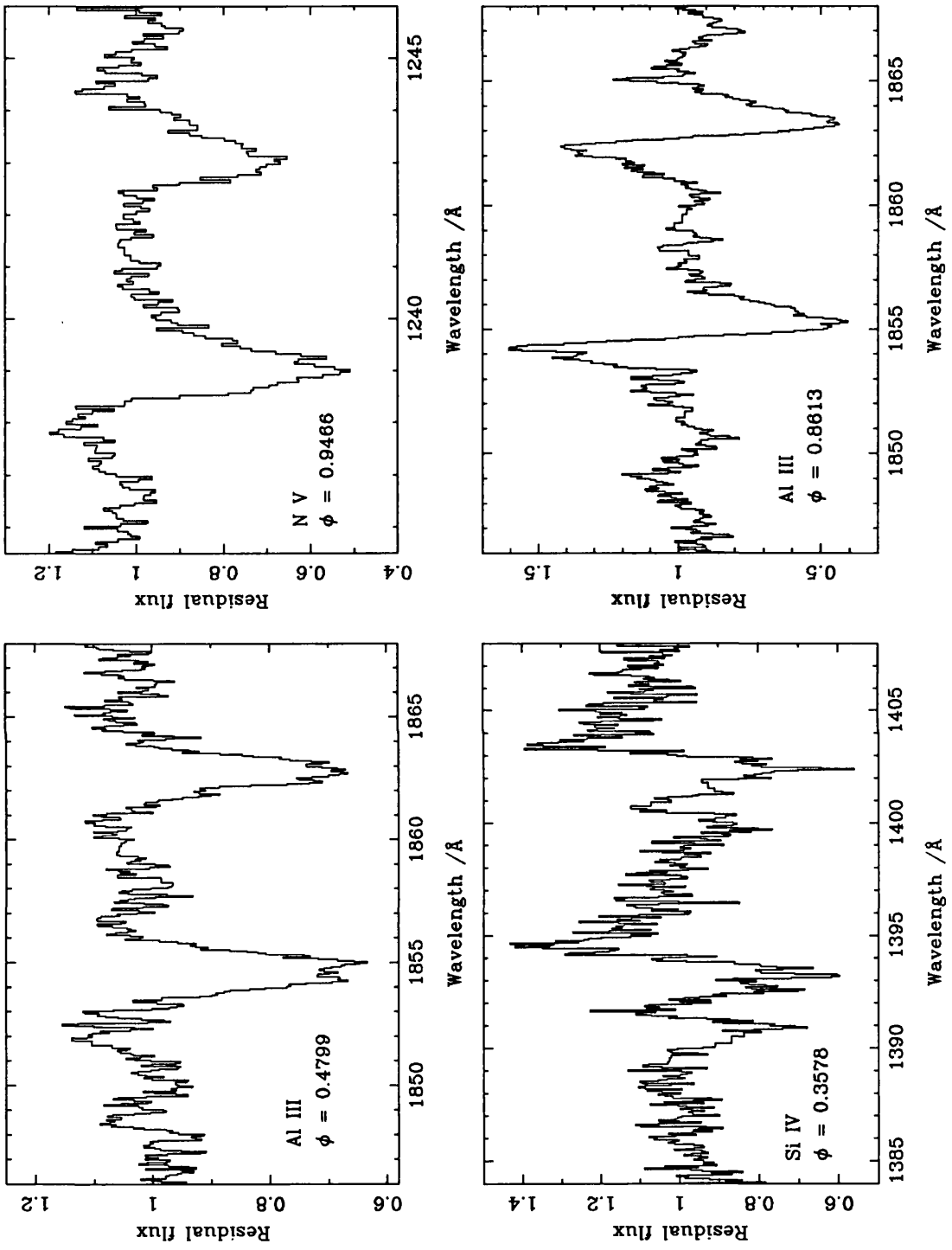

Figure 2.6: *Examples of the various types of profile seen in CX Dra.*

The accretion process also offers an explanation for the fact that the primary of CX Dra is rotating faster than is normal for stars of its spectral type, in that the accreting stream applies a torque to the star, which then spins it up.

There is also a surprising feature of the montages of CX Dra which appears in all four superions, most noticeably in N V. Between phases 0.6580 and 0.6899, in a time $\Delta t \lesssim 5^{\rm h}$, the streaming material almost entirely disappears. Then, between $\phi = 0.7453$ and $\phi = 0.8613$ ($\Delta t \lesssim 19^{\rm h}$), it reappears. The two spectra in this interval (SWP10242 and SWP14703) were taken many cycles apart, demonstrating that this phenomenon is repeatable. This effect is seen consistently across a wide range of ionization temperatures and is therefore unlikely to be due (solely) to a change in the local ionization balance. The most probable cause is a geometric and/or dynamical one. As the matter falls in from the L1 point, it accelerates and reaches the photosphere where a fraction of it is accreted. In accordance with Bernoulli's Theorem, these processes lead to a pressure drop within the plasma as it circles the primary. This means that the stream will collapse towards the orbital plane, causing it to drop out of the line-of-sight to the primary. The reverse situation occurs when the stream emerges from the far side of the primary where the flow is decelerated as it climbs out of the gravity well of the system. The internal pressure in the stream rises causing it to expand back into view. This phenomenon will be referred to as 'stream dipping'.

The origin of this material is most likely to be simple Roche lobe overflow (RLOF) at the L1 point due to the secondary having evolved into its giant phase and filled its Roche lobe. Recent observations of the Hα line by Koubský (1978, 1989) tend to reinforce this model. His latter series of observations show a phase-dependent variation with broad absorption lines appearing at $\phi \sim 0.85$–0.95 where one would expect to be looking straight along the accretion stream and sampling a large range of velocities. Narrow absorption appears at $\phi \sim 0.6$–0.85 where the flow is virtually perpendicular to the line of sight, and emission between $\phi \sim 0.95$–0.6 where the stream is no longer in projection, and only the circumstellar material can be seen.

Peters & Polidan (1984) also adopts this RLOF model. They derive the conditions in the 'hotspot' and posit the existence of a high-temperature accretion region with a temperature $\sim 10^5$ K, an electron number density $n_e \sim 10^9$ cm^{-3}, and a carbon depletion C $\sim$ 0.03 C$_\odot$. The carbon underabundance is taken as an indicator that the matter in the stream originates from the evolved secondary.

To test the feasibility of this model as a description of CX Dra, numerical simulations will be constructed in the next chapter.

Chapter 3

The Single Particle Model

Where there is matter, there is geometry.

Johannes Kepler

3.1 Introduction

To simulate, in detail, a stream of plasma falling between two stars in a binary system would be a task of Herculean proportions, involving a full magnetohydrodynamic treatment, radiation transport in a moving, probably-shocked medium and a very complicated ionization balance.

In order that some headway may be made, the problem of generating a model of circumstellar flow has to be greatly simplified. Early work has concentrated mainly on simple ballistic paths traced out by single 'massless' particles in a binary potential. Warner & Peters (1972) applied a restricted three-body calculation of stream trajectories to cataclysmic variables to demonstrate that the 'hotspots' in the light curves of these systems are due to material accreting onto a ring surrounding the primary from the secondary. Flannery (1974) corrected an error in the previous work and noted that viscosity has an important rôle to play in determining the size of the accretion ring and hence the position of the 'hotspot'. Perhaps the most

refined treatment of gas dynamics in semi-detached binary systems is the work of Lubow & Shu (1975, hereafter LS) in which the problems of three-body flow are examined analytically using perturbation theory.

As a first approximation to such a model, a combination of the work done in the three papers mentioned above will be used to generate single-particle streamlines in binary systems of a given mass ratio. These streamlines are then used to construct simplified velocity-phase curves to compare with the data. The models are also used to find the mapping of the parameter space covering the initial velocity of the stream at the L1 point onto the parameter space covered by the maximum velocity and the impact parameter. This enables the plausibility of an escaping matter stream to be more rigorously discussed.

3.2 The Model

The geometry of the model is shown in figure 3.1. The system consists of a giant-class secondary star (on the left) which is presumed to be filling its Roche lobe and transferring matter to the Main Sequence primary (on the right). The secondary plays little part in the model except in that it contributes a point-like gravitational potential to the system. The mass in the distorted outer layers of the giant is assumed to be negligible and any circulation currents near the Inner Lagrangian point are taken to have no effect on the initially sub-sonic flow of material through that region. The system is rotating in a right-handed sense and all motion is restricted to the orbital plane. For computational purposes, all dimensional quantities are expressed in units of some characteristic scale of the problem. Lengths are in units of the binary separation, a, time intervals are given in units of the reciprocal of the orbital angular velocity, Ω^{-1}, and masses are scaled by the total mass of the system, $M_1 + M_2$. This has the useful property that the results can be applied to *any* given semi-detached binary simply by using dimensional scales appropriate to that system.

Setting the origin of coordinates at the centre of mass of the system (see fig-

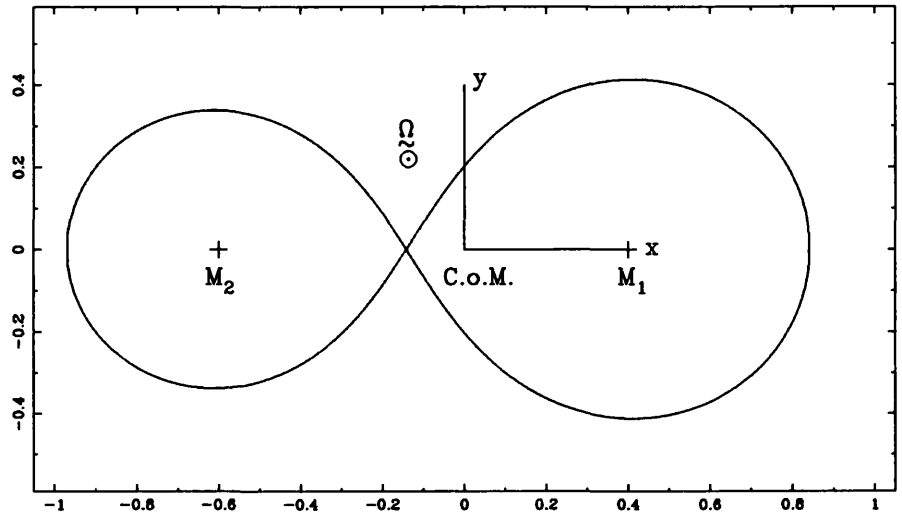

Figure 3.1: *Model geometry for an example system with* $\mu = 0.6$.

ure 3.1), the equations of motion for a 'massless' test particle (*i.e.* $m \ll M$) are

$$\ddot{x} = 2\dot{y} + x + \mu\frac{(x - x_1)}{r_1^3} - (1 - \mu)\frac{(x - x_2)}{r_2^3} \tag{3.1}$$

$$\ddot{y} = -2\dot{x} + y - \mu\frac{y}{r_1^3} - (1 - \mu)\frac{y}{r_2^3} \tag{3.2}$$

where

$$\mu = M_1/(M_1 + M_2), \quad r_1^2 = (x - x_1)^2 + y^2, \quad x_1 > 0$$
$$r_2^2 = (x - x_2)^2 + y^2, \quad x_2 < 0$$

and x_1 and x_2 are the x-coordinates of the centres of mass of the primary (mass-gaining) and secondary (mass-losing) components respectively. The first terms on

the right-hand sides of equations 3.1 and 3.2 are the Coriolis terms; the second terms constitute the centrifugal accelerations and the remaining terms make up the gravitational effects of the primary and secondary, respectively.

The Inner (or First) Lagrangian point is located by solving the quintic equation that describes the *total* force on a test mass for the root that lies on the symmetry axis of the binary system (*i.e.* the root that has a zero-valued imaginary part). The total force is the sum of the centrifugal and gravitational components, thus

$$x_{\mathrm{L1}} + \frac{\mu}{(x_{\mathrm{L1}} - 1 + \mu)^2} - \frac{1-\mu}{(x_{\mathrm{L1}} + \mu)^2} = 0$$

where $(x_{\mathrm{L1}}, 0, 0)$ are the coordinates of the L1 point.

The test particle is placed at the Inner Lagrangian point with a photospheric thermal velocity ε which is small (see LS), and allowed to evolve under the influence of the potential given by equations 3.1 and 3.2.

To solve these equations for the particle motion, they are cast in the form of two pairs of coupled first-order differential equations and solved using a Runge-Kutta-Merson technique (NAG routines D02BHF and D02BBF). The integrated solutions of equations 3.1 and 3.2 then yield both the trajectory of the stream and the velocity variations along the stream. A sample of stream paths is given in figure 3.2, calculated for various values of μ. The centres of the primary and secondary lie at $1-\mu$ and $-\mu$ respectively in this coordinate system. Computation is terminated at the hypothetical disc-edge, defined as the point where the particle's instantaneous specific angular momentum about the primary becomes equal to the specific Keplerian orbital angular momentum at that point, i.e.

$$\Delta j = (j_{prim} - j_{Kep}) = \dot{y}(x - 1 + \mu) - y\dot{x} - \sqrt{r_1} = 0.$$

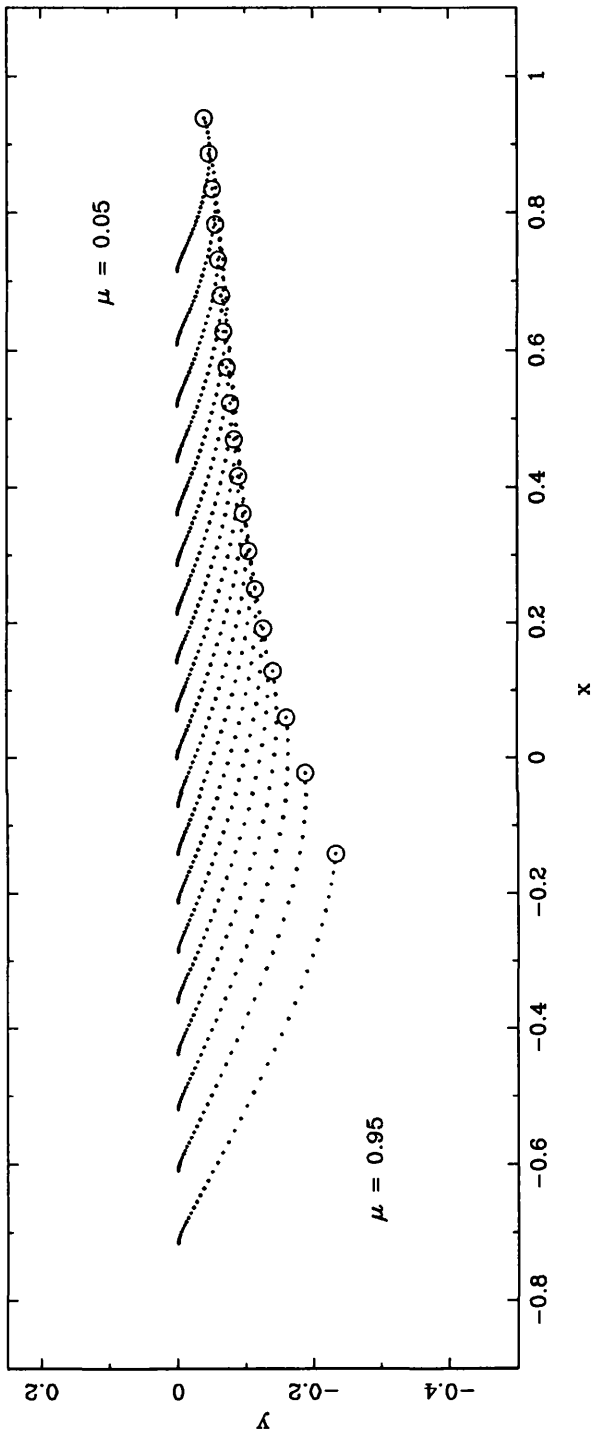

Figure 3.2: *Ballistic stream trajectories.*

3.3 Comparison with the data

To compare this model with the *IUE* FeIII data obtained in the previous chapter, the radial velocity curve for a given model is required. Rather than compute an absorption line profile under this simple model, the velocity at maximum stream density along the *projected* part of the stream is found under the assumptions that the time-independent conservation equation (3.3) holds and variations in velocity and density are confined to the orbital plane, i.e.

$$\nabla.(\rho \mathbf{v}) = 0 \tag{3.3}$$

or, alternatively,

$$\rho v_s = \dot{\mathrm{M}}/A = \text{constant}$$

where $v_s, \rho, \dot{\mathrm{M}}$, and A are the velocity parallel to the stream, the stream density, the mass-flow rate along the stream and the stream cross-sectional area normal to the flow respectively. Hence the maximum density lies at the point of minimum velocity. This was expected to approximate the point of maximum extinction in the observed profiles.

To extract this information, the radial velocity seen at an inclination i to the normal of the orbital plane and centred on the primary is computed as a function of the orbital phase ϕ, remembering that if the binary system rotates in a right-handed sense as seen by the observer, the observer will rotate in the opposite sense as seen from the rest frame of the system. This change of coordinates is easily achieved by applying the general Euler transformation for 3-rotations of a coordinate system at each value of the required phase. For the portion of the orbit where the primary occultes the streaming material, the orbital motion of the primary is substituted on the basis that there will probably be some stellar contribution to the measured line profile.

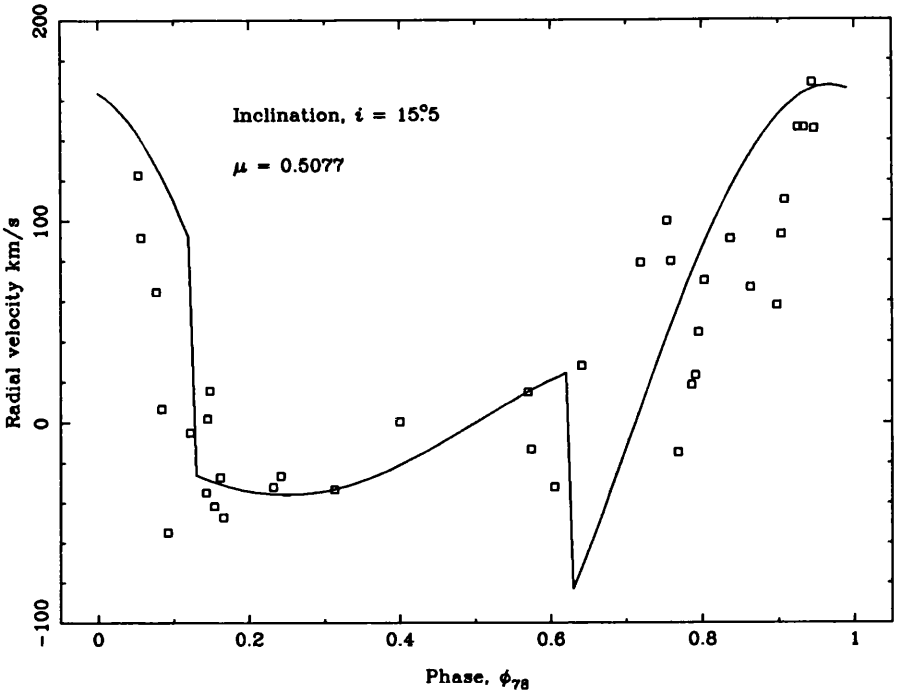

Figure 3.3: *Ballistic model fit to Fe III λ 1895 data of CX Dra.*

Radial velocity curves were constructed for various values of the inclination of the system using the appropriate values of μ and r_1 from Koubský (1978). The best fit as judged by eye is shown in figure 3.3.

3.4 Discussion

As can be seen, the model velocity curve fits all parts of the observed data well. The rapid drop in the line velocity at $\phi \sim 0.1$ is due to the occultation of the stream by the stellar disc and the sawtooth 'jump' at $\phi \sim 0.6$ is caused by the reappearance of the stream. The stream strikes the photosphere of the primary at a phase $\phi \sim 0.7$–0.8 and this is seen in the data as a region of variable or turbulent velocity. The surprising result however, is that the inclination is required to be only 15.°5 to bring the velocity scales into agreement. Is it possible to reconcile this with the superion

velocities noted in the previous chapter? The maximum observed stream velocity is $\sim$ 700 km/s. Allowing for an inclination to the line of sight of 15.°5, the stream has a velocity in excess of 2600 km/s. The primary is neither massive enough to accelerate an infalling stream to this speed nor hot enough to drive a wind of this magnitude. Furthermore, the low inclination implies that the mass ratio of the system is approximately unity. If this is so, then it becomes rather unlikely that the secondary could have evolved as far as the giant branch without the primary also leaving the Main Sequence.

It is clear then that the inclination must be larger than the value derived above and that this discrepancy must explained. Firstly, it can be seen that a major portion of the fit occurs over the part of the velocity curve where the stream is occulted, yielding no information concerning the transfer of matter. Secondly, the data do not accurately constrain the phase at which the rapid drop seen in the velocity curve near $\phi \sim 0.1$ begins. The only 'peak' in the data consists of a small cluster of points at $\phi \sim 0.95$. Given that these lie on the tail of the turbulent region, to base a value for the inclination on these points alone seems unjustified.

What is needed is some criterion by which the validity (or otherwise) of these ballistic models under these circumstances can be judged.

3.5 The conditions for an escaping stream

Material is observed emerging *from* CX Dra at high speed, narrowly confined to phases near $\phi \sim 0.3$. This cannot be attributed to material spilling over the Lagrangian (L2) point behind the primary as the absorption would be observed at $\phi = 0.5$ and later phases, and this is not the case. To obtain a collimated jet of material as observed, the stream from the L1 point must at least partly circle the primary, and escape near phase $\phi \sim 0.3$. By generating a series of ballistic models, the applicability of such simple models to these observations can be tested.

For a given initial velocity (i.e. speed *and* direction), two parameters of the subsequent flow are derived, namely, the closest approach of the stream to the

point-mass primary, b, and the maximum velocity attained by the stream, v_{max}. Figures 3.4 and 3.5 show the results of such calculations for binaries of reduced primary masses $\mu = 0.5$ and $\mu = 0.9$ respectively.

For example, from figure 3.4, a stream launched at an angle of 30° (measured clockwise from the line joining the stellar centres) and at a speed of $3\,a\Omega$ in a $\mu = 0.5$ system, attains a maximum velocity of $\sim 3.2\,a\Omega$ and passes closest to the primary at a distance of $\sim 0.28\,a$.

By imposing conditions on v_{max} and b, limits may be placed upon the flow conditions at the L1 point. In order that a stream of plasma *escapes* from the system it is required that:

1. the stream must miss the primary, i.e. b must be greater than the primary radius, and

2. at some point along the trajectory, the speed of the flow must be greater than the escape velocity from that point.

Typical minimum values for v_{max} and b, which meet these conditions, are 2.08 and 0.134 respectively for $\mu = 0.5$, and 2.35 and 0.151 for $\mu = 0.9$. These are also plotted on figures 3.4 and 3.5. Escaping streams will only form *in the context of this ballistic model* in the upper right-hand quadrant of the parameter space. This appears to limit the initial conditions to mostly supersonic launch speeds at angles which are not along the line-of-centres of the system.

The latter condition is easily fulfilled as the stream is always deflected from the line-of-centres by the Coriolis force through an angle between 19.°5 and 28.°4 as it leaves the L1 point (see LS). The former condition, however, is not so easy to satisfy.

At first sight, it seems that a supersonic ejection mechanism is required to produce the observed stream. Kondo, M^{c}Cluskey & Stencel (1979) propose that surface waves in the form of rotationally-split g-modes can drive matter from the surface of the secondary star in U Cep in this manner. Another possibility is that the secondary possesses a stellar wind which the gravitational potential can partially

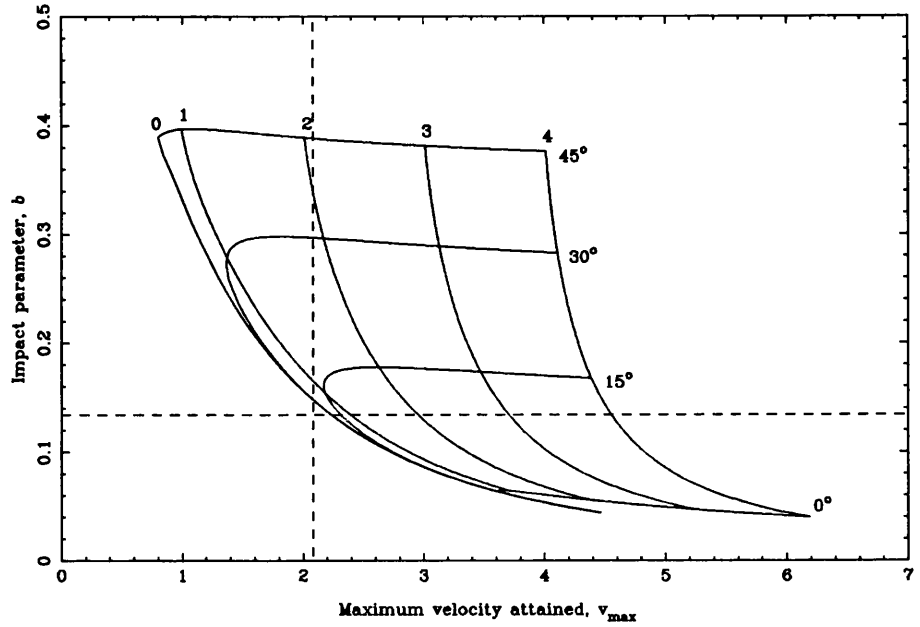

Figure 3.4: *Test for escaping streams in a system with* $\mu = 0.5$. *Contours are labelled with the launch angle and the dimensionless launch speed.*

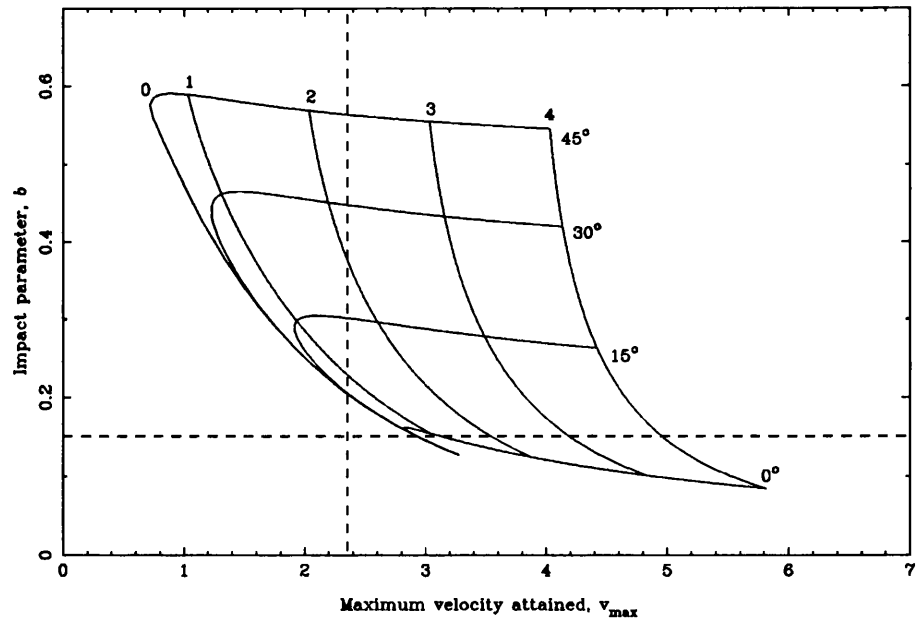

Figure 3.5: *Test for escaping streams in a system with* $\mu = 0.9$. *Contours are labelled with the launch angle and the dimensionless launch speed.*

'funnel' through the L1 point (Sørensen, Matsuda & Sakurai 1974). Both of these processes are nearly spatially axisymmetric (about the secondary) and if either was sufficiently strong to produce the observed lines, it would also be likely to produce substantial asymmetric absorption at all phases, an effect which is not seen. To obtain speeds of the order of $a\Omega$ by thermal means would require gas temperatures higher than 2×10^6 K at the inner face of the secondary. The only possible source of such heating (aside from chromospheric activity in the secondary which can be ruled out on the basis that it would be likely to be observed to occur over the whole star) would be X-ray heating of the secondary by the radiation from the impact zone. CX Dra is a known X-ray source (Guinan, Koch & Plavec 1984), but as the stream itself lies between the impact zone and the L1 point it is probable that most of the X-rays from the 'hotspot' (if that is where they are produced) will be absorbed before they reach the photosphere of the secondary.

It appears, therefore, that there is no way that high-velocity material can be produced *at* the L1 point in CX Dra. The problem, however, is not to give the stream sufficient energy; it must acquire enough angular momentum to avoid collision with the primary (hence the non-zero launch angles) and there seems to be no process by which an inviscid stream can achieve this as its trajectory is completely determined by its launch parameters. A viscous stream, on the other hand, is a different matter. Depending on the strength of the viscous interactions between particles in the stream, angular momentum can be efficiently transported to any part of the stream. Some of the stream will escape accretion at the expense of the part that will strike the primary. In the next chapter, the subject of viscous streams will be investigated in more detail.

Chapter 4

The viscous model

Big whirls have little whirls
That feed on their velocity,
And little whirls have lesser whirls
And so on to viscosity.

Lewis F. Richardson

4.1 Introduction

4.1.1 Possible stream-supporting mechanisms

The ballistic, inviscid model of RLOF constructed in the previous chapter fits the observed FeIII data well, but by no means unambiguously. When the same model is applied to the superions' velocity-phase curve, it is found to be quite inadequate near $\phi \sim 0.2$. A mechanism which supports at least some of the infalling material over the primary's horizon is required in order to produce the streamer of escaping matter traced out by the superions. There are several possible candidates for stream-supporting processes:

1. A radiation-driven stellar wind from the primary,

2. A magnetic field surrounding the primary, and

3. Viscosity in the streaming material.

Consider each in turn.

1. To deflect the stream, a stellar wind would be required to dump an amount of momentum in the stream of the same order as that which the stream itself carries (in a radial direction), i.e.

$$\rho_{\mathrm{wind}} u_{\mathrm{wind}} = O(\rho_{\mathrm{stream}} u_{\mathrm{stream}})$$

   If $u_{\mathrm{stream}} \sim$ few 10^2 km/s $\sim u_{\mathrm{wind}}$ (typical of normal early B-star winds; see Prinja 1989 and Grady, Bjorkman & Snow 1987), then $\rho_{\mathrm{wind}} = O(\rho_{\mathrm{stream}})$ $\sim m_{\mathrm{H}} \times 10^9 \mathrm{cm}^{-3}$. This constitutes a minimum mass loss rate at the stellar surface of $\dot{M} \sim 10^{-9}$ $M_\odot$/yr which would certainly be observable with *IUE* under 'normal' ionization conditions (Prinja 1989), whereas CX Dra shows no signs of such a wind at $\phi \sim 0.1$, where the stream is minimally present; in fact, the velocity profiles indicate an infalling of matter.

2. To decide whether a (putative) magnetic field around the primary would be able to support the stream, a measure of the compressibility of the magnetic field is needed. Shih-I Pai (1962) gives the parameter $\mathcal{R}_{\mathrm{H}}$ as just such a measure.

$$\mathcal{R}_{\mathrm{H}} = \frac{\text{Magnetic pressure}}{\text{Dynamic pressure}} = \frac{\mathrm{B}^2/\mu_o}{\rho u^2}$$

   where B is the local magnetic field strength, ρ is the local plasma density and u its speed. ($\mathcal{R}_{\mathrm{H}} \ll 1$ implies that the field lines are pushed aside by the oncoming plasma; $\mathcal{R}_{\mathrm{H}} \gg 1$ indicates that the plasma cannot penetrate the magnetic region).

The Solar value of B is 1 G but, as CX Dra is a rapidly-rotating star ($v \sin i \sim$ 180 km/s; Slettebak 1982) higher values up to, say, 100 G might be generated by the dynamo effect. Although no convincing fields have been found in rapidly-rotating, *isolated* OB stars (Borra, Landstreet & Mestel 1982), radio observations at 8.4 GHz of several eclipsing binaries with Main-Sequence components by Stewart *et al.* (1988) have tentatively identified fields of the order of a kiloGauss or more. Taking these limits (1 and 1000 G), $\rho = m_{\rm H} n_{\rm H} \sim m_{\rm H} \times (10^9 {\rm cm}^{-3})$ and u $\sim$ 500 km/s, then

$$0.02 \lesssim \mathcal{R}_{\rm H} \lesssim 20000$$

This value of $\mathcal{R}_{\rm H}$ brackets the critical value; either case (support or no support) could be true. No closer limits on B can be set as no search of CX Dra for magnetic effects has yet been carried out. All that can be said is that, unless the magnetic field in CX Dra is high compared to isolated OB stars, the stream is unlikely to receive support from magnetic effects.

3. Viscosity is the most natural solution to the problem because it is inherent in the streaming material and for rigour, should be included in any model as a matter of course. Lynden-Bell & Pringle (1974) have shown that for accreting material to spiral inwards through an accretion disc, it must transfer its angular momentum *outwards* across the disc. (Their arguments for axisymmetric accretion discs are easily generalized to the stream considered here). Thus, as the majority of the matter in the stream falls inwards onto the stellar photosphere, a tenuous outer edge receives the lost angular momentum, preventing it from moving in close enough to accrete, as required. This process is therefore identified as the most likely to be operating in CX Dra and will be pursued further in this chapter.

4.1.2 Viscosity

Few treatments of viscosity deal with the problem analytically. One important exception is the work of Shakura & Sunyaev (1973) and their α-disc prescription in which the kinematic viscosity is given by $\nu_s = \alpha c_s H$ (where c_s is the local sound speed and H the local scale height). Although this enables a formal solution to be derived, the method suffers from the 'empirical' nature of the above relationship and an imposed axisymmetry condition.

Most other attempts to incorporate viscosity into hydrodynamic models rely on some numerical technique in which neighbouring particles can influence each other to a greater or lesser extent as they move through a computationally imposed grid.

Lin & Pringle (1976) adopted a particle-in-cell method in which, after each timestep, each particle's previous velocity is replaced with a fraction, f, of the linear and angular momentum averages about the cell centre-of-mass and a fraction $(1 - f)$ of the original velocity. This has the same disadvantage as the α-disc in that the viscosity parameter (in this case, f) is arbitrary. Henser (1982) improved on Lin & Pringle's method by including pressure gradients and horizontal energy transport, but the arbitrary f is still retained.

Różyczka & Schwarzenberg-Czerny (1986) and Różyczka (1988) make use of a von Neumann-type artificial viscosity which is proportional to the divergence of the velocity field but requires various second derivatives to be computed with the consequent increase in computer overheads.

Prendergast & Taam (1974, hereafter PT) use a method which simulates collisional thermalization of the particles *within* a grid-cell (see section 4.2.1).

Of all the aforementioned viscosity schemes, that of PT is the only one that does not require some *ad hoc* parameter, in that it specifies the mean-free-path of the gas (a *physical* parameter) as the grid size, and between timesteps complete collisional thermalization takes place, driving the velocities back to a Maxwellian distribution—by no means an unrealistic assumption. Therefore, having decided to include viscous effects in the modelling of interacting/Be-binary systems, the subsequent analysis

will employ the Prendergast & Taam viscosity prescription.

4.2 The viscous model

4.2.1 Prendergast & Taam viscosity

The details of the PT viscous model are outlined below.

Particles are allowed to flow through a binary system as in the ballistic models, but at the end of each timestep they are halted and forced to 'interact'. This interaction consists of assigning each particle to a grid-cell and averaging to find the total momentum and thermal energy in a given cell. These parameters are used to construct a new Maxwellian distribution for the velocities from which the next generation of particles are randomly generated. The process thus 'thermalizes' the flow after it has traversed one mean-free-path length and in this way, a 'viscosity' is introduced. In fact, the mean-free-path will be a function of the velocity of any individual particle (and of the timestep) since the distance that a particle travels between 'thermalizing' events is $v\,\Delta t$. In general, the mean-free-path of a particle will be given by

$$l = \min\left(l_{\rm lim}, v\,\Delta t\right)$$

with $l_{\rm lim}$ always providing an upper limit. PT define $l_{\rm lim}$ as the grid cell size $l_{\rm cell}$, and the next timestep to be $l_{\rm cell}/v_{\rm max}$ where $v_{\rm max}$ is the maximum particle velocity found in the grid once a given timestep has been completed.

This formulation has the advantage that velocity and density gradients and even shocks are easily handled and require no special numerical treatment.

4.2.2 Implementation

The computational grid is an $n\times n$ array of cells through which the particles are allowed to evolve under the influence of the equations of motion (equations 4.1 and

4.2). The grid is centred on the centre-of-mass of the primary star and the L1 point is halfway up the left-hand side of the grid. A fixed number of particles (100) is loaded into the L1 point cell at the beginning of each timestep to simulate the mass lost from the secondary's Roche lobe. The mass transfer is supposed to be by thermal evaporation and so each particle is given a small Maxwellian velocity, ϵ_0, upon initialization. The equations of motion, cast in dimensionless form as before, are

$$\begin{aligned} \ddot{x} &= 2\dot{y} + x + \mu\frac{(x-x_1)}{r_1^3} - (1-\mu)\frac{(x-x_2)}{r_2^3} \\ &\quad -\frac{3}{2}\left(\mu\frac{(x-x_1)}{r_1^5} - (1-\mu)\frac{(x-x_2)}{r_2^5}\right)\frac{\epsilon^2}{\mathrm{B}} \end{aligned} \tag{4.1}$$

$$\ddot{y} = -2\dot{x} + y - \mu\frac{y}{r_1^3} - (1-\mu)\frac{y}{r_2^3} + \frac{3}{2}\left(\mu\frac{y}{r_1^5} + (1-\mu)\frac{y}{r_2^5}\right)\frac{\epsilon^2}{\mathrm{B}} \tag{4.2}$$

where B is defined below.

These equations differ from equations 3.1 and 3.2 by the appearance of terms proportional to ϵ^2/B. These are the vertically-averaged pressure terms arising from the motion of particles perpendicular to the computational (i.e. orbital) plane and are derived from a Taylor expansion of the potential about the orbital plane ($z = 0$) thus:

$$\begin{aligned} \Phi(x,y,z) &\sim \Phi(x,y,0) - \frac{1}{2}z^2\left(-\frac{\partial^2\Phi}{\partial z^2}\bigg|_{z=0}\right) \\ &= \mathrm{A}(x,y) - \frac{1}{2}z^2\,\mathrm{B}(x,y). \end{aligned}$$

Differentiating this expression and averaging over the vertical direction yields the

average in-plane acceleration equation

$$\langle \mathbf{F} \rangle = \langle \nabla \Phi \rangle = \nabla \mathrm{A} - \frac{1}{2} \langle z^2 \rangle \nabla \mathrm{B}$$

which, when expanded, gives equations 4.1 and 4.2.

Assuming hydrostatic support in the direction perpendicular to the orbital plane and the Perfect Gas law gives a vertical density distribution of the form

$$\rho(x, y, z) = \rho(x, y, 0)\, e^{-\frac{1}{2}(z^2/\langle z^2 \rangle)} \tag{4.3}$$

where $\langle z^2 \rangle = (kT/\mu m_{\mathrm{H}} \mathrm{B}) = \varepsilon^2/\mathrm{B}$. Here ε is seen to be the *local* thermal velocity of the plasma and is computed with the proviso that if the calculated gas temperature is lower than that of gas in equilibrium with the primary's radiation field, the gas temperature is set to this equilibrium value.

The presence of these extra terms allows the density scale-height of the stream to be found as well as the usual in-plane variables; the scale-height is needed to test for the occurrence of 'stream dipping' as observed in the *IUE* data (see chapter 2).

To evolve the particles over each timestep, the assumption is made that, because the particles are only allowed to move a distance of the order of one grid-cell or less (i.e. the timesteps are small), the forces acting on the particles are constant for the duration of the timestep. Any particles (bound or unbound) leaving the grid are lost to the computation.

In the original PT formulation, they approximate the Gaussian form of the Maxwellian velocity distribution by a parabolic distribution. The work presented here uses the full Gaussian form, thereby including the high-velocity particles in the Maxwellian tail that are excluded from PT's analysis. Omission of these particles is likely to render the viscosity less efficient as the average momentum transfer per collision will be lower.

Here the gas is treated under the adiabatic approximation. Energy is strictly conserved between timesteps (in the cell averaging) and as the particles are moved, the timestep is made short enough to ensure that the assumption of a constant

acceleration *during* the timestep is a good approximation to the 'true' gravitational acceleration. The approximation will be worse for particles in regions where the potential gradient is steepest (regions where the force is large, for example, close to the stellar surface) but any effect is small (see section 4.3). Radiation losses from the stream are ignored.

PT use a variable-timestep formulation which explicitly prevents any particle moving further than one cell-width. This, however, tends to a constant timestep once initial transients have died away, and since the run-time of the models presented here is long compared to the transient timescale, a constant timestep of $\Delta t_{step} = 0.02$ (derived from experimentation with the models) is used. This means that the maximum mean-free-path of particles in these models is derived internally (to the program) from a combination of the chosen timestep and the maximum velocity appearing in the grid. Once the steady-state has been achieved, the mean-free-path (or equivalently the viscosity) is controlled by a combination of the value of Δt_{step} which establishes the mean-free-path length, and the grid size which sets the scale of the viscous interaction. For low-density media such as the streams considered here, the mean-free-path ($\propto \Delta t_{step}$) dominates the computation.

There is also a need to allow for the non-synchronous rotation of the primary; in CX Dra the synchronous rotation rate is $2\pi R_1/P \sim 32$ km/s but the primary rotates at $v \sin i \sim 180$ km/s (Slettebak 1982). PT have shown that this rapid prograde rotation can enhance the mass lost from the system (although there is some question as to whether this is just a result of the way they model the primary's photosphere). A ring of particles at high-density and encircling the primary point-mass was continuously re-initialised to simulate the presence of the stellar photosphere. It was assigned a flow velocity equal to the desired photospheric rotation velocity and a thermal width of zero to inhibit 'evaporation' of the photosphere (see section 4.3).

Models were run for a pre-determined number of orbital periods (usually two) and are then averaged over all previous timesteps. This reduced fluctuations in the structure of the circumstellar material, making it more amenable to later interpola-

tion and manipulation. The free-fall time of the gas from L1 onto the photosphere was typically $O(\frac{1}{6}P)$ and so the initial absence of the gas stream constitutes $< 10\,\%$ of the total time used for the averaging process (for a run over two periods).

4.3 Tests of the Model

The models of U Cep from PT were used to benchmark the models produced here. To aid the comparison, the same parameters (from Kopal & Shapley 1956; Kopal 1978) are used. They are $M_1 = 2.9\,\mathrm{M}_\odot, M_2 = 1.4\,\mathrm{M}_\odot, \mathrm{R}_1 = 2.4\,\mathrm{R}_\odot, \mathrm{A} = 14.1\,\mathrm{R}_\odot \Rightarrow \mu = 0.6743, r_1 = 0.1708$.

Figures 4.1 and 4.2 show the density and velocity distributions respectively in the model of U Cep. In comparison to the relevant figures of PT (figures 11 and 12), it is apparent that the infalling part of the stream is reproduced well, but the escaping streamer, the shock front on the inner edge of the accreting stream and the large quantity of circumstellar material seen in PT are *not* present in these models.

This discrepancy cannot simply be accounted for by differences in their treatment of either the velocity distributions or the cooling of the plasma. Both assumptions, of a *full* Gaussian velocity distribution and of adiabaticity, act to increase the support given to the infalling stream, the former by increasing the (angular) momentum transfer per collision over the PT models and the latter by inhibiting the energy (and hence pressure) losses from the stream.

Tests on the viscosity parameter indicate that, as expected, reducing the size of the grid cells (and hence the mean-free-paths of the particles), reduces the viscosity and causes the stream to contract in both width and in height, and to approach a purely ballistic solution. Mean-free-paths are typically of the order of $4\,l_{\mathrm{cell}}$, implying that the associated viscosities are four times *less* efficient than in PT. To compare the two methods of modelling, $\Delta \mathrm{t}_{\mathrm{step}}$ was set to 0.005, increasing the viscosity by a factor four and making it equal to that of PT. Such models show marginal differences from those at lower values of the viscosity in that a slightly larger fraction of the accreted mass spills over the primary's horizon, but they still show large departures from the

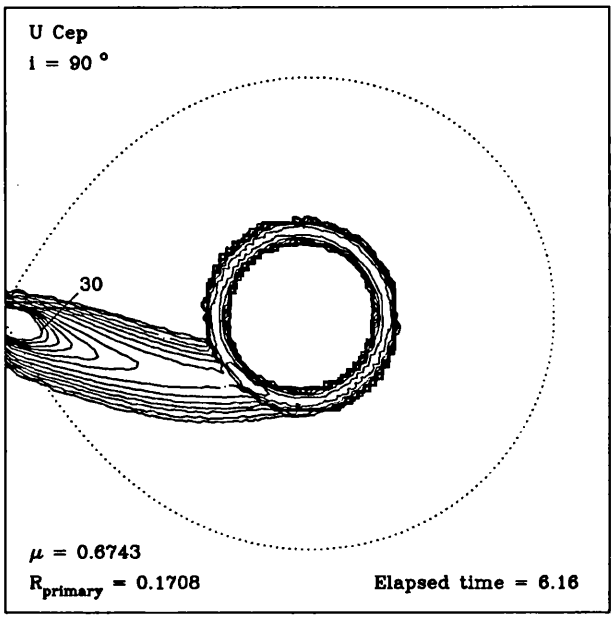

Figure 4.1: *Surface density plot for U Cep. The contours begin at the contour marked* 30 *and decrease as* (30,25,20,16,12,8,4,2,1,0.5,0.25,0.1,0.05). *The densities are in units of particles per grid cell.*

PT simulation, implying that there are substantial differences in the models.

Differences in the 'input physics' are unable to account for this discrepancy, so it is possible that the particular numerical methods used in coding this scheme can explain the divergence of results.

If there are insufficient particles in the model to accurately map out the density distribution, then the very low density regions (such as those absent in the models of this work compared to those of PT) would not appear. However, trials that involve increasing the number of particles crossing L1 per timestep by a factor ten, produce results that do not differ significantly from results produced at lower surface densities and so remain at variance with PT and their models. (All densities are, of course, ten times higher than before but the ratio of the densities in any two regions

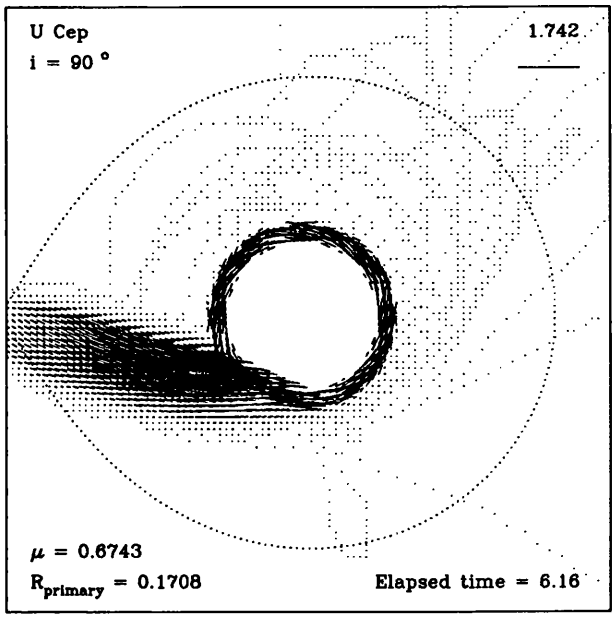

Figure 4.2: *Velocity plot for U Cep. The velocity scale is given in the top right-hand corner in units of* $a\Omega$.

does not vary).

Another possibility is that PT fail to control the particles comprising the photosphere of their first model accurately, and that the subsequent use of this first set of results (case A) as a starting point for their other computations (their cases B i) and ii)) distorts their findings. One might argue that because the photosphere is given zero velocity but a *non-zero* temperature in their case A (synchronous rotation), 'evaporation' can take place, creating an expanding disc of circumstellar material which deflects the infalling stream enough to produce the escaping streamer. Then, when the photosphere is 'spun-up' for use as a rapidly-rotating primary (their case B ii)), its mass-motion dominates the thermal motion, inhibiting 'evaporation' and allowing the previously circumstellar gas to accrete. Such an effect *is* noted by PT but they do not attempt to explain it. The models produced here have been tested

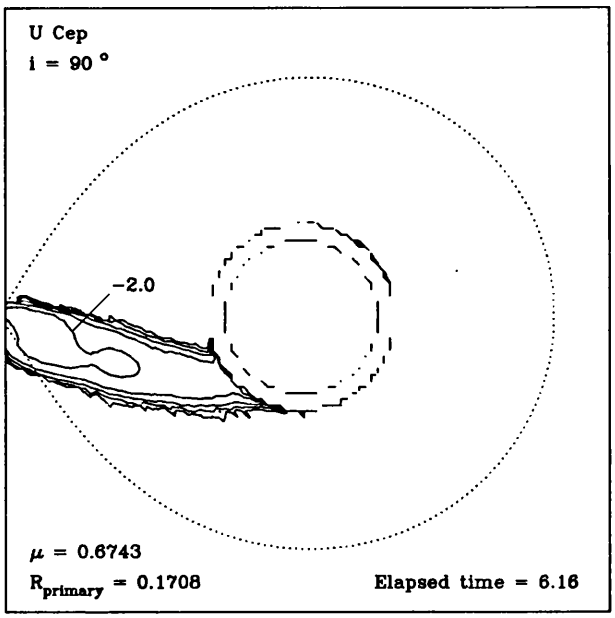

Figure 4.3: $\log_{10}$(scale height) *plot for U Cep. The contours begin at the contour marked* −2.0 *and decrease as* (-2.0,-2.5,-3.0,-3.5,-4.0). *The scale-heights are given in units of the binary separation a.*

for this effect and in all cases no more than five particles 'evaporate' over two orbital periods out of the several thousand that go to make up the photosphere.

Without being able to compare the two codes directly, the above is no more than informed conjecture, but since several potentially more plausible avenues have been explored to no avail, only the possibility described above (or others that are equally speculative) remains.

It is important to determine the value of the viscosity (i.e. Δt_{step}) that should be used. PT have too much material in their final model and their derived velocity curve completely fails to match the observed data because of this. Obviously, the viscosity should be reduced to prevent such large outpourings of matter. Olson (1980) reports large variations in the light from the disc in U Cep over periods as short as ten days,

and describes the transient discs observed. Batten (1976) presents nearly a century of $(O-C)$ data which shows small fluctuations about a simple parabolic curve. That the disc is seen to vary quite strongly with minor changes in the mass transfer rate implies that the stream width cannot be large enough to allow substantial amounts of matter to escape accretion, otherwise a large *stable* structure would form. This, in turn implies that the viscosity used should be small enough to prevent the formation of a permanent disc. Reducing the viscosity by a factor of four is known to make a negligible difference to the models of U Cep shown in figures 4.1–4.3 which appear to be in agreement with the requirements above. With this in mind, the value of Δt_{step} that was previously adopted (i.e. 0.02) was retained.

There is also the question of whether or not the final result is in a state of dynamic equilibrium. Mass is transferred *about* the system on a viscous timescale ($\tau_{visc} \sim l_{visc}/v \sim O\,(0.01)$). This is of the same order as the timesteps used and thus internal adjustments to the distribution of matter in the system are made very quickly. This leaves the possibility that mass is gained on a secular timescale by the system. Any such effect should appear as a slow build-up of particles in the computational grid. Dynamic equilibrium is reached when the total number of particles remains constant. Run-time statistics for the model of U Cep show that the number of particles present in the grid rises steeply from zero to an approximately constant value of 7500 after $t \sim 1.5\,\Omega^{-1}$. This 'constant' value actually has a very small gradient of 4.5 particles gained per unit time indicating that there is an *extremely* slow build-up of material going on in the system. This rate of mass addition requires more than 25 orbital periods to produce a significant ($> 10\%$) effect, assuming that it is maintained; a time span well beyond the limits imposed by computing time restrictions. Statistics for CX Dra show a similar rapid rise to 10^4 particles followed by a slow growth of 2.4 particles per unit time (computed over a period $t \sim 70$). This rate requires 83 orbital periods to affect the system. Therefore, because of computing limitations, it was assumed that this secular growth does not affect the long-term distribution of material in any way.

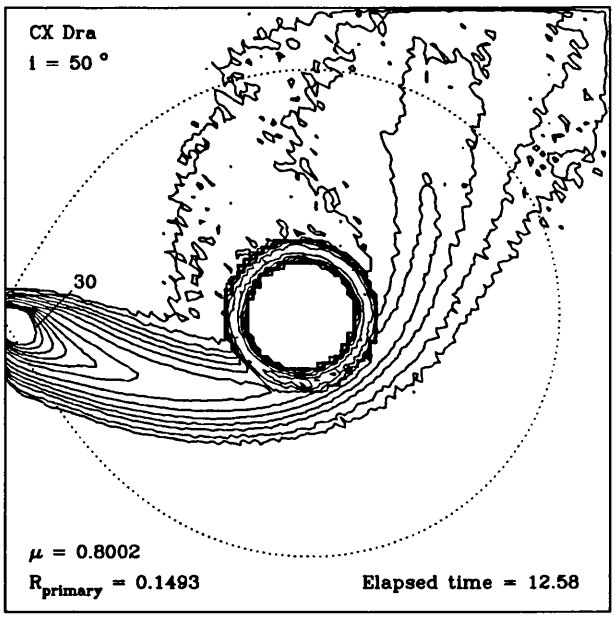

Figure 4.4: *Surface density plot for CX Dra. The contours begin at the contour marked* 30 *and decrease as* (30,25,20,16,12,8,4,2,1,0.5,0.25,0.1,0.05). *The densities are in units of particles per grid cell.*

4.4 Results

Models for CX Dra have been computed using the data from Koubský (1978) , taking $i = 50°$ as an example, and are shown in figures 4.4, 4.5 and 4.6.

Whilst not wishing to repeat the comprehensive discussion of PT, it is nevertheless instructive to point out the salient features of the flow.

Material becomes supersonic at the L1 point and is subsequently deflected by the Coriolis force as it falls towards the primary. Most (> 90%) of the material accretes onto the photosphere, but a small fraction misses the primary altogether, due to the low fractional size of the star. The stream spreads by the action of viscous internal forces and the material on the outer edge thus avoids accretion.

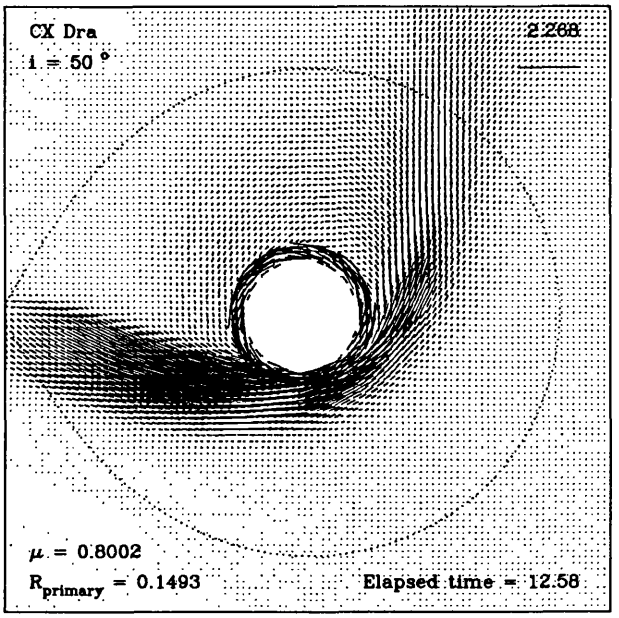

Figure 4.5: *Velocity plot for CX Dra. The velocity scale is given in the top right-hand corner in units of* $a\Omega$.

This matter is about half as dense as that in the core of the stream and is moving at about 40–50 times the local sound speed. By the time it is ejected in approximately the direction of the orbital motion of the primary, it is highly turbulent and probably strongly shocked. This region (along with collisions within the stream) is considered to be responsible for the production of the superionic species seen in the ultraviolet spectral data. The plasma then forms two further components. Some particles will not have sufficient energy to escape the system and will complete their orbits around the primary, either raining back down onto the leading face of the star or continuing on to become entrained into the inner edge of the accreting stream. Contrary to PT, there is no shock front seen in this region, implying that the re-attachment of this gas is an altogether more gentle process; indeed, the velocities at this interface appear quite well matched with very little slip between them. The

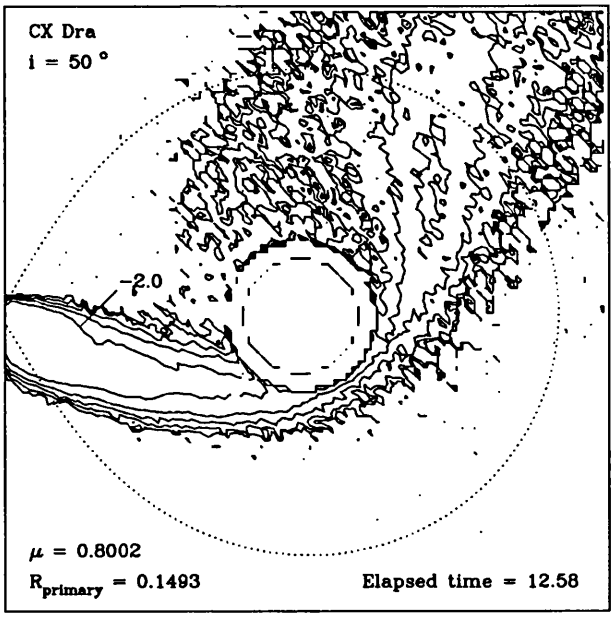

Figure 4.6: $\log_{10}$(scale height) *plot for CX Dra. The contours begin at the contour marked* -2.0 *and decrease as* (-2.0,-2.5,-3.0,-3.5,-4.0). *The scale-heights are given in units of the binary separation a.*

remaining material leaves the computational grid in a highly anisotropic fashion. Figure 4.7 shows the distribution of bound (KE < PE) and unbound (KE > PE) particles as a function of the phase where they cross the grid boundary. The escaping stream is highly collimated in the direction $\phi \sim 0.3$ and it is this that gives rise to the large blueshifted features in the spectral lines. A small amount of material also escapes between $0.6 \lesssim \phi \lesssim 0.8$; this probably originates in the outer edge of the stream where the viscous transfer of momentum causes some high-velocity particles to escape. Of the 5000 particles entering the grid per unit time, 7 % leave the grid but are bound (although these should strictly return at some point, their loss due to grid-clipping is expected to have a minimal effect), and the remaining 0.7 % actually depart the system altogether to contaminate the interstellar medium.

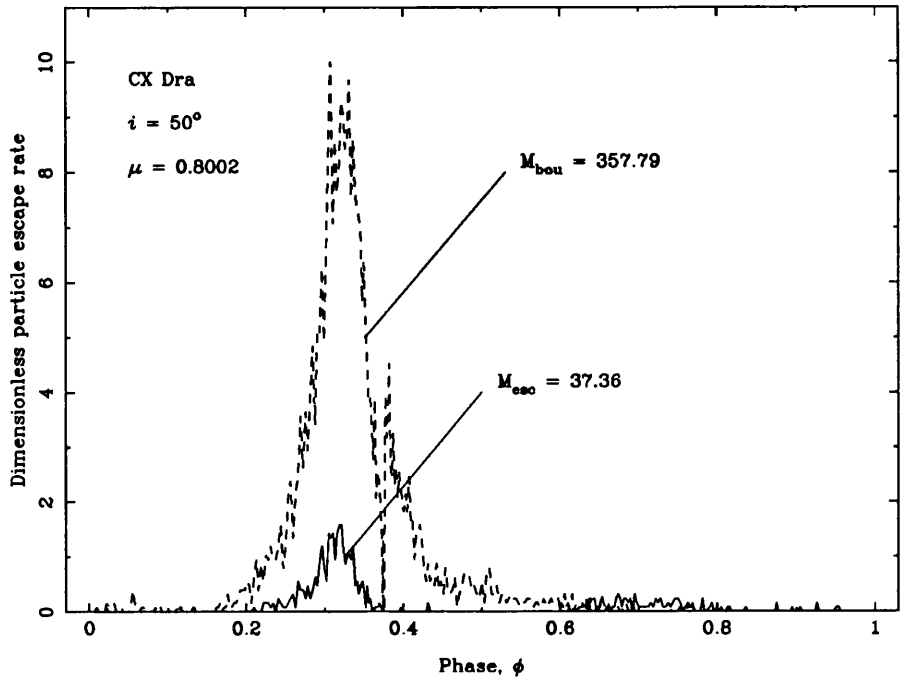

Figure 4.7: *Anisotropy of the particle escape in CX Dra. The grid escape rates are given in particles per unit dimensionless time.* M_{bou} *and* M_{esc} *are the rates for energetically 'bound' and 'free' particles respectively.*

4.5 Scale-height predictions

It is now possible to investigate the observations of 'stream dipping'. Given the stream model, the stream height can be calculated as a function of distance *along the stream* from the L1 point. A search of the data is shown below. The search criterion finds the maximum scale height over the cross-section of the stream. Superimposed on the distribution are the analytic solutions for the scale height of the stream taken from Lubow & Shu (1976). Two models have been computed (see figure 4.8); one on the assumption that hydrostatic equilibrium holds over the whole vertical structure of the stream (h_{ω_z}), and the other making allowance for the inertia of the streaming material as it passes through a rapidly-varying gravitational field ($h_{\sqrt{\chi}}$). The viscous

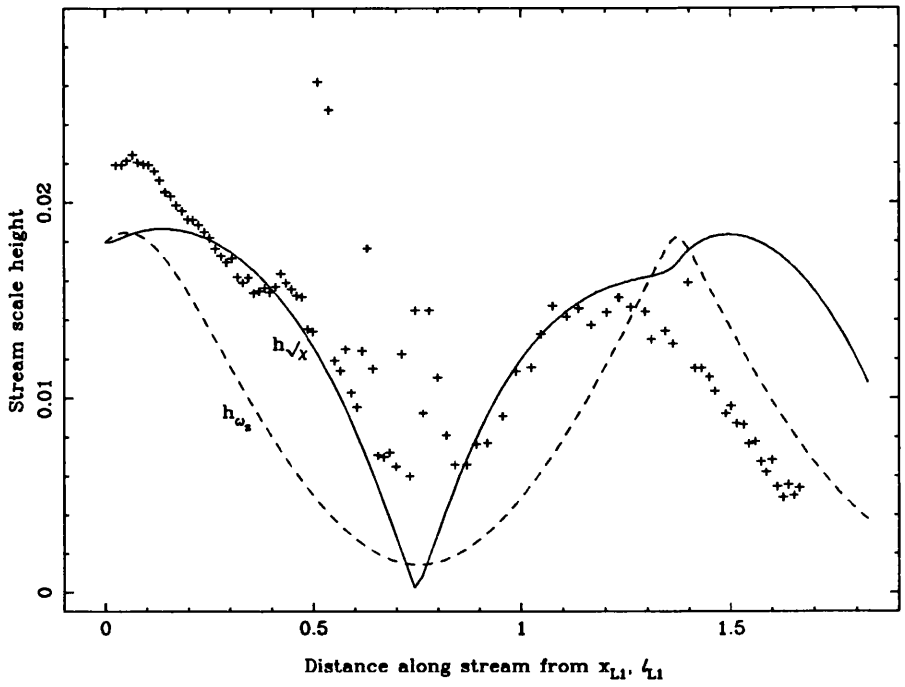

Figure 4.8: *Comparison of the density scale-heights produced by the viscous model* (+), *the hydrostatic assumption* (h_{ω_z}), *and the inertial calculations* ($h_{\sqrt{\chi}}$) *of LS.*

model displays a similar behaviour to the inviscid ones.

The stream collapses vertically as the material accelerates inwards, in accordance with Bernoulli's theorem, the turbulent accretion zone is clearly present near minimum scale-height and the viscous gas undergoes free expansion into the vacuum between $0.8 \lesssim l_{\rm L1} \lesssim 1.4$ before diffusion takes over and the stream disperses. There are, however, two important differences. Firstly, the greater viscous scale-heights are due to the inclusion of radiative heating of the gas by the primary—if this energy source is removed the viscous model agrees almost perfectly with the Lubow & Shu models over the infalling part of the stream, which subsequently evolves in the same manner as shown here. Secondly, the departing stream does not attain the same scale heights as the infalling stream. This is partly due to diffusion, and partly due to the loss of matter in the stream by accretion onto the primary.

The minimum stream height is approximately 3–4 times smaller than the maximum. For a density distribution which is Gaussian perpendicular to the orbital plane, this can reduce the density of material above the orbital plane, seen at differing phases, by an order of magnitude or more, easily accounting for the observed 'stream-dipping'.

The addition of viscosity to models of RLOF, therefore, provides a good qualitative agreement between observations of CX Dra and theoretical predictions in terms of the expected three-dimensional mass distributions, and of the 'stream-dipping'.

Chapter 5

Ultraviolet line synthesis

Grau, teuerer Freund, ist alle Theorie,
und grün des Lebens goldner Baum.

Faust's Mephisto

5.1 Introduction

The analysis of the preceding chapters has led to a good qualitative agreement between the hydrodynamic models constrained by a few reasonable assumptions and the model of CX Dra inferred from observations in the ultraviolet. The high-ionization stages of several common elements are due to the collisional ionization occurring within the stream and the strongly-shocked accretion zone, the 'stream-dipping' is a consequence of Bernoulli's Theorem in the infalling streamer of this semi-detached binary system, and the blue-shifted line components originate in an emergent tongue of material which escapes accretion by the action of viscous forces within the transferred plasma.

It is desirable, nevertheless, to produce a more quantitative description than the above, both in order to derive some physical parameters of the system and to further demonstrate the concordance between observation and theory. Such a description

should not only be capable of reproducing the gross properties of the observations but should also be able to distinguish between models on a more subtle level. For example, it should accurately mirror the range of velocities present in the observations rather than just predicting a 'global' radial velocity. A secondary consideration is that the models should be presented for comparison in a form that does not require the data to be excessively manipulated, for this risks losing potentially important information altogether. The generation of synthetic line profiles satisfies both of the above criteria. In addition, the required density and velocity distributions already exist in the form of the models of chapter 4, leaving only the appropriate equation of radiative transfer to be solved.

There are many possible schemes, of varying degrees of complexity, for generating line profiles, from the simple absorbing slab model to the methods devised to take advantage of large velocity gradients (e.g. Sobolev 1960) or specialized geometries in resonance line synthesis (e.g. Rybicki & Hummer 1978; Olson 1982) . However, unless the situation has an exploitable symmetry, for instance in the case of a spherically symmetric wind, the overheads in terms of computing time rapidly become prohibitive. The most prudent (and illuminating) approach to the problem of simulating the observed superion line profiles, and that adopted for the subsequent analysis, therefore, is to progress through models of increasing complexity until a satisfactory agreement between the observations and the models is achieved.

5.2 Profile synthesis: Absorption

5.2.1 The 'slab' model

The simplest case of radiative transfer is the 'slab' absorption approximation in which the intervening plasma is treated as a plane of absorbing material with no scattering or emission and which removes radiation from the incident radiation ac-

cording to the fashion

$$I(L) = I_0\, e^{-\tau(L)}; \qquad \tau(L) = \int_0^L \chi\, dl$$

where I_0 is the incident intensity, τ is the optical depth along a ray through the slab of geometric thickness L, and χ is some opacity prescription.

The opacity used under the 'slab' scheme is the line opacity of Mihalas (1978a) for a species in LTE:

$$\chi_l^* = \frac{\sqrt{\pi}e^2}{m_e c} f_{ij}\, n_i^*\, \frac{H(a,v)}{\Delta\nu_{\rm D}} \tag{5.1}$$

where	n_i^*	=	the number of absorbing ions (in LTE)
	$H(a,v)$	=	the Voigt profile of the line
	a	=	$\Gamma_{ij}/4\pi\Delta\nu_{\rm D}$
	v	=	$\nu - \nu_0\,(1 - \xi_p/c)$
	$\Delta\nu_{\rm D}$	=	$\nu_0\,\xi_0/c$
		=	the Doppler width of the line
	ξ_p	=	the local mass-velocity of the plasma
	ξ_0	=	the local thermal velocity of the plasma

and all other symbols take their conventional meanings. This ignores both stimulated emission and contributions to the opacity in the continuum.

Although Kamp (1978) has shown that strong silicon lines in the ultraviolet region of the spectra of normal stellar atmospheres are "almost unaffected by non-LTE", the assumption of LTE is not physically justified in the present situation because the plasma will be shock- or collisionally-ionized rather than being in thermal equilibrium with the radiation field of the primary. However, in LTE the relevant equations are considerably simplified and so, with the approximation firmly in mind, equation (5.1) was used for the purposes of computational expediency until the results warranted otherwise.

To calculate the opacity the number density of ions, n_i^* and the local temperature (to enable $\Delta\nu_D$ to be found) were required as functions of the distance along the line-of-sight. (For simplicity, the ions are assumed to be all in the ground state, and ionization balance calculations are deferred until later). The electron density and temperature were obtained by interpolating on the grid of hydrodynamic model values which had been extended from the two-dimensional planar format to functions in three dimensions using the assumptions of

1. a vertical distribution of material that is in hydrostatic equilibrium i.e. one that is Gaussian as in equation (4.3), and

2. independence of the velocity structure on the vertical distance from the orbital plane.

The assumption of hydrostatic equilibrium is not unreasonable provided the stream is vertically thin ($h/r \ll 1$), and in general, $v_z \ll \sqrt{(v_r^2 + v_\theta^2)}$, so the second assumption is probably reliable too (except when the system is viewed from high latitudes). In-plane volume densities were computed by assigning each computational particle a mass (from a knowledge of the timestep, the number of particles released at L1 per timestep and a chosen mass transfer rate) and assuming that the surface density of particles in the plane, $\sigma(x, y)$, corresponded to the vertically-averaged Gaussian density distribution of scale-height H, that is,

$$\rho(x, y, 0) = \frac{\sigma(x, y)}{\sqrt{2\pi}\, H(x, y)}.$$

Both $\sigma(x, y)$ and $H(x, y)$ are variables taken from the model binary systems of the previous chapter. Out-of-plane densities were then given by equation (4.3).

The distribution of matter across the face of the star is highly irregular; it was therefore necessary to perform *explicit* integrals of the emergent intensity over the stellar disc to properly account for this. The optical depths were computed along a selection of lines-of-sight and, given the run of photospheric intensity across the

stellar disc, integrals over the disc yield the residual flux thus:

$$R_\nu = \frac{F_\nu}{F_c} = \frac{\int_{0,0}^{1,2\pi} I_\nu(s,\alpha)\, e^{-\tau_\nu(s,\alpha)}\, s\, ds\, d\alpha}{\int_{0,0}^{1,2\pi} I_\nu(s,\alpha)\, s\, ds\, d\alpha}$$

where (s,α) are polar position variables on the stellar disc. The integrations were performed by evaluating the integrands at a set of mesh points (s_i,α_i). Fitting a surface to these points (with NAG routine E01SAF) then enabled the surface integrals to be computed (using NAG routines E01SBF and D01JAF). Experimentation with the number of mesh points to optimize the computer overheads against accuracy led to the use of ten radial and eight azimuthal points to determine the integrals to an accuracy of $< 0.5\%$.

The doublet nature of the lines was ignored in view of the complicated radiation transfer required to treat the overlap region between the red and blue components; only the blue component was modelled and was treated as a single line.

Two possible stellar intensity functions were made available: a uniformly-lit disc which has $I_\nu(s,\alpha) =$ constant, I_0, and a ultraviolet limb-darkening law of the form

$$I_\nu(s,\alpha) = I_0(\bar{a}\,\mu^2 + \bar{b}\,\mu + \bar{c})$$

where

$$\mu = \sqrt{1 - \frac{s^2}{R_*^2}} \quad \text{and} \quad \bar{a} = -0.18,\ \bar{b} = 1.08,\ \bar{c} = 0.10$$

The mean coefficients $(\bar{a},\bar{b},\bar{c})$, averaged over the wavelengths $\lambda\lambda\,1000, 1500, 2000$, were provided by Smith (1989) who computed quadratic fits to the limb-darkening curves of ATLAS model atmospheres with $T_{\rm eff} = 20\,000\,\mathrm{K}$, $\log g = 4.0$. The second intensity function was expected to provide a better fit to the data because stellar limb-darkening is very severe in the ultraviolet (e.g. Gray 1976a), the cooler outer layers of a photosphere radiating exponentially less energy than the hotter deeper layers.

The instrumental point spread function of the *IUE* telescope was not convolved into the synthetic line profiles as its nominal FWHM is given over the short-wavelength (SWP) range as $0.087\,\text{Å} \lesssim \text{FWHM} \lesssim 0.19\,\text{Å}$ (Cassatella & Martine 1990), and it will consequently have little or no noticeable effect on the profiles which are expected to be of the order of several Ångstroms wide. Oscillator strengths and f-values were taken from Wiese, Smith & Miles (1978).

To test the performance of the modelling process, simulations of isothermal homogeneous slabs moving with a uniform velocity were generated and compared to theoretical profiles constructed with the same parameters. The agreement was found to be excellent, and better than 1 %.

5.2.2 Results

The results of several typical calculations are shown in figure 5.1. The profiles are generated at the same phase as a known observation, with (for the purposes of demonstration) $i = 50°$ and the mass transfer rate from the secondary given a range of values. Notice that the mass transfer rate has the value *appropriate for that ion* and is *not* the total mass transfer rate through the L1 point.

The synthetic profiles exhibit the same 'sawtooth' appearance as the observations, the red wing being more shallow than the blue. Notice however, that the profile does not exceed a depth of 10% before the wings begin to become important, as compared to an observed profile depth of $\sim 50\%$ *without* broad wings. In fact, it has proven impossible to produce an absorption profile at *any* inclination and mass transfer rate, and regardless of the chosen stellar intensity function, whose depth is comparable to that of the observation without the Lorentzian wings dominating the profile. The problem arises from the large spread of velocities present in material at low densities as even small amounts of material can contribute significantly to the generation of wings in an absorption profile.

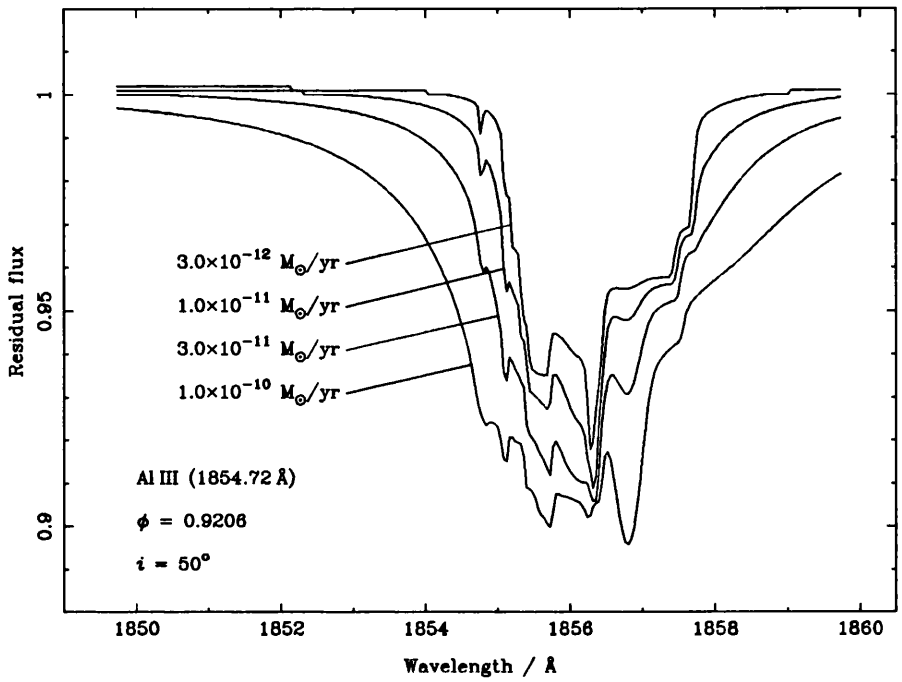

Figure 5.1: *Simulated absorption profiles of CX Dra with* $i = 50°$ *demonstrating the failure of the 'slab' model (see text).*

5.3 Profile synthesis: Scattering

5.3.1 The scattering model

The particular superionic lines observed in CX Dra (and other interacting binaries) are produced by transitions from the ground state of the ion, the so-called 'resonance' lines. These lines have large oscillator strengths (indicative of their high cross-sections for photon absorption) and large transition coefficients A_{ij} (implying a short lifetime for the excited state). The rapid de-excitation of these lines means that their behaviour on the atomic scale is much more akin to the process of photon scattering than to absorption (see Mihalas 1978b). It is hardly surprising therefore, that the 'slab' absorption model of the previous section has proved inadequate.

To derive the analytic form of the intensity in the case where scattering becomes

dominant, the Milne-Eddington equation is used.

$$\mu \frac{\partial I_\nu}{\partial \tau_\nu} = I_\nu - \lambda_\nu B_\nu - (1 - \lambda_\nu) J_\nu \tag{5.2}$$

where B_ν = the Planck function

J_ν = the mean intensity

λ_ν = $[(1-\rho) + \varepsilon\beta_\nu]/(1+\beta_\nu)$

ρ = $\sigma/(\kappa_c + \sigma)$

= the ratio of continuum scattering to total opacity

ε = the photon thermalization fraction

β_ν = $\chi_l/(\kappa_c + \sigma)$

= the ratio of line to continuum opacity

Assuming further a Planck function which is linear in the optical depth scale and that λ_ν, ε and ρ are all constant with optical depth permits a solution for the mean intensity, which can then be substituted into the formal solution to the transfer equation along with the source function taken from equation (5.2) to give the solution for the intensity (Mihalas 1978c). In the limit of pure scattering in both the line and the continuum ($\varepsilon = 0$, $\rho = 1$ respectively) this expression becomes

$$I_\nu(0, \mu) = \frac{I_0}{1 + \beta_\nu}, \tag{5.3}$$

independent of the optical depth scale and where now

$$\beta_\nu = \frac{\sqrt{\pi} e^2}{m_e c} f_{ij} \frac{n_i^*}{n_e \sigma_T} \frac{H(a, v)}{\Delta\nu_D},$$

n_e is the electron number density, σ_T is the Thompson scattering cross-section for electrons and other symbols are as given for the absorption case in equation (5.1).

A value for ε can be estimated from

$$\varepsilon = C_{UL}/(C_{UL} + A_{UL})$$

using the reciprocal lifetime of the state A_{UL}, and the collisional de-excitation rate C_{UL} which can be computed from

$$C_{UL} = 8.6287 \times 10^{-6}\, \Upsilon n_e/(g_U\sqrt{T_e}) \qquad \mathrm{s}^{-1}$$

from Mendoza (1983) for N V and C IV using Υ (the effective collision strength) from Cochrane & M^{c}Whirter (1982), and

$$C_{UL} = 1.676\, f_{ij} \left(\frac{g_L}{g_U}\right) \left(\frac{h\nu}{kT_e}\right) \sqrt{T_e}\, E_U^{-2} e^{+(3h\nu/4kT_e)}\, n_e$$

$$\times \left(1.099\, e^{-(3h\nu/4kT_e)} + \mathrm{E}_1\,(3h\nu/4kT_e)\right) \qquad \mathrm{s}^{-1}$$

from Kastner (1980) with E_U^{-2} in cm^{-1} for Si IV and Al III. Taking $T_e = 20\,000\,\mathrm{K}$ and $n_e = 10^9\,\mathrm{cm}^{-3}$ yields an average value over all four ions of $\overline{\varepsilon} \sim 6 \times 10^{-7}$. This value is quite small compared to typical B-star photospheric values. Interpolating the electron number density from Kurucz model atmospheres (Kurucz 1979) at $T_{\mathrm{eff}} = 19\,000\,\mathrm{K}$ and an optical depth of unity gives $n_e = 3.9 \times 10^{14}\,\mathrm{cm}^{-3}$, leading to a value for ε which is 4×10^5 times greater in the stellar photosphere than in the stream. Increasing the temperature (as in shocked regions) or decreasing the electron density (as in the more rarefied circumstellar regions) serves only to decrease the photon destruction fraction even more. This justifies the adoption of the constant value $\varepsilon = 0$.

The constancy of the continuum scattering parameter ($\rho = 1$) over depth may also be expected to be quite accurate because of the large number of free electrons present in the circumstellar material to scatter the continuum photons. These two assumptions automatically assure that λ_ν is also constant with a value of zero, and hence that equation (5.3) is now independent of assumptions concerning the Planck function.

With the approximation that the ratio of the proton number density to the

electron number density is unity, n_i^*/n_e can be re-expressed thus:

$$\frac{n_i^*}{n_e} \sim \frac{n_i^*}{n_H} = \frac{n_i^*(k)}{\sum_{j=1}^{\infty} n_i^*(j)} \frac{\sum_{j=1}^{\infty} n_i^*(j)}{n_H} = q_{ik} A_i$$

where i is the element, k is the ionization stage, and q_{ik} is the ionization fraction for the element of abundance A_i. The product of the latter two is a parameter to be fitted to the observations.

Given the final form of I_ν, the computations proceed by averaging the profiles over the line-of-sight (hence assuming a profile which is largely independent of the distance along the line-of-sight, in accordance with the depth independence assumed above for other parameters) before integrating them over the stellar disc to obtain the predicted flux distribution.

Again, there is very good agreement between the synthetic profiles and the analytic solutions for isothermal planes of material.

5.3.2 Preliminary analysis

Can the data distinguish between the two stellar intensity functions? Experimentation shows that, in general, there is little to choose between the profiles generated against either background, the differences typically being less than 2% of the continuum and decreasing rapidly with decreasing inclination and increasing abundance. The abundances derived from a uniformly-lit primary illuminating the stream were often marginally ($\lesssim 10\%$) greater than a similar fit with a ultraviolet limb-darkened primary.

Unfortunately then, the choice of stellar illumination function cannot be made on the basis of a fit to the observations as both give similar but equally good (or bad) fits. It is probable that some combination of the two would more accurately represent the true illumination, because the polar regions of the primary are likely to conform well to the ultraviolet limb-darkening law employed, but the equatorial regions will

be subject to an extra source of (mechanical) heating, namely the accretion stream. This will cause a bright strip along a substantial fraction of the stellar equator (Różyczka & Schwarzenberg-Czerny 1986). Given the uncertainty in the dimensions of this 'hot stripe', the ultraviolet limb-darkened illumination was adopted for the analysis.

As might have been expected, the quality of the model fits to the observations is highly variable. Figures 5.2(a), 5.2(b) and 5.2(c) show the three broad categories of fit.

Figure 5.2(a) is a good fit to most of the profile. Apparent 'emission' in the blue wing is almost certainly due to a deficit of absorption in the observations over the standard photospheric template rather than real emission, for although emission might be expected to be common in the circumstellar material, there is little evidence for it in other parts of the profile or in other profiles.

Figure 5.2(b) shows a poor fit in the sense that this type of profile usually demonstrates extra absorption which could credibly be reproduced by a large number of profiles similar to the synthetic profile but variously shifted to cover a larger range of velocities. The explanation for the absence of this extra absorption is simply that the model does not possess any material which has been allowed to build up over a long timescale because of computing limitations. The secular accumulation of material *has* been noted in the models (see section 4.3) but could not be included for the stated reasons. The derived abundance for a profile fit *to the depth of the observed feature* is taken as representative of the (postulated) material with a wider velocity dispersion, i.e. the number of scattering clumps is increased but their chemical abundance remains unchanged.

Figure 5.2(c) shows the third class of profile where virtually nothing about the model profile can be said to agree with the observations. The most probable reason for this is that whereas large temporary excursions from a steady distribution due to shocks and turbulence are occurring, the model has been time-averaged to remove such transient effects and therefore should not be expected to give a good represen-

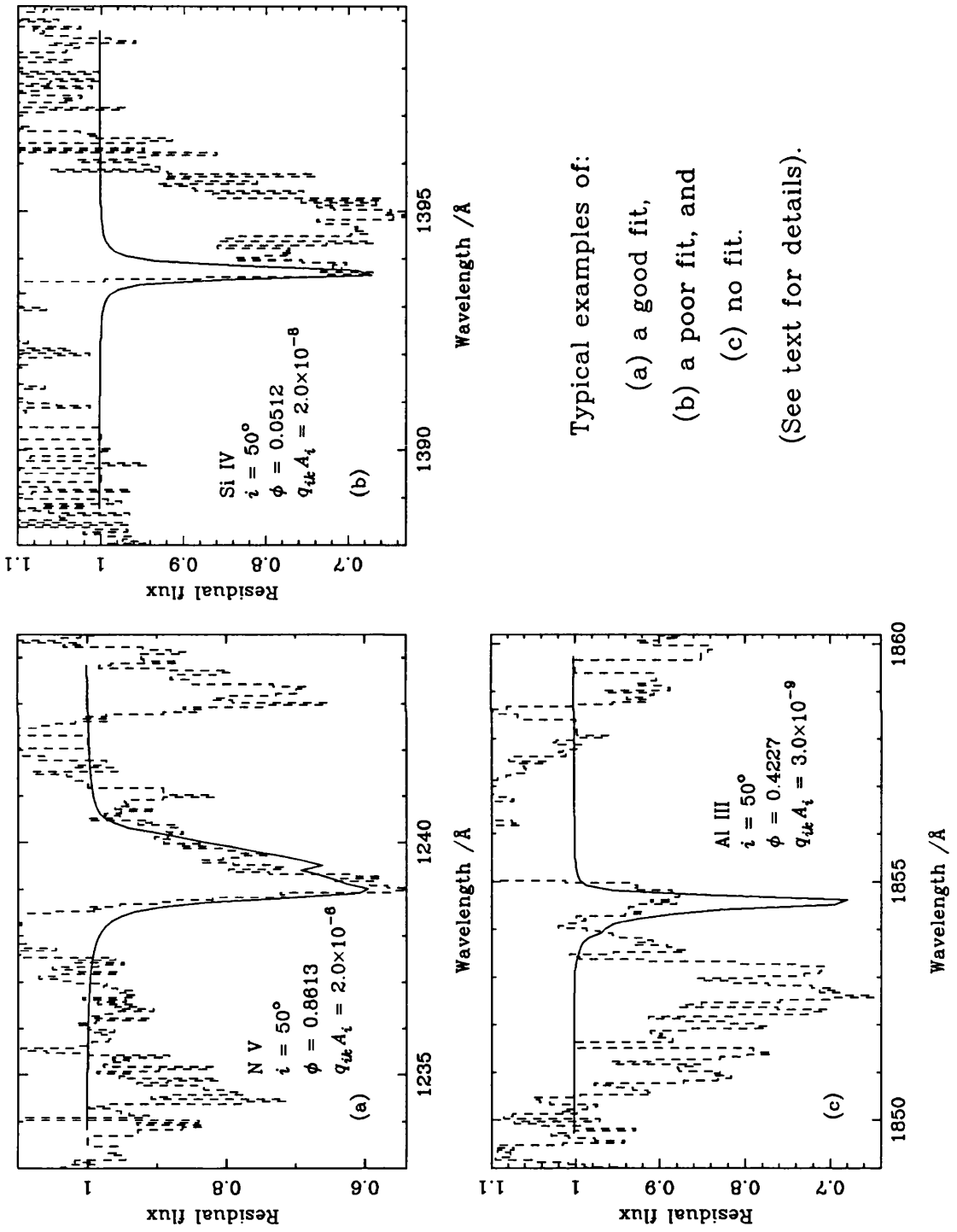

Figure 5.2: *Different qualities of fit between the observations of CX Dra and the synthetic scattering line profiles (see text).*

tation of the fast-moving clumps of matter travelling with random deviations from the general flow.

The essential difference between these last two classes is that the discrepancies in the former are due to the lack of a permanent or quasi-permanent collection of material which might be expected to appear in the model given sufficient computing time, whilst the discrepancies of the latter arise because of purely random fluctuations in the mass distribution which, by their nature, are inherently unpredictable.

It is interesting to note that profiles of N V and C IV fall into two phase-categories; profiles from phases $0.5 \lesssim \phi \lesssim 1.0$ mainly occupy the first ('good') category, whilst the earlier phases reside in the second. For the profiles of Si IV and Al III, only those phases looking directly along the stream ($\phi \sim 0.95$) are good fits, all others lie in the third category. It may be deduced, therefore, that the more-tightly bound lithium-like ions (N^{+4} and C^{+3}) are good tracers of the relatively-dense, collisionally-dominated core of the stream, whilst the sodium-like ions of Si^{+3} and Al^{+2} with their lower ionization energies, can trace out the more rarefied, erratic regions of the circumstellar material as well as just the stream core.

5.3.3 Results

For nine available phases spaced approximately equally about one orbital cycle, the values of $q_{ik}\, A_i$ were obtained from fits by eye to the profiles of lines in the first category and from fits to the deepest parts of the lines in the last two categories (thus providing upper limits). The overall quality of the fits was marginally better for smaller inclinations, but on the whole, the abundance variation was relatively insensitive to the adopted angle. This is because the residual flux is no longer density-dependent (unlike the 'slab' absorption case); it is merely a function of the ratio of two densities which are assumed to have the same spatial dependence. Thus the rapid (exponential) decline in the number density of any ion with vertical distance from the orbital plane no longer has any effect on the amount of scattering. The only remaining effect of a change in inclination is on the size of the radial ve-

locities present in the profile, making the profile wider or narrower in proportion to sin i, greatly reducing its potential as an indicator of orbital inclination. Nevertheless, for sufficiently large velocity dispersions across the profile, profile-fitting might be useful as a diagnostic. To test this, models of the circumstellar material in U Cep using the recent system parameters of Plavec (1983) were generated, providing the velocity distributions required for profile synthesis. The largest velocity dispersions observable within a single profile are those between the phases $\phi \sim 0.9$ and $\phi \sim 0.0$, when the accretion stream is seen end-on. Figure 5.3 shows the C IV profile of U Cep at $\phi = 0.9022$ (SWP4457) which has had a small 'photospheric' contribution removed by division of the rectified profile by the MK standard B5 V star ρ Aur (SWP10389). SWP 4457 was selected to avoid the eclipse phases of U Cep which begin around $\phi = 0.916$. During partial or total eclipse, the continuum becomes depressed and the absorption lines move into emission as the B-star disappears leaving only the hot circumstellar gas radiating strongly in the ultraviolet. This induces a spuriously high abundance in the profile fits.

Profiles generated at 30°, 50°, 70° and the true inclination 85.°5 are shown. It can be seen that an angle *smaller* than the true inclination is indicated by this fitting procedure. This can most reasonably be attributed to the lack of any ionization calculations during the modelling of the stream. The ionization balance certainly changes along the length of the stream (due to shocks, the changing proximity of the primary and the photospheric impact) and it is probable that the superionic species presently under examination only exist in restricted spatial regions of the stream, and hence have a more restricted range of velocities than is possessed by the general mass-flow. For instance, if the fast-moving material present in the red wings of the model profiles in figure 5.3 were to be removed by ionization to a higher stage, the profiles generated at larger inclinations would move into better agreement with the observations. The reverse is not permitted to happen (i.e. more superions cannot be created within the stream) as it is assumed they already occupy all parts of the stream in the present models. There are, therefore, two competing processes at

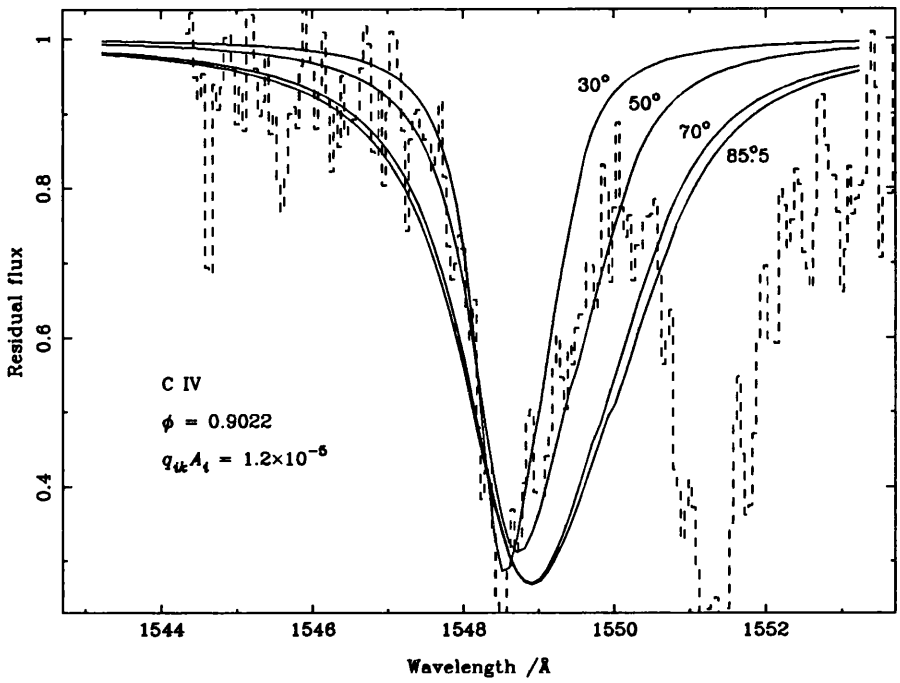

Figure 5.3: *Synthetic C IV profiles at various inclinations for U Cep observed at phase* $\phi = 0.9022$.

work. Some material is *absent* at particular velocities because the model cannot be generated covering timescales which are long enough to allow the secular build-up of circumstellar material, and some material is *present* in the model at velocities where it is not observed because its removal by ionization is not accounted for in the modelling. Fortunately, these two effects usually appear most strongly in different phase-regions of the circumstellar material, and can therefore be separately identified and allowances made. As such, the lack of a proper treatment of the ionization structure of the stream only allows lower limits on the inclination of an interacting binary system to be deduced using this technique.

Figure 5.4 shows the range of the synthetic profile fits to the N V observations of CX Dra at $\phi \sim 0.9466$. The emission in the blue wing aside, the best fitting profiles give a strong lower limit to the inclination of CX Dra, namely $i \gtrsim 35°$. The other

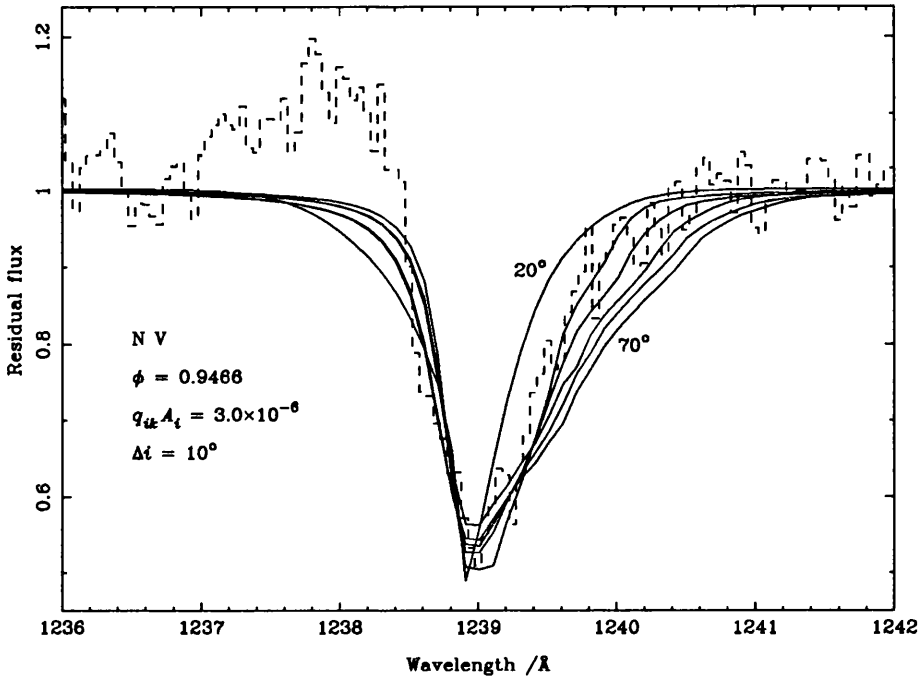

Figure 5.4: *Synthetic N V profiles at various inclinations for CX Dra observed at phase* $\phi = 0.9466$.

superions yield limits in excellent agreement with the result for nitrogen.

This is, however, in disagreement with the inclination of 15.°5 deduced from the velocity variations of the Fe III (UV 34 multiplet) in section 3.4. The fact that the iron line velocities are always less than those of more highly ionized species points again to the spatial separation of the different ionization stages as its root cause: twice-ionized iron is supposed only to exist in the more slowly-moving plasma away from the faster N^{4+}, C^{3+}, Si^{3+} and Al^{2+}, producing a lower-amplitude velocity curve and reconciling the model and the observations. Therefore, the higher ionization stages of other elements are likely to prove more reliable as indicators of inclination by profile-fitting as they trace out the more energetic parts of the stream where the velocities are consequently greater. This conclusion is also borne out by the observed velocity width ratio, which is such that $1.68 \lesssim \xi_{\mathrm{N\,V}}/\xi_{\mathrm{Fe\,III}} \lesssim 2.30$ over all phases,

indicating a smaller spread in velocities for iron, and hence a different spatial origin.

Figure 5.5 shows the derived abundance parameters $\log_{10}(q_{ik}\,A_i)$ as functions of phase for each of the four species N V, C IV, Si IV and Al III observed in CX Dra. The most immediately apparent feature of these figures is the almost-discontinuous rise in the parameter by several orders of magnitude in some cases near phase ~ 0.5. This can be attributed to phase variations in either (or both) of the parameters q_{ik} and A_i. As the photospheric contribution to the lines has been removed, variations in A_i imply that there is mixing going on between the streaming material and the outer photospheric layers of the primary, diluting the abundances seen in the post-impact plasma ($\phi \lesssim 0.5$) relative to the uncontaminated material ($\phi \gtrsim 0.5$). However, a far more likely hypothesis is that this sudden variation is due to the appearance of the impact region over the stellar horizon. In this interpretation, the total fraction of each element is constant but approximately one hundred times more N V (for example) is produced by the shock-ionization of the stream on the photosphere than elsewhere. This also explains the second feature which is the obvious correlation between the size of the discontinuity and the ionization potential of the ion. N V can only be produced in extreme conditions near the 'hotspot' and so is strongly phase-dependent, but Al III with its lower ionization potential, already abundantly populates the stream and the circumstellar material and shows a much weaker variation. Intermediate ions show discontinuities of intermediate magnitude. This could, in principle, be verified (or otherwise) by searching for variations in adjacent ionization stages. Unfortunately, there are no useful lines of N VI in the *IUE* spectral range, the λ1718 line of N IV is not present, possibly indicating the direct ionization of N III to N V by the Auger process, and although lines of C III, Si II and Si III do exist (and the last two are seen to vary), photospheric contamination is so great that a 'clean' removal of these effects is impossible and any correlation between ions is completely masked.

The third feature of figure 5.5 is the drop in the value of the abundance parameter at the 'stream-dipping' phase, $\phi \sim 0.75$. The density-*in*dependence of the scattering

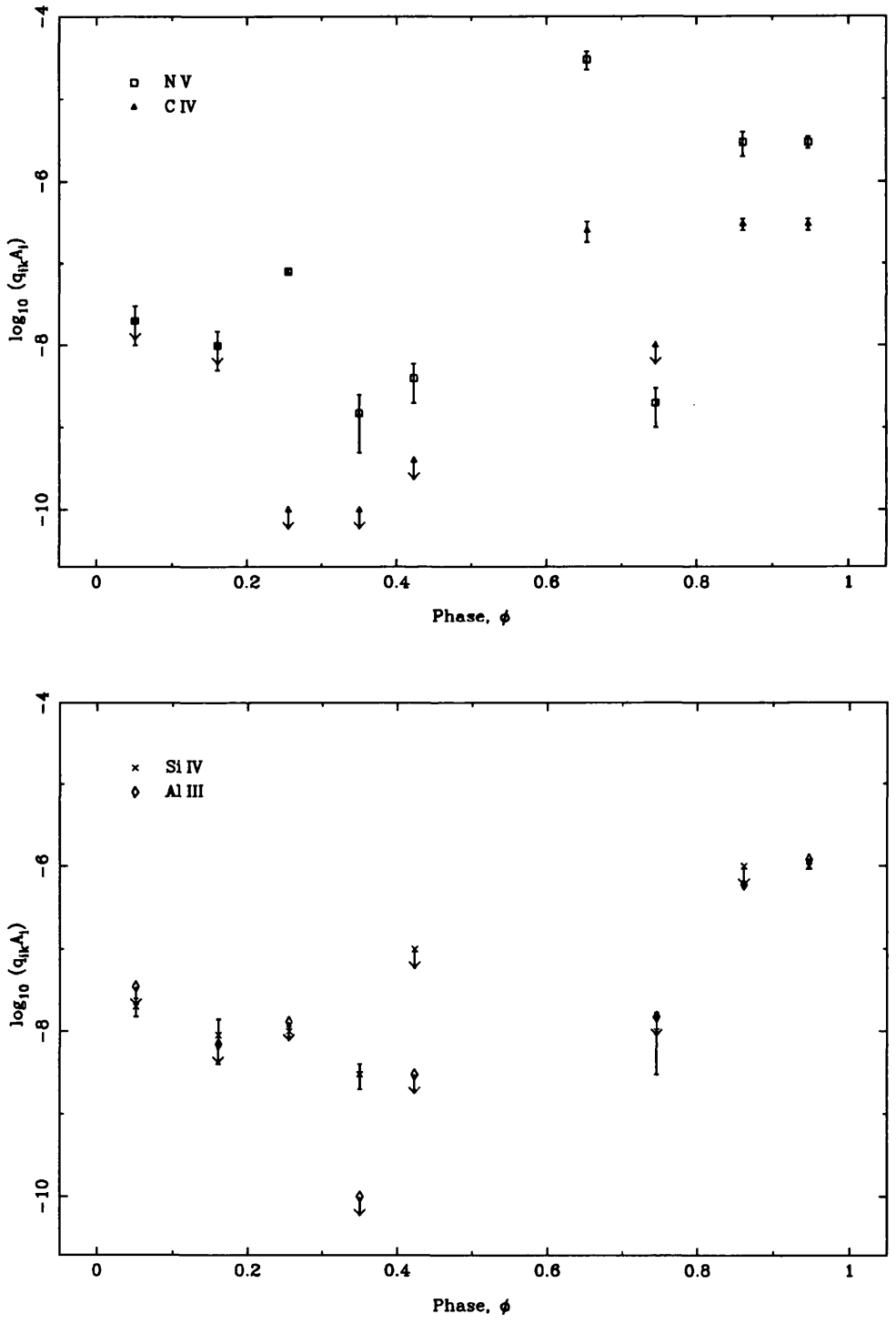

Figure 5.5: *Phase variation of the abundance parameter $q_{ik}\,A_i$ for various observed ions. (Arrows indicate upper limits).*

process would seem to argue against the reality of the 'stream-dipping', as a drop in the stream scale-height is a property of the spatial density distribution, not of the *relative* abundance of any element. However, such a precipitous density drop (if it exists) would naturally have repercussions for the ionization balance of the gas and so it still remains to be seen whether the stream really does 'dip' or whether the secondary undergoes periods of reduced (or zero) mass transfer. Against this latter proposal is the fact that the two observations of this effect, seen at different epochs, appear at almost the same phase and yet have not been seen at any other phase, particularly at one between the two epochs.

To derive the abundances of the material in the stream of CX Dra and U Cep, the fits to the greatest columns of material at $\phi = 0.9466$ (SWP 9996) and $\phi = 0.9022$ (SWP 4457) respectively were used to extract the value of $\log_{10}(q_{ik}A_i)$ for each ion, and the ionization fractions, $q_{i,k+1}$, were computed from the ionization ratios

$$\frac{N_{i,k+1}}{N_{i,k}} = \frac{(W(r)/n_e)\,R_{k,k+1} + C_{k,k+1}}{\alpha^{\rm rad}_{k+1,k} + \alpha^{\rm diel}_{k+1,k}}$$

where $R_{k,k+1}$, $C_{k,k+1}$, $\alpha^{\rm rad}_{k+1,k}$ and $\alpha^{\rm diel}_{k+1,k}$ are the rate coefficients of photoionization, collisional ionization, and radiative and dielectric recombination respectively. These were computed using the fit coefficients to the ionization and recombination rates of Shull & van Steenberg (1982) and the photoionization rates of Harmann (1980), the dilution factor is given by

$$W(r) = \frac{1}{2}\left(1 - \sqrt{1 - \frac{R_*^2}{r^2}}\right)$$

for a distance r from a star of radius R_*, and n_e is the local electron number density. The photoionization effects of the dilute radiation field of the primary are included because, although the higher ionization stages are collisionally dominated, the lower stages are affected by photoionization, and so will in turn have an influence on the ionization fraction of any given ion. Computations were performed with the value of the electron temperature at 10^5 K and an electron density in the range

	CX Dra	U Cep
$T_{\rm rad}(\lambda < 504\,\text{Å})$	11 500 K	6 800 K
$T_{\rm rad}(504\,\text{Å} < \lambda < 912\,\text{Å})$	12 800 K	6 800 K
$T_{\rm rad}(\lambda > 912\,\text{Å})$	19 000 K	11 250 K

Table 5.1: *Adopted radiation temperatures for the ionization balance calculations of CX Dra and U Cep.*

10^6–$10^{10}\,\text{cm}^{-3}$, consistent with the presence of N V in the spectra and with the results of Peters & Polidan (1984) for their analysis of the impact region in CX Dra, and with the analysis of Plavec (1983) of the circumstellar disc of U Cep. Radiation temperatures were derived from black-body fits to Kurucz model atmospheres over the appropriate wavelength regions (below the helium ionization edge at $\lambda\,504$, above the hydrogen ionization edge at $\lambda\,912$, and at intermediate wavelengths) and are given in table 5.1, and the circumstellar material was assumed to be at the representative distance of $1.5\,R_*$.

The results for both systems are given in tables 5.2 and 5.3 where the derived elemental abundances and their logarithmic depletions, D, relative to the normal Solar values (Duley & Williams 1984) are listed. Unfortunately, no atomic data on Al III could be found, preventing the abundance of aluminium from being derived.

Both systems show a large increase in nitrogen content and a reduction in carbon over the Solar values. This strongly suggests that the transferred material has experienced a degree of CNO-processing. The expected values for material in CN-equilibrium but not in NO-equilibrium are a +0.66 dex overabundance in nitrogen and a −1.60 dex underabundance in carbon (Clayton 1968). As the CNO bi-cycle progresses, all CO nuclei are eventually converted to N and this seems to be what is happening in CX Dra and U Cep. (The absence of the O VI $\lambda\lambda$ 1032, 1038 line cannot

Ion	$\log_{10}(q_{ik}A_i)$	$\log_{10}(q_{ik})$	$\log_{10}(A_i)$	$\log_{10}(A_i)_\odot$	D
N V	−5.44	−2.68	−2.76	−3.94	+1.18
C IV	−6.44	−0.46	−5.97	−3.43	−2.54
Si IV	−5.92	−1.77	−4.16	−4.46	+0.31
Al III	−5.84	—	—	−5.60	—

Table 5.2: *Derived elemental abundances for the streaming material in CX Dra.*

Ion	$\log_{10}(q_{ik}A_i)$	$\log_{10}(q_{ik})$	$\log_{10}(A_i)$	$\log_{10}(A_i)_\odot$	D
N V	−5.14	−2.68	−2.46	−3.94	+1.48
C IV	−4.92	−0.47	−4.45	−3.43	−1.02
Si IV	−5.92	−1.82	−4.10	−4.46	+0.36
Al III	−5.62	—	—	−5.60	—

Table 5.3: *Derived elemental abundances for the streaming material in U Cep.*

be used to test this hypothesis as temperatures of at least 3×10^5 K are required to produce significant amounts of O VI and no trace of the O V λ 1371 line can be found, this stage possibly being circumvented, as for N IV, by Auger ionization).

The derived abundances of CN are in excellent agreement with those found by Peters & Polidan (1984) for CX Dra, but are in discord with the much lower level of nuclear burning (only 75 % CN-processed) deduced by Plavec (1983) from ultraviolet emission lines and by Parthasarathy, Lambert & Tomkin (1983) from visual spectra in U Cep. The silicon abundance is in agreement (to within the expected errors of $\sim \pm 0.4$ dex) with the Solar value for both CX Dra and U Cep.

It is worth stressing at this point that the ionization fractions used here and by Plavec are very sensitive functions of electron temperature. A change of 0.1 dex in the temperature produces a change of $\sim$ 1.0 dex in the derived nitrogen depletion, and a change of just under 0.4 dex in that of silicon and carbon. The depletions are completely insensitive to the electron density over the range considered here. Yet the requirement that these superions be *simultaneously* present in the circumstellar material seems to accurately constrain T_e to a value very close ($\pm$5000 K) to 10^5 K. The turbulent nature of the accreting column and post-impact region argues against any sustainable temperature or abundance stratification, further defeating any attempt to explain these extreme abundances. Nevertheless, it is possible that whilst the region may be homogeneous in a large-scale, statistical sense, on smaller scales the turbulent cells and, in particular, any shocks that may be present could have a significant effect on the appearance of the lines (e.g. Lucy 1982). Any extra source of ionizing radiation not accounted for in the computations of q_{ik} could reduce or remove these abundance 'anomalies' too, for example, Auger ionization of material near the impact zone by X-rays produced in the accreting shock and/or boundary layer between the partial disc and the primary. This would have the effect of increasing the ionization fractions of the superions and hence reducing their abundances. Whilst potentially removing the nitrogen and silicon 'anomalies', this enhanced ionization *in*creases the derived depletion of carbon, and could cause O VI to appear where none is observed. Obviously, the reality of the situation is extremely complex.

In summary, the abundances derived for the common elements of the two interacting binary systems CX Dra and U Cep are *suggestive* of an advanced stage of CNO-processing in the secondaries; a more detailed treatment of *all* of the physical processes affecting the ionization balance is required before firmer conclusions can be drawn.

Chapter 6

Polarization in Algols

> ...there's information in the polarization ... All that frenetic switching between left and right means something. It's not just random noise.
>
> *Contact — Carl Sagan*

6.1 Introduction

Whilst spectroscopy is undoubtedly one of the most powerful tools available to the astronomer, it is by no means *all*-powerful. In the study of binary stars in particular, it is capable of revealing a great deal about binary motion but it fails in one important aspect: it is impossible to extract the orbital inclination of non-eclipsing binaries from spectroscopic data. Only in eclipsing systems where the inclination is close to 90° can the true values of such critical parameters as mass, radius and orbital separation be obtained. For this reason, other techniques must be used when embarking upon a complete analysis of single- and double-lined binary systems.

When light is scattered it becomes polarized, and if a collection of scatterers has a geometry which departs from axial symmetry about the line-of-sight to the source of the radiation, then there will be an excess of polarization in the plane

perpendicular to the asymmetry direction. Thus polarization carries information about the orientation of the scatterers projected onto the sky, and their spatial distribution.

As the binary system rotates, any static or quasi-static (non-axially symmetric) distribution of scatterers as seen from Earth rotates along with it, producing "phase-locked" variations in the intrinsic polarization. The first observations of such an effect were made by Shakhovskoi (1965) in a sample of Algol systems.

In interacting and Algol-type binary systems, the dominant polarization mechanism is likely to be isotropic scattering from free electrons, in particular, electrons produced by shock-ionization of the plasma in a matter stream. Kemp *et al.* (1986) model the eclipse of ε Aur with an opaque, tilted disc about the primary, and a similar geometrically- and optically-thick disc is proposed by Piirola (1980) to explain the observed polarization in U Cep. The observed polarization variations of CX Dra in the visible region are at the 0.1% level (Huang, Hsu & Guo 1989) and, as demonstrated below, are only attributable to some extended (i.e. circumstellar as opposed to stellar) scattering medium.

6.1.1 Possible sources of polarization

In 1946, Chandrasekhar demonstrated that high levels of polarization (up to approximately 11%) are obtainable from *plane-parallel*, grey, pure-scattering stellar atmospheres, arising from gradients in the embedded radiation field. However, it is readily apparent from symmetry arguments that a spherically symmetric-star has *zero* polarization, all scattering angles being equally represented. Some form of asymmetry is therefore required to produce any polarization at all.

Sizeable values of polarization are attainable, for example, if the star is distorted by rotation. However, Haisch & Cassinelli (1976) and Collins (1970) have modelled these effects numerically and found that only for stars with highly flattened envelopes (i.e. those seen equator-on *and* rotating at speeds close to their critical break-up speed) can substantial (i.e. $\gtrsim 0.5\%$) polarization be generated. The value

of $v \sin i = 180\,\mathrm{km/s}$ for CX Dra (Slettebak 1982) implies that one of the above conditions applies but probably not both.

Collins (1970) has shown that the wavelength dependence in the *non-grey* case is quite severe. The polarization is expected to be greatest where the gradient of the source function near the stellar surface is greatest, implying that for OB stars, the maximum occurs at ultraviolet wavelengths and falls away rapidly towards the visual region of the spectrum where values of substantially less than 0.03% are obtained.

The late-type secondary is a potential source of polarization too. Schwarz & Clarke (1984) and Clarke & Schwarz (1984) have observed wavelength-dependent polarization in Betelgeuse (α Ori) of magnitude $\sim 0.4\%$ at 4000 Å falling to 0.04% at $\sim 1\,\mu$m which they model with a hot photospheric convection cell enhancing polarization in the overlying scattering layers. However, surveys of late-type stars have shown that their polarization is strongly dependent on their luminosity class (Clarke, Schwarz & Stewart 1985) and spectral type (Tinbergen 1982) to the extent that the 1% polarization in late-K and M-type *super*giants decreases to less than 0.01% for F0 giants. This fact, coupled with the faintness of the secondary star in CX Dra (see section 6.2), makes it unlikely that it can contribute significantly to the observed polarization.

Polarization due to light reflected from the inner faces of stars in a binary system is also likely to be quite small. Kemp *et al.* (1981) estimate that such polarization can only reach $\sim 0.01\%$ if the reflecting surface is *substantially* heated by the companion star, and otherwise is much smaller.

If neither the stellar photosphere nor the presence of a companion can produce the observed astronomical sources of variable polarization with magnitudes of several tenths of a percent, then it is probable that a more extended, asymmetric circumstellar 'cloud' is responsible.

Monte Carlo simulations of polarization by electron scattering (Daniel 1980) have shown that substantial polarizations (greater than 1 %) are possible even in modestly oblate circumstellar distributions of scatterers ($e \sim 0.85$). Given the (growing)

suspicion that CX Dra has such a 'cloud', the generation of models of the polarization from the expected particle distribution will be the subject of this chapter.

6.2 Polarization theory

It is probable that the gas stream circling the primary of CX Dra is quite tenuous and so the *scattering* optical depth should be less than unity. This means that the analytic models of Brown, M^{c}Lean and Emslie (1978, hereafter BME) of polarization in the optically-thin limit can be used. BME have developed a description of the polarization produced by an arbitrary distribution of scattering electrons in terms of a series of directional moment integrals over the electron number density. The first moment is in the form of a scattering optical depth (equation 6.1), and the others describe the clustering of the scatterers about various co-ordinate planes which pass through the source(s) of unpolarized light (equations 6.2).

There are two potential sources of unpolarized light in CX Dra: the primary and the secondary stars (ignoring the possibility of thermal emission from any circumstellar material and the probable distortion of the secondary). Their relative contributions to the total light (and hence to the polarization) from the system are

$$\frac{\text{Flux of light } \textit{at scatterers} \text{ due to primary}}{\text{Flux of light } \textit{at scatterers} \text{ due to secondary}}$$

$$\underset{\sim}{\text{typically}} \quad \frac{4\pi R_1^2 \sigma T_1^4 / 4\pi R_s^2}{4\pi R_2^2 \sigma T_2^4 / 4\pi A^2}$$

$$= \quad \left(\frac{r_1}{r_2 r_s}\right)^2 \left(\frac{T_1}{T_2}\right)^4$$

where T_1, T_2, r_1 and r_2 are the temperatures and fractional radii of the primary and secondary respectively, r_2 is assumed to equal the radius of the secondary's Roche lobe and r_s, the typical radius of the scatterers about the primary, is taken to be equal to the radius of the primary's Roche lobe. With Koubský's values of the primary

mass, $M_1 = 7\mathrm{M}_\odot$, and the mass-function $f = 0.031389\,\mathrm{M}_\odot$ (Koubský 1978), the Roche lobe radii were calculated from the formula of Paczyiński (1971). Together with surface temperatures of $T_1 = 19\,000\,\mathrm{K}$ and $T_2 = 6\,500\,\mathrm{K}$, and a primary radius of $R_1 = 4.6\,\mathrm{R}_\odot$ (Koubský 1978), the value of the above ratio was found for various orbital inclinations ranging from $i = 20°$ to $i = 70°$. Values from ~ 65 to ~ 95 are obtained, showing that for all reasonable inclinations the secondary makes a negligible contribution to the total light from the system. (This does not include reflection effects which have, in any case, been shown to be of minor importance).

The expressions for the direction moments of BME for a single source are therefore

$$\tau_0 = \frac{3\sigma_\mathrm{T}}{32\pi} \int_V \frac{n_\mathrm{e}(x,y,z)}{(x^2+y^2+z^2)} D(x,y,z)\,dx\,dy\,dz \tag{6.1}$$

and

$$\left.\begin{matrix}\tau_0\gamma_0\\ \tau_0\gamma_1\\ \tau_0\gamma_2\\ \tau_0\gamma_3\\ \tau_0\gamma_4\end{matrix}\right\} = \frac{3\sigma_\mathrm{T}}{32\pi} \int_V \frac{n_\mathrm{e}(x,y,z)}{(x^2+y^2+z^2)^2} D(x,y,z) \left\{\begin{matrix} z^2\\ xz\\ yz\\ x^2-y^2\\ xy\end{matrix}\right\} dx\,dy\,dz \tag{6.2}$$

where σ_T is the Thompson cross section for electron scattering, n_e is the electron number density, V is the volume under consideration (effectively infinite), and $D(x,y,z)$ is the "finite star depolarization factor" of Cassinelli *et al.* (1987) which corrects the equations of BME for the fact that a (spherically symmetric) star of finite extent will dilute the observed polarization relative to the point source model;

$$D(x,y,z) = \left(1 - \frac{R_1^2}{x^2+y^2+z^2}\right)^{\frac{1}{2}}. \tag{6.3}$$

Notice how each shape factor is weighted by a simple function which selects a preferred direction in space so that any tendency for the distribution of scatterers

to lie in one of these directions is reflected in an enhanced value of the appropriate shape factor, e.g. if γ_2 is large compared to γ_1, the scatterers are localized parallel to the x-axis to a greater extent than they are localized parallel to the y-axis.

In the evaluation of the above integrals, allowance is also made for the other effect of a finite star, i.e. that of 'shadowing'. Scattering material occulted by the disc of the primary is not included in the calculation, making the shape factors τ_0 and γ_0–γ_4 phase-dependent.

The electron number density is presumed to be directly proportional to the total number density of all particles and to have the vertical Gaussian distribution given by equation 4.3. The absolute scale of n_e is derived from the known timestep of the model of the binary system and the mass transfer rate at L1 which is a free parameter of the polarization model. The assumption $n_e \sim n_H$ is also implicit in the model and is probably a good assumption given the highly ionized state of the plasma. Thus by matching the amplitude and shape of the observed polarization variations to those of the model, the geometry and the absolute electron number density scale (and thence the mass transfer rate) of the scatterers can be found.

The 3-D integrals over the volume of the model were performed using the "alternative extended Simpson's rule" (Press *et al.* 1988) which was accurate to better than 0.1% in tests simulating a single point-particle in orbit about the primary.

From the shape factors, the Stokes' parameters I, Q and U can be calculated (the fourth parameter, V, which is concerned with the circularly-polarized component, is zero as it is impossible to produce circularly-polarized light from the electron scattering of unpolarized light). BME give the following formulae for I, Q and U.

$$\begin{aligned} I &= I_0 [1 + \tau_0 \{2(1+\gamma_0) + (1-3\gamma_0)\sin^2 i \\ &\quad + \sin 2i (\gamma_1 \cos\phi + \gamma_2 \sin\phi) \\ &\quad + \sin^2 i (\gamma_3 \cos 2\phi + \gamma_4 \sin 2\phi)\}] \qquad (6.4) \\ Q &= \tau_0 \{(1-3\gamma_0)\sin^2 i + \sin 2i (\gamma_1 \cos\phi + \gamma_2 \sin\phi) \\ &\quad - (1+\cos^2 i)(\gamma_3 \cos 2\phi + \gamma_4 \sin 2\phi)\} \qquad (6.5) \end{aligned}$$

$$U = -2\tau_0 \{\sin i (\gamma_1 \sin \phi - \gamma_2 \cos \phi) + \cos i (\gamma_3 \sin 2\phi - \gamma_4 \cos 2\phi)\} \quad (6.6)$$

(BME use λ, the longitude of the secondary relative to the primary as seen projected onto the sky, as their phase-parameter instead of ϕ, the binary phase as seen by an external observer in the orbital plane. The two measures are related by $\lambda = -\phi$ and this produces the above sign-changes in the odd terms of the BME equations for Q, U and I to give equations 6.4–6.6).

There are several general points to be noted when comparing the models and the observations.

Firstly, the observed locus does not lie in the same place or at the same orientation as the computed locus. This is for two reasons. The first is the polarizing effect of the interstellar medium which produces a constant shift of the 'stellar' locus—in fact, the shift has an extra intrinsic term from equation 6.5 which brings the total shift to $(Q_I + \tau_0 (1 - 3\gamma_0) \sin^2 i, U_I)$. This must be removed first (as it was imposed last) before allowance can be made for the second effect which is due to the orientation of the system as seen on the celestial sphere. This causes a rotation of the data about an angle of $2\theta_0$ where θ_0 is the projection of the reference plane (in this case the orbital plane) onto the sky. (The factor of 2 arises because all angles are doubled in the Q-U plane). Rotating the data into alignment with the model permits the scale of the data, τ_0, to be fitted. The shape factors are inherent in the model, and the extraction of γ_0 finally allows the true interstellar components to be found.

6.3 Preliminary Results

The results of the computations (with the points of quadrature and conjunction marked) are cast in the form of the Stokes parameters for comparison with the observed data (figure 6.2 and 6.1 respectively shown below). The model is for CX Dra, seen at an inclination $i = 50°$ and with a mass transfer rate of $\dot{M} = 10^{-10} M_\odot/yr$.

There is an obvious elongation of the data in one direction (called the stellar

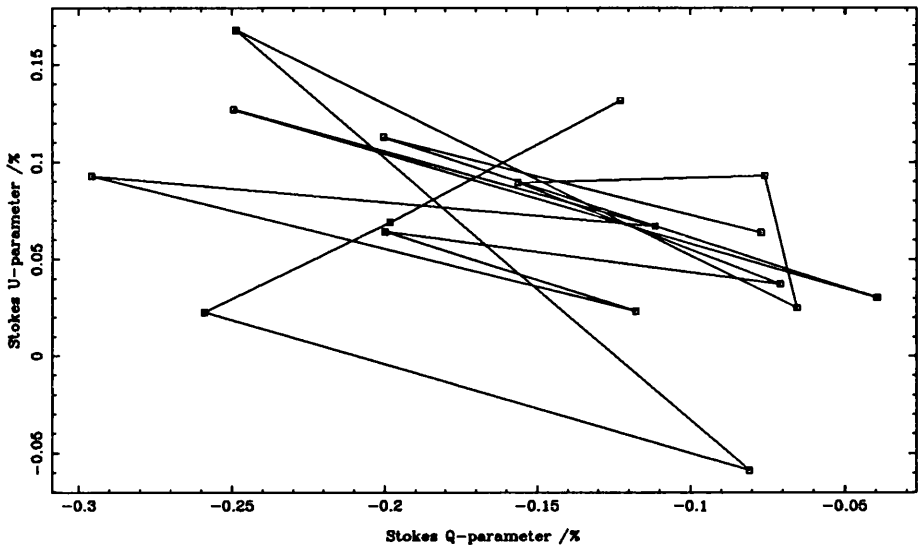

Figure 6.1: *CX Dra Q-U data from Huang, Hsu & Guo (1989). The data have been connected in phase order (Koubský's 1980 ephemeris). Note the tendency to lie parallel to the equatorial line.*

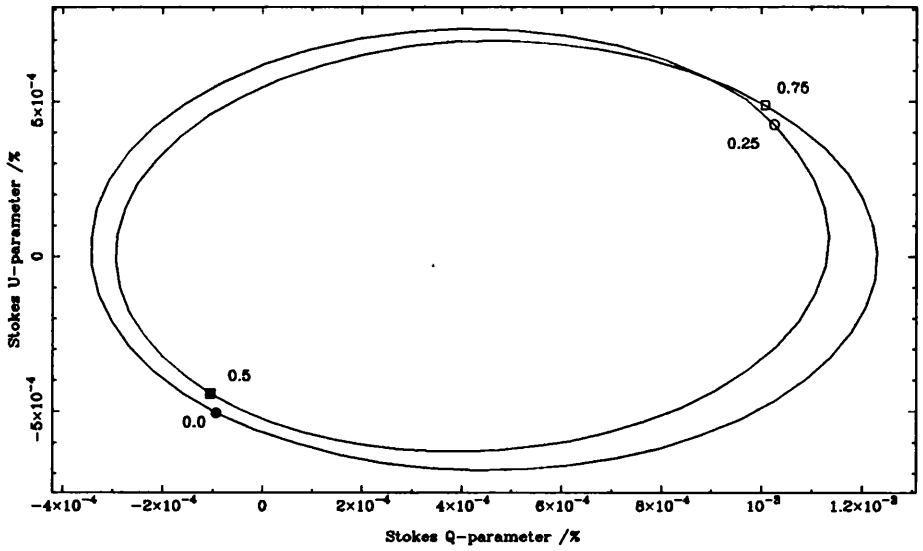

Figure 6.2: *Computed Q-U locus for the optically-thin model of CX Dra, with* $i = 50°$ *and* $\dot{M} = 10^{-10}\, M_{\odot}/yr$. *The sense of circulation of the model is clockwise.*

intrinsic line or SIL; Clarke & M^{c}Gale 1987) at an angle of $\sim 155.^\circ6$ (or $-24.^\circ4$) to the positive Q-axis. It is especially noticeable when the data are joined in phase order (see figure 6.1). The SIL is also known as the equatorial line because it lies parallel to the projection onto the sky of the stellar equator (and hence to the orbital plane of the binary). Thus the orbital plane lies at an angle of $155.^\circ6/2 = 77.^\circ8$ to the equatorial (sky) reference frame used by the observers. The alternative angle can be ruled out by a comparison of the positions of the quarter-phase points in the data and the models.

The SIL in the model of CX Dra corresponds to the positive-pointing part of the major axis of the ellipse. Any deviations from a smooth ellipse traced out twice (as predicted by BME) are due to the phase-dependence of the shape factors derived for this model introducing a variable phase-shift between the fundamental and second harmonic of the Stokes parameters.

The fitted locus gives an electron density scale for the model of $1.48 \times 10^9\,\mathrm{cm}^{-3}$ and the interstellar components are quoted elsewhere (see table 6.6).

Secondly, the pairs of values of the polarization at quadrature ($\phi = 0.25, 0.75$) and at conjunction ($\phi = 0.0, 0.5$) are slightly different ("split"). In the model, this is due once more to the induced phase shift and to the asymmetric distribution of scatterers between these phases. In the observations however, the splitting is considerably larger and in much poorer alignment perpendicular to the SIL. The splitting is also quite variable in the data where the positions of the quarter-phases vary with the epoch of observation.

Thirdly, there is a considerable scatter of the observations about the model, far more than would be expected from observational error alone, especially in the light of the smooth behaviour of the computed Q-U locus.

Before proceeding with any attempts to refine the models further, it is important to establish whether or not this erratic behaviour of CX Dra is typical of interacting binaries in general or unique to this system.

6.4 The behaviour of the polarization of other Algol systems

Consider the following summaries of the three binary systems Algol, U Sge and AO Cas.

Kemp *et al.* (1981) have observed Algol (β Per) over hundreds of orbital cycles and have produced a well-defined Q-U locus from the polarization variations. However, the scatter in the data over the years is of the same order of magnitude as the variations themselves, i.e. $\sim 0.01\,\%$ and if the observations are plotted in the Q-U plane, the proposed double ellipse is by no means apparent.

The observations are dominated by a second harmonic as would be expected, but there is a significant fundamental mode present too which distorts the pure ellipse giving rise to a substantial quadrature splitting and is attributable to some breakdown in the mirror symmetry of the distribution of the scatterers about the orbital plane.

A model of Algol (from the viscous model of chapter 4 using the parameters of Richards & Bolton 1988; figure 6.3) shows a stream that impacts *almost* entirely onto the primary, the remainder going on to form a very weak stream that circles the primary and eventually escapes as a jet near $\phi \sim 0.3$. The derived Q-U locus (figure 6.4) shows a small difference in the ellipse lengths near either quadrature, an effect present but with increased size in the observed data. The locus also possesses substantial distortions near the stream eclipse ($\phi \sim 0.5$), which are not present in the observations.

U Sge has also been observed extensively (Rudy & Kemp 1978) and shows the same strong second harmonic in the Q-parameter as does Algol, but no significant fundamentals or harmonics in the U-parameter. The polarization varies with a semi-amplitude of $\sim 0.05\,\%$ and a scatter of the same order.

The size of the U-parameter variability is surprising as the strict BME models predict that for a system with $i = 90^{\circ}$ and mirror symmetry in the scatterers about

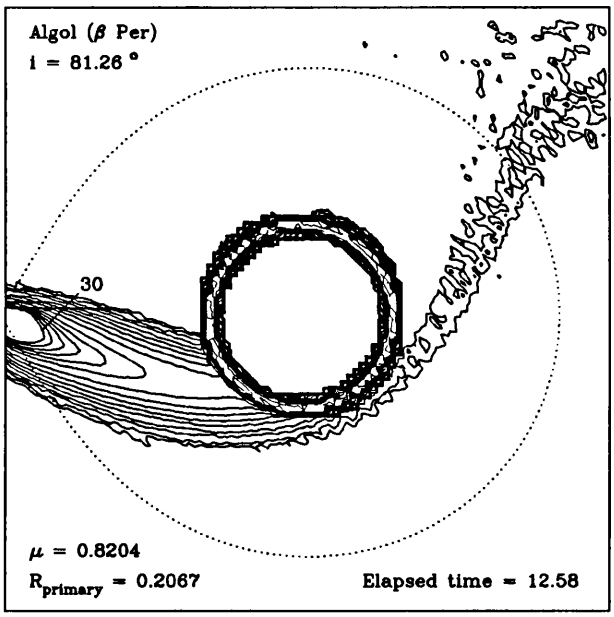

Figure 6.3: *Viscous model of Algol, showing the surface density. The contours are as in figure 4.4 with two more* (0.02, 0.01) *added, and are in units of particles per grid cell.*

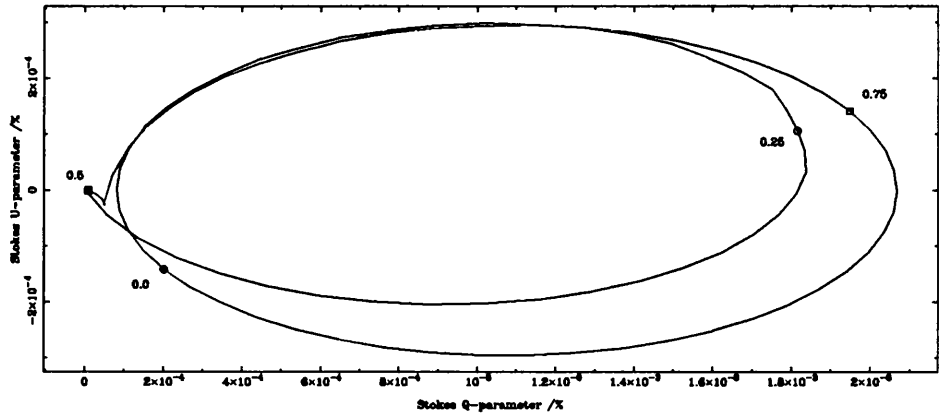

Figure 6.4: *The Q-U locus computed from the above model under the optically-thin assumption and a mass transfer rate of* $10^{-10} M_{\odot}/yr$. *The quarter-phase points are marked and the sense of circulation is clockwise.*

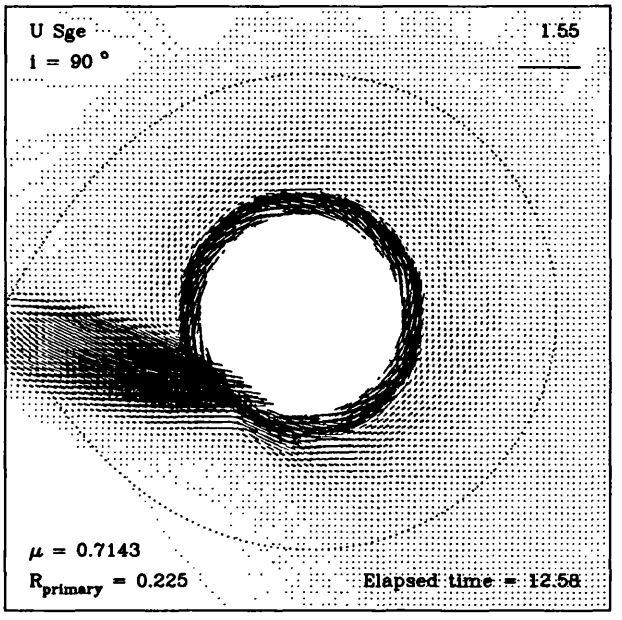

Figure 6.5: *Viscous model of U Sge, showing the velocity structure. The velocity scale is given in the top right-hand corner in dimensionless units.*

the orbital plane, the Q-U locus is expected to be a very narrow line parallel to the Q-axis. This is manifestly not so (see figure 6.8).

A model of U Sge (with parameters from M^{c}Namara & Feltz 1976; see figure 6.5) indicates that the infalling stream 'splashes' up from the impact region and forms a weak circumstellar disc. The modelled Q-U locus is a twice-traversed line in agreement with BME. As before, the model predicts strong variations near primary eclipse, but none are seen in the observations.

AO Cas is not an Algol system. It comprises two O8.5 III stars with similar masses. It is of interest here because of the significantly different geometry that it possesses when compared to Algols.

Rudy & Kemp (1976) obtained 38 observations over 20 orbital cycles and produced a Q-U locus with a scatter less than a third of the amplitude of the observed

variations, in marked contrast to the two systems listed above. They locate a scattering body on the advancing hemisphere of the more massive component and identify this with some effect of a matter stream between the two stars. Koch (1960) notes changes in the light-curve on the scale of days and small period jumps have been reported.

Schneider & Leung (1978) however, use a *UBV* photometric solution to show that AO Cas is a slightly over-contact system of two very similar stars whose light variations are due "...entirely to tidal distortion." In addition, the *IUE* spectra of AO Cas show no indication of matter streaming between the stars, only the P Cygni and sawtooth profiles typical of the wind of an O star (Stickland 1990). Profile "doubling" reported by M^{c}Cluskey & Kondo (1981) is almost certainly due to the *winds* of both stars being seen around quadrature.

6.5 Discussion

From the above reviews, several points emerge.

1. The interacting binaries examined here all have small but significant *fundamental* frequencies (i.e. variations on the orbital period) present in their Stokes parameters (AO Cas included).

2. The large scatter in the CX Dra data appears to be typical of Algol-type systems in general. Binaries with no appreciable gas streams (e.g. contact systems) have much less scatter in their data.

3. None of the data presented in the original analyses of the systems in the sample shows any effects due to the eclipsing of the streaming material.

Consider first points 2 and 3. A large scatter in the polarization observations seems to correlate with the presence of a gas stream in the system. An obvious explanation of this would be that the stream impact region is violently disrupted and 'splashes' of material are either ejected out of the orbital plane or into eccentric orbits about

the primary. Work by Clarke & M^{c}Gale (1986) on the stochastic appearance of polarizing clumps in the Q-U plane for various geometries has shown that considerable 'scatter' can be generated about the smoothed Q-U locus by non-co-rotating transient blobs such as might be expected to be thrown up by an impacting stream. No such scatter would be expected in contact systems where there is no energetic stream, and so it is seen that, at least empirically, this model goes a long way to explaining the highly variable observations. It is also possible that the eclipse of the main body of the stream at and just prior to $\phi \sim 0.5$ can be totally masked by these stochastic 'splashes'. Indeed, this effect would be most noticeable (and most effective at obscuring the eclipse) when the stream is in the state of minimum visibility during primary eclipse.

Point 1 is considerably more involved. The presence of a fundamental mode in the polarization oscillations indicates that there is a secularly stable asymmetry in the distribution of the scatterers about the orbital plane. In fact, the amplitude of the fundamental mode ($\gtrsim 10\,\%$ of the second harmonic for Algol and AO Cas and even greater for U Sge) means that the distortion is quite substantial.

Several candidate 'distorters' can be argued against on the grounds that repeatability of the observations is required. A twisted accretion disc or equatorial bulge could produce a first harmonic in the polarization but a warped disc is likely to precess causing the fundamental to drift in phase relative to the second harmonic, and any sizeable bulge on the surface of the contact member of an interacting binary will be either outside or very close to the Roche surface making it improbable that such a feature could be maintained. Magnetism (presumably generated by the rapid rotation of the primary) could support clumps of material out of the orbital plane and an oblique dipole configuration would certainly give rise to a fundamental mode in the polarization. However, as before, this is unlikely to remain 'phase-locked' for long, especially in view of the fact that the primary in Algol systems is often found to be rotating highly asynchronously.

An altogether more subtle and universal solution involves the proposition that in the gas streams and tenuous outer photospheric regions of interacting binaries, the *absorption* optical depth becomes large, even in the continuum. In a system observed from an inclination $\neq 90°$, only the upper surface of the stream would be seen, leading to an *apparent* asymmetry of material about the orbital plane. This solution applies equally well to the gas streams of Algols as to the tenuous Roche lobes near the L1 point in contact systems.

To model this effect accurately demands a substantial outlay in terms of solving the problems of radiative transfer for simultaneously scattering and absorbing media for the optically thick case (Buerger & Collins 1970). A zero-order solution to this problem consists of simply ignoring those scatterers deemed by some criterion to be at an optical depth greater than unity when evaluating the volume integrals (6.2).

An estimate of the absorption optical depth can be made using the electron density derived above, and although this has been derived under an optically thin assumption, the optically thick value for the density can only be larger (see section 6.6). With the approximation that the mean value over the system of the vertically-integrated density is of the same order as the hydrogen column with appropriate allowance for the inclination (a plane-parallel-type approximation), the absorption optical depth is given by

$$\tau_{\rm abs} \sim K(\nu)/\cos i \int_0^l n_{\rm H}\, dz$$

$$\sim K(\nu)/\cos i \sqrt{2\pi}\, \overline{n_{\rm e}\, H} \qquad (6.7)$$

where $K(\nu)$ is the bound-free absorption coefficient of hydrogen which is expected to be the dominant opacity source in early type stars and so will be used here for the purposes of estimation. Near the Lyman limit, $K(\nu) \sim 6.33 \times 10^{-18}\,{\rm cm}^2$ (Kopal 1981) and the mean value of the hydrogen column (assuming a pure hydrogen composition) is $\overline{n_{\rm e}\, H} \sim 2.97 \times 10^{19}\,{\rm cm}^{-2}$ for Algol and $6.79 \times 10^{19}\,{\rm cm}^{-2}$ for CX Dra modelled with $i = 50°$. Substitution into equation 6.7 yields the values $\tau_{\rm Algol} \sim 3080$,

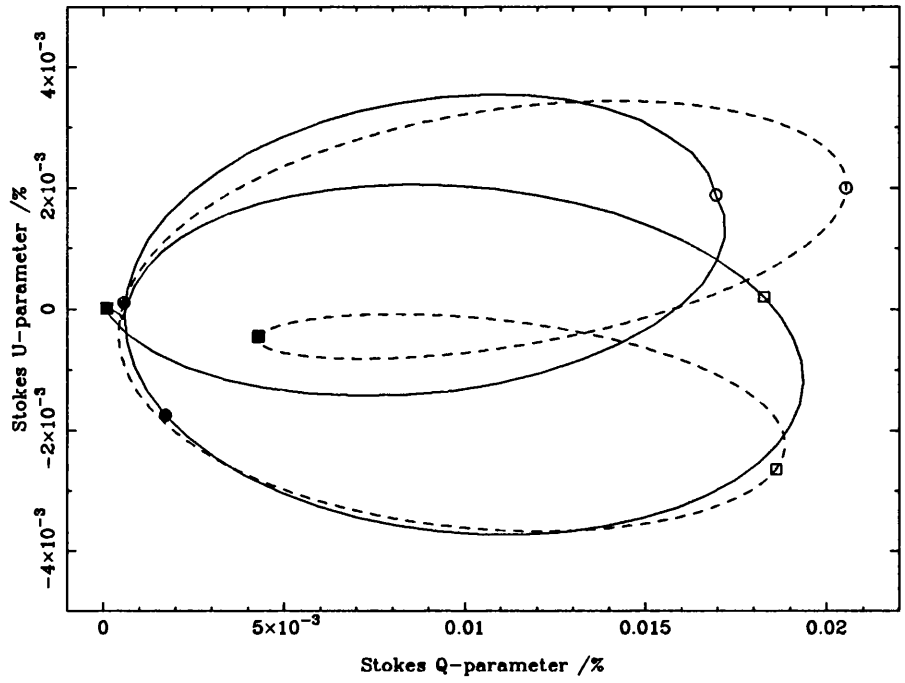

Figure 6.6: *Comparison of the data (dotted line) and the optically-thick model (solid line) for a mass transfer rate of* $1.9 \times 10^{-10}\, M_{\odot}/yr$. *The quarter-phase points are marked as before and the circulation of both models is clockwise.*

$\tau_{\mathrm{CX\,Dra}} \sim 1680$. Values for the opacity in the visual continuum are likely to be marginally larger than that given above for the Lyman limit; Gray (1976b) estimates that the visual continuum opacity is some 1.3 times greater than at the Lyman limit, leading to even larger absorption optical depths. It would seem reasonable therefore to proceed with the assumption that the circumstellar plasma is optically thin for scatterers but optically thick in absorption.

The viscous model of Algol used above was subjected to this zero-order optically-thick approximation by ignoring all the scatterers *below* the orbital plane. The new shape factors were used to derive a model Q-U locus which is shown below along with the smoothed fit to the data of Rudy & Kemp (1981) (see figure 6.6). Their fit has been rotated to lie along the eigenaxis of the model.

Several points are worthy of comment. Most noticeably, the quadrature splitting has been increased (over the optically thin model) and is now in excellent agreement with the observations, and although not shown, both loci are traversed in the same (clockwise) sense. Kemp *et al.* (1981) postulate asymmetric, flattened surfaces on the inner face of the secondary in Algol, giving rise to this quadrature splitting by reflection. This work shows that such *ad hoc* assumptions are rendered unnecessary with more refined modelling.

There is a small difference in the lengths of each modelled quadrature lobe, but in the opposite manner to that of their data. This can readily be accounted for by recalling that the 'data' are in fact points on a locus produced from Fourier transforms of the observations up to and including the second harmonics; one might therefore expect some small high-frequency deviations to be missing. Examination of the original observations *do* show a tendency for them to lie further from the mean value at $\phi \sim 0.75$ than the fitted model does, in quite good agreement with the model derived here.

Finally, the greatly enhanced distortion of the central loop is explained by the masking of the stream-eclipse by 'splashes' (described above). If the eclipse effects were to be removed from the optically-thick Q-U locus, it is apparent that the central loop would contract and the phase-points at $\phi = 0.75$ and 0.0 would advance into much closer alignment with the observations.

This much-improved fit of the optically-thick model compared to that of its optically-thin counterpart weighs heavily in favour of the former. Therefore, the optically-thick model has been adopted for the remainder of this chapter.

6.6 Results

Many of the physical parameters of Algol (and other systems) can be derived from the model fits in the following manner. Rotating the model of the Q-U locus of Algol onto the Fourier transform data gives that angle as twice the orientation of the system on the sky, and translating it into agreement with the data gives the (rotated)

interstellar component of the polarization. Notice that the constant value in the Q-parameter of BME of $\tau_0(1-3\gamma_0)$ is included in the model and so is kept separate from the interstellar component allowing the true value of the latter to be found. Scaling the locus to the data gives the τ_0-value (corresponding to scattering optical depth *not* the continuum absorption optical depth) and hence the mass transfer rate. The shape factors γ_0–γ_4 can be extracted directly from the model. Notice that the size of the optically-thick Q-U locus is reduced by a factor equal to the ratio of the volumes occupied by the optically-thick and optically-thin scatterers (in this model ~ 2), and consequently, to produce the same level of polarization, the density and hence the mass transfer rate must increase by the same factor over their optically-thin values. The final parameters for Algol are listed in table 6.6.

The variations of CX Dra in the Q-U plane are approximately an order of magnitude greater than those of Algol. This means that the density and mass transfer rate must be correspondingly higher, and so if Algol is most successfully modelled under this optically-thick assumption, then the stream of CX Dra is likely to be optically-thick too.

In fact, because the inclination is not close to 90° and because the material is more axisymmetrically distributed than in Algol, the shape of the Q-U locus barely changes between the optically-thick and thin cases. However, as outlined above, the density scale does. Taking the outermost points to describe a limiting envelope of the Q-U locus enables limits to be placed on the inclination of CX Dra: the paucity of data on this system does not allow an accurate determination of the parameters, merely upper and lower bounds to be set.

The sense of circulation in the observations is opposite (i.e. anticlockwise) to that of Algol, indicating that CX Dra is observed from "underneath", that is in the direction $\theta = 180° - i$ to the positive z-axis. The models have been adjusted to allow for this and now both circulate in the correct sense. As has already been noted, the orientation of the major axis of the loci (at 155.°6 or −24.°4) was chosen to match the looped structure seen in the data covering the third observing night of Huang,

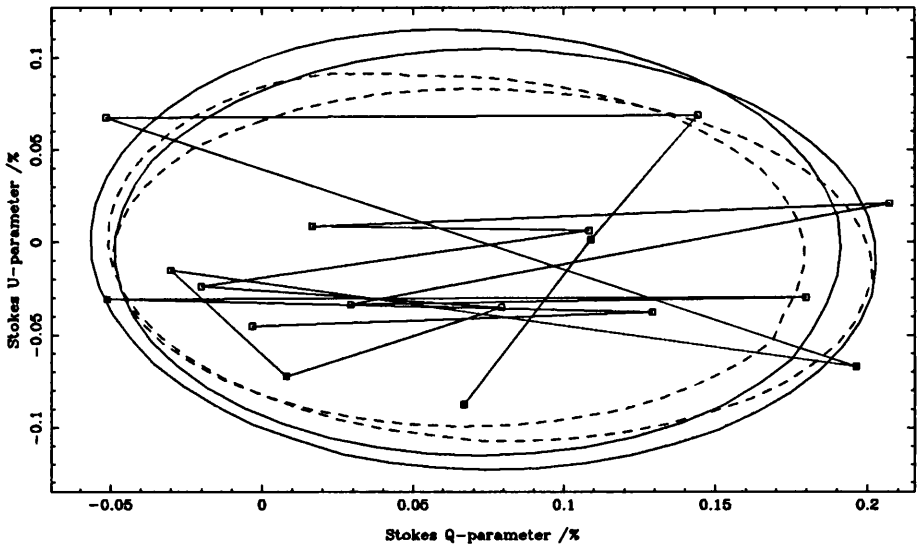

Figure 6.7: *Computed Q-U locus for CX Dra at inclinations of* 50° *(solid line) and* 60° *(dotted line) compared to the data. The circulation is in an anticlockwise sense.*

Hsu & Guo (1989) which closely resembled the model only if the orientation was set at 155.°6.

The derived parameters for the two limiting models are included in table 6.6 and the fits are shown in figure 6.7.

The fits to CX Dra show that $i > 50°$ but bearing in mind that CX Dra shows no sign of eclipses, $i < 65°$ is probably a reasonable lower bound (Koubsky 1978). The concentration of points towards the centre of the loci is probably an indication of a variable τ_0 changing the absolute scale of the ellipses. However, given the data as they stand leads to a mass transfer rate for CX Dra which is quite reasonable.

For the $i = 90°$ binary U Sge, the removal of the material below the orbital plane in order to simulate the effects of continuum absorption is not a valid procedure as the plane is seen edge-on. However in the spirit of the optically-thick assumption used above, a model with the material removed from behind a plane normal to the line-of-sight and passing through the centre of the primary is shown in figure 6.8.

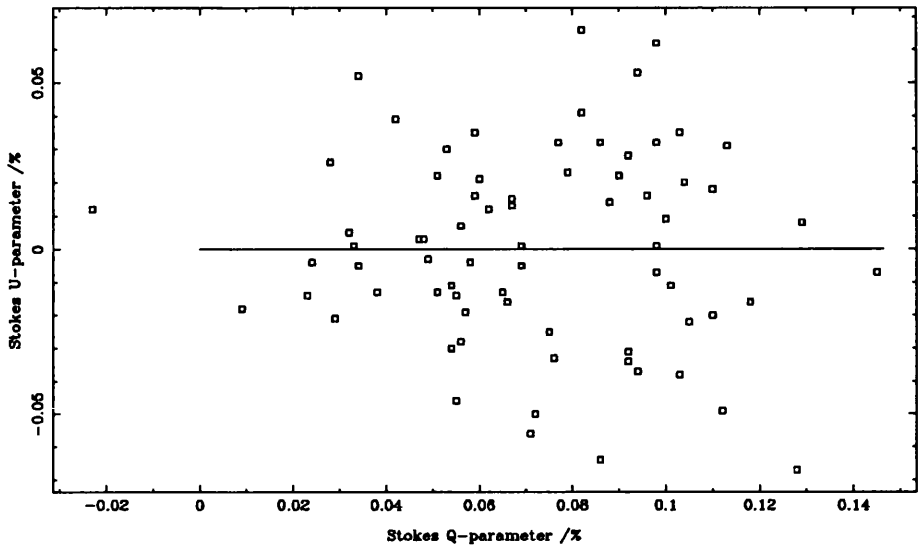

Figure 6.8: *Computed Q-U locus of U Sge superimposed on the observations of Rudy & Kemp (1978). The system is seen edge-on resulting in a linear Q-U locus.*

The model for U Sge does not fit the observations well: it is necessary to invoke the presence of 'splashes' (or other unknown effects) to explain the distribution of data in the Q-U plane. It is interesting though, that the only model to show strong 'splashing' (see figure 6.5) corresponds to the system with the largest polarization 'scatter'.

Given the lack of an obvious SIL, all that can be done is to derive a mass transfer rate by fitting the magnitude of the variations in the Q-parameter.

The absence of a preferred direction makes determination of θ_0 impossible and $(Q_{\rm I}, U_{\rm I})$ difficult, so a mean value for the interstellar components has been given below.

The interstellar polarization ($P_{\rm I} = \sqrt{(Q_{\rm I}^2 + U_{\rm I}^2)}$) for all systems investigated here is less than the upper limit of Spitzer (1978) which states that no interstellar component exceeds $9\,E\,(B-V)$. Values of $E\,(B-V)$ for Algol, CX Dra and U Sge respectively are $0\overset{\rm m}{.}03$ (Guinan, Koch & Plavec 1984), $0\overset{\rm m}{.}05$ (Hoffleit 1982) and $\sim 0\overset{\rm m}{.}09$ (Hoffleit 1982; Allen 1973), giving upper limits on $P_{\rm I}$ of $0.27, 0.45, 0.81\,\%$

System	Algol (β Per)	CX Dra		U Sge
Inclination, i	81.°26	50°	60°	90°
Position angle of SIL, θ_0	137.°0	77.°8	77.°8	—
Q_I /%	0.000	−0.100	−0.135	−0.192[a]
U_I /%	−0.003	0.024	0.036	−0.105
$\dot{M}$ /$M_\odot$/yr	1.9×10^{-9}	3.3×10^{-8}	3.7×10^{-8}	3.7×10^{-9}
τ_0 /%	0.0103	0.127	0.148	0.0792
γ_0	2.67×10^{-3}	3.18×10^{-3}	3.53×10^{-3}	—
γ_1	−0.0545	−0.0547	−0.0495	—
γ_2	−0.0207	−0.0348	−0.0341	—
γ_3	0.768	0.494	0.432	—
γ_4	0.416	0.509	0.503	—

[a]No correction has been made for the constant 'stellar' component, $\tau_0 (1-3\gamma_0) \sin^2 i$, as no value for γ_0 has been derived

Table 6.1: *Results of the optically-thick model fits.*

each of which is greater than the polarization deduced above.

The mass transfer rates are expected to be quite representative of the true rates (an accuracy of better than 50 % is likely given the constraints imposed by the modelling process) remembering that in Algol-type systems, the mass transfer rate is known to be variable. However the values derived in this work have an interesting correlation with the observed $v \sin i$ of the primaries. CX Dra which rotates more than twice as fast as the other two primaries (180 km/s (Slettebak 1982) as compared to 65 km/s and 76 km/s (Hoffleit 1982) for Algol and U Sge respectively), has a mass transfer rate an order of magnitude greater than the latter pair. This is not an unreasonable state of affairs considering that a larger mass transfer rate implies a greater transfer of angular momentum to the mass-gaining star and hence a larger rotational speed. Obviously, a larger dataset would be desirable.

Finally, the shape factors all imply highly-flattened circumstellar envelopes ($\gamma_0 \ll 1$) and a concentration or 'bulge' of material at phases $\phi = 0.0$ or $\phi = 0.5$ ($\gamma_1 > \gamma_2$), obviously due to the emergence of the stream from the L1 point. The thick stream of Algol and perhaps the escaping streamer force $\gamma_3 > \gamma_4$ implying a clumping of the material about the directions $y = \pm x$, whereas the more axisymmetric distribution of CX Dra give rise to $\gamma_3 \sim \gamma_4$. Shape factors have not been given for U Sge as no part of the geometry of the model can be fitted due to the large scatter in the data. Only the total scattering (measured by τ_0) can be derived with any certainty.

To conclude: the hydrodynamic models of chapter 4, when used to simulate the polarization variations observed in certain types of interacting binary, have demonstrated that it is possible to extract a great deal of important information concerning the geometry and structure of the matter streams therein, and on the polarizing effects of the interstellar medium.

Chapter 7

Conclusions

What is now proven, was only once imagin'd.

William Blake — Paradise Lost

7.1 Summary of the results and techniques

The foregoing analyses have served to bring to light many of the important, hitherto unknown properties of the Be star CX Draconis.

The deduction from visual observations that CX Dra is a non-eclipsing, interacting binary similar to the Algol stars, has been confirmed by a detailed analysis of forty ultraviolet spectra taken with good phase coverage. Maximum use has been made of the spectral information by the application of cross-correlation techniques with due allowance made for the contaminating effects of the circumstellar material. The derived orbital parameters are in excellent agreement with other studies. This bodes well for the future analysis of other Algol-type systems in this manner. Furthermore, knowledge of the details of the binary motion has enabled the effects of the photosphere to be removed (under an assumption concerning the lack of radiative coupling of the atmosphere and the circumstellar medium), permitting the streaming material to be studied in isolation.

Given the unencumbered view of the stream, it becomes possible to compare models with the picture of the system geometry derived from the velocity variations. Such a comparison leads to the rejection of a simple stream falling under the influence of gravity and rotation, in favour of a stream where viscous forces are important, thereby demonstrating that viscous effects *cannot* be ignored when modelling these kinds of flows.

Detailed hydrodynamic modelling has explained the presence of two curious features of the ultraviolet observations, namely the blue-shifted profiles seen in a narrow phase-region centred on $\phi \sim 0.3$, and the 'sudden' disappearance of almost all of the superions near phase $\phi \sim 0.7$. The former is due to the viscous support and subsequent ejection of a portion of the infalling stream at the observed phase, and the latter can be attributed to the vertical collapse of the stream in response to the rapidly-changing gravitational field it experiences near its closest approach to the primary. The possibility of a time-dependent mass flow cannot be ruled out, however the only known process which produces a (quasi-) periodic mass transfer rate, the Biermann-Hall effect (Biermann & Hall 1973), is thought to operate on a substantially longer timescale than that required by the observations. Further observations are necessary to distinguish between the latter two processes.

Synthetic line profiles have been shown to be in good agreement with the observations over regions where the stream is most dense, further confirming the velocity structure of the model and allowing abundances to be derived for several important elements. This analysis demonstrates that the circumstellar material has been CNO-processed (and, as such, necessarily originates in the secondary), and points out the need for a good model of the ionization structure of the stream, as the assumption of a homogeneous ionization balance throughout the stream is shown (not surprisingly) to be invalid. A lower limit on the inclination of the system to the line-of-sight has also been derived from these profile fits, and was found to be in agreement with the results of chapter 6.

Recently-published polarization data of CX Dra prompted the use of the vis-

cous models as analytic tools on these observations. By performing the appropriate integrals over the distribution of scatterers derived from the models, synthetic polarization variations have been created, and matching them to the data has enabled the derivation of such parameters as the inclination, the shape factors, the mass transfer rate, the contribution of the interstellar medium to the polarization, the orientation on the sky and even the perceived sense of binary rotation. Both the deduced mass transfer rates and the interstellar polarizations lie well within the expected limits for such parameters, the latter being wholly consistent with the observed reddenings of each system. The excellent fit to the polarization data for Algol shows that the models can explain the large observed quadrature splitting *without* recourse to arbitrary and unjustified geometric arguments. The lack of a credible fit (for U Sge) also indicates the kind of physical processes that are going on near the impact point, i.e. the 'splashing' of blobs of material. The stochastic nature of this process means that these observations can only be reproduced in some statistical sense.

The techniques developed and utilised above are generally applicable to most interacting binaries composed of non-compact objects, and there remain many systems that have not yet been examined for which an understanding of their present configurations could provide important evolutionary information.

7.2 Further work

It is expected that a great improvement in the synthetic profile fits can be achieved by the expediency of coupling the ionization balance computation directly into the calculation of the profiles instead of addressing the two processes separately, thus removing one of the main uncertainties in the fits of chapter 5. The effects of Auger ionization in the region local to the stream impact should be investigated to decide whether or not they can contribute significantly to the amounts of N^{+4} and C^{+3} observed in CX Dra. A potential test of this would be the reconciling of the CN abundances calculated from the ultraviolet and visual observations.

Further work is needed to ascertain the secular effects of the mass transfer on the

hydrodynamic models over time-scales which are an order of magnitude (or more) greater than those examined in this work. In particular, to determine whether the slow increase in total circumstellar mass is enough to damp out the 'jet' and form a stable disc, making the observation of such a feature in CX Dra a rare event, or whether the 'jet' is a permanent structure. If the latter is true, what are the restrictions (in mass ratio, primary radius and viscosity) on its formation? Recent observations of U Cep making the transition to a 'high' state of mass transfer show the appearance of such a 'jet' (Gimenez *et al.* 1990), another situation which is amenable to modelling by this method.

Calibrations of the mass transfer rates through the L1 point in these systems, permit an estimate of the amount of material that is transferred into the interstellar medium by Algol systems undergoing non-conservative mass transfer. Only two studies exist (Svechnikov 1973; Giuricin, Mardirossian & Mezzetti 1983), and they are in "serious" disagreement, partly because of the lack of a definitive value for the fraction of mass transferred into the ISM as a function of the important physical parameters of Algol systems. This parameter can easily be supplied by the aforementioned models.

One immediate consequence of the presence of a 'jet' is readily testable. The collimated outpouring of a quantity of material in the orbital plane should lead to an large, flattened, expanding and presumably cooling disc centred on the binary system. Infrared or radio polarization measurements should readily detect such a 'cloud' (indeed there is already some evidence for these structures, see sections 1.2.2 and 1.2.3), and the inclination of the system could be much more accurately determined from such an extended structure.

Knowledge of the inclination of binary systems is of critical importance because only then is it possible to determine the true values of the stars' masses and their orbital separation (if both components can be seen). Previous attempts to allow for the streaming material in Algol-like systems have been quite crude and the derived inclinations are consequently quite uncertain, but now that a more refined model

can be used to allow for the effects of the CSM, reliable inclinations can be found. The importance of this is that it becomes possible to obtain the present masses of stars whose mass has changed substantially over their hydrogen-burning lifetime. Comparison of these data and evolutionary models is obviously very desirable.

Bibliography

Allen, C. W., 1973. *Astrophysical Quantities*, Athlone Press, London, England.

Allen, D. A., 1973. *Mon. Not. R. astr. Soc.*, **161**, 145.

Ashok, N. M., Bhatt, H. C., Kulkarni, P. V. & Joshi, S. C., 1984. *Mon. Not. R. astr. Soc.*, **211**, 471.

Batten, A. H., 1974. *Publs. Dom. astrophys. Obs.*, **14**, 191.

Batten, A. H., 1976. *Structure and Evolution of Close Binary Systems, IAU Symp. No. 73*, eds. Eggleton, P., Mitton, S. & Whelan, J. J., pp. 303 ff., Reidel, Dordrecht, Holland.

Biermann, P. & Hall, D. S., 1973. *Astr. Astrophys.*, **27**, 249.

Bolton, C. T., 1989. *Algols, IAU Coll. No. 107*, ed. Batten, A. H., p. 311, Kluwer Academic Publishers, Dordrecht, The Netherlands.

Borra, E. F., Landstreet, J. D. & Mestel, L., 1982. *Magnetic Stars*, p. 191, Volume 20 of *Ann. Rev. Astr. Astrophys.*, Annual Reviews Inc., Palo Alto, California, U.S.A.

Bradt, H. V., Apparao, K. M. V., Clark, G. W., Dower, R., Doxey, R., Hearn, D. R., Jernigan, J. G., Joss, P. C., Mayer, W., McClintock, J. & Walter, F., 1977. *Nature*, **269**, 21.

Brown, J. C., McLean, I. S. & Emslie, A. G., 1978. *Astr. Astrophys.*, **68**, 415. (Paper BME).

Buerger, P. F. & Collins II, G. W., 1970. *Astrophys. J.*, **161**, 1025.

Cassatella, A. & Martine, T., 1990. *ESA IUE Newsletter*, in press.

Cassinelli, J. P., Nordsieck, K. H. & Murison, M. A., 1987. *Astrophys. J.*, **317**, 290.

Clarke, D. & McGale, P. A., 1986. *Astr. Astrophys.*, **169**, 251.

Clarke, D. & McGale, P. A., 1987. *Astr. Astrophys.*, **178**, 294.

Clarke, D. & Schwarz, H. E., 1984. *Astr. Astrophys.*, **132**, 375.

Clarke, D., Schwarz, H. E. & Stewart, B. G., 1985. *Astr. Astrophys.*, **145**, 232.

Clayton, D. D., 1968. *Principles of Stellar Evolution and Nucleosynthesis*, pp. 390 ff., McGraw-Hill, New York, U.S.A.

Cochrane, D. M. & McWhirter, R. W. P., 1982. Technical Report RL–82–099, Rutherford Appleton Laboratory.

Collins II, G. W., 1970. *Astrophys. J.*, **159**, 583.

Collins II, G. W., 1987. *Physics of Be Stars, IAU Coll. No. 92*, eds. Slettebak, A. & Snow Jr., T. P., p. 3, Cambridge University Press, Cambridge, England.

Coté, J. & Waters, L. B. F. M., 1987. *Astr. Astrophys.*, **176**, 93.

Cox, D. P. & Tucker, W. H., 1969. *Astrophys. J.*, **157**, 1157.

Coyne, G. V. & McLean, I. S., 1982. *Be Stars, IAU Symp. No. 98*, eds. Jaschek, M. & Groth, H.-G., p. 77, Reidel, Dordrecht, Holland.

Dachs, J., Engels, D. & Kaiser, D., 1988. *Astr. Astrophys.*, **194**, 167.

Dachs, J., Hanuschik, R., Kaiser, D. & Rohe, D., 1986. *Astr. Astrophys.*, **159**, 276.

Daniel, J. Y., 1980. *Astr. Astrophys.*, **86**, 198.

Duley, W. W. & Williams, D. A., 1984. *Interstellar Chemistry*, p. 9, Academic Press, London, England.

Dworetsky, M. M., 1989. Private communication.

Fireman, E. L., 1974. *Astrophys. J.*, **187**, 57.

Flannery, B. P., 1974. *Mon. Not. R. astr. Soc.*, **170**, 325.

Gerhz, R. D., Hackwell, J. A. & Jones, T. W., 1974. *Astrophys. J.*, **191**, 675.

Gimenez, A., Gonzalez-Riestra, R., Guinan, E., Kondo, Y., M^{c}Cluskey, G. E., M^{c}Cook, G. P., Dorren, J. D., Johanson, S. & Sahade, J., 1990. *Evolution in Astrophysics*, ESA Publications Division, Noordwijk, The Netherlands, in press.

Giuricin, G., Mardirossian, F. & Mezzetti, M., 1983. *Astrophys. J. Suppl.*, **52**, 35.

Grady, C. A., Bjorkman, K. S. & Snow Jr., T. P., 1987. *Astrophys. J.*, **320**, 376.

Gray, D. F., 1976. *The Observation and Analysis of Stellar Photospheres*, pp. 162–166, Wiley-Interscience, New York, U.S.A. (1976a).

Gray, D. F., 1976. *The Observation and Analysis of Stellar Photospheres*, p. 144, Wiley-Interscience, New York, U.S.A. (1976b).

Guinan, E. F., Koch, R. H. & Plavec, M. J., 1984. *Astrophys. J.*, **282**, 667.

Haisch, B. M. & Cassinelli, J. P., 1976. *Astrophys. J.*, **208**, 253.

Harmanec, P. & Kříž, S., 1976. *Be and Shell Stars, IAU Symp. No. 70*, ed. Slettebak, A., p. 385, Reidel, Dordrecht, Holland.

Harmann, W.-R., 1980. *Astr. Astrophys.*, **84**, 342.

Harnden Jr., F. R., Fabricant, D., Topka, K., Flannery, B. P., Tucker, W. H. & Gorenstein, P., 1977. *Astrophys. J.*, **214**, 418.

Henser, G., 1982. *Astr. Astrophys.*, **114**, 309.

Hoffleit, D., 1982. *Bright Star Catalogue*, Yale University Observatory, Conneticut, U.S.A.

Hook, R. & Giddings, J., *S.E.R.C. STARLINK User Note, No. 37*, 1985.

Howarth, I. D. & Murray, J., *S.E.R.C. STARLINK User Note, No. 50*, 1987.

Huang, L., Hsu, J. C. & Guo, Z. H., 1989. *Astr. Astrophys. Suppl.*, **78**, 431.

Huang, S.-S., 1972. *Astrophys. J.*, **171**, 549.

Jones, T. J., 1979. *Astrophys. J.*, **228**, 787.

Kamp, L. W., 1978. *Astrophys. J. Suppl.*, **36**, 143.

Kastner, S. O., 1980. *J. Quant. Spec. Rad. Trans.*, **23**, 327.

Kemp, J. C., Barbour, M. S., McBirney, R. E. & Rudy, R. J., 1981. *Astrophys. J.*, **243**, 557.

Kemp, J. C., Henson, G. D., Kraus, D. J., Beardsley, I. S., Carroll, L. C., Ake, T. B., Simon, T. & Collins II, G. W., 1986. *Astrophys. J.*, **300**, L11.

Koch, R. H., 1960. *Astr. J.*, **65**, 127.

Kondo, Y., McCluskey Jr., G. E. & Harvel, C. A., 1981. *Astrophys. J.*, **247**, 202.

Kondo, Y., McCluskey Jr., G. E. & Stencel, R. E., 1979. *Astrophys. J.*, **233**, 906.

Kopal, Z., 1978. *Dynamics of Close Binary Systems*, p. 414, Volume 68 of *Astrophysics and Space Science Library*, Reidel, Dordrecht, Holland.

Kopal, Z., 1981. *Photometric and Spectroscopic Binary Systems*, p. 535, Reidel, Dordrecht, Holland.

Kopal, Z. & Shapley, H. B., 1956. *Jodrell Bank Ann.*, **1**, 141.

Koubský, P., 1978. *Bull. Astr. Inst. Czech.*, **29**, 288.

Koubský, P., 1989. Private communication.

Koubský, P., Harmanec, P., Horn, J., Jerzykiewicz, M., Kříž, S., Papoušek, J., Pavlovski, K. & Ždárský, F., 1980. *Bull. Astr. Inst. Czech.*, **31**, 75.

Kurucz, R. L., 1979. *Astrophys. J. Suppl.*, **40**, 1.

Lin, D. N. C. & Pringle, J. E., 1976. *Structure and Evolution of Close Binary Systems, IAU Symp. No. 73*, eds. Eggleton, P., Mitton, S. & Whelan, J. J., pp. 237–252, Reidel, Dordrecht, Holland.

Lubow, S. H. & Shu, F. H., 1975. *Astrophys. J.*, **198**, 383. (Paper LS).

Lubow, S. H. & Shu, F. H., 1976. *Astrophys. J.*, **207**, L53.

Lucy, L. B., 1982. *Astrophys. J.*, **255**, 278.

Lynden-Bell, D. & Pringle, J. E., 1974. *Mon. Not. R. astr. Soc.*, **168**, 603.

Marlborough, J. M. & Peters, G. J., 1986. *Astrophys. J. Suppl.*, **62**, 875.

Mendoza, C., 1983. *Planetary Nebulae, IAU Symp. No. 103*, ed. Flower, D. R., p. 143, Reidel, Dordrecht, Holland.

Mermilliod, J.-C., 1982. *Astr. Astrophys.*, **109**, 48.

Miczaika, G. R., 1949. *Astron. Nachr.*, **277**, 167.

Mihalas, D., 1978. *Stellar Atmospheres*, p. 279, W. H. Freeman & Co., San Francisco, U.S.A., 2nd edition. (1978a).

Mihalas, D., 1978. *Stellar Atmospheres*, pp. 310–315, W. H. Freeman & Co., San Francisco, U.S.A., 2nd edition. (1978b).

Mihalas, D., 1978. *Stellar Atmospheres*, p. 314, W. H. Freeman & Co., San Francisco, U.S.A., 2nd edition. (1978c).

Morgan, W. W. & Keenan, P. C., 1973. *Spectral Classification*, p. 29, Volume 11 of *Ann. Rev. Astr. Astrophys.*, Annual Reviews Inc., Palo Alto, California, U.S.A.

McCluskey, G. E. & Kondo, Y., 1981. *Astrophys. J.*, **246**, 464.

McLaughlin, D. B., 1961. *J. R. astr. Soc. Canada*, **55**, 73.

McNamara, D. H. & Feltz, K. A., 1976. *Publs. astr. Soc. Pacif.*, **88**, 688.

Niemela, V. S. & Sahade, J., 1980. *Astrophys. J.*, **238**, 244.

Olson, E. C., 1980. *Astrophys. J.*, **237**, 496.

Olson, G. L., 1982. *Astrophys. J.*, **255**, 267.

Paczyński, B., 1971. *Evolutionary Processes in Close Binary Systems*, p. 183, Volume 9 of *Ann. Rev. Astr. Astrophys.*, Annual Reviews Inc., Palo Alto, California, U.S.A.

Pai, Shih-I, 1962. *Magnetogasdynamics and Plasma Dynamics*, p. 31, Springer Verlag, Wein, Germany.

Parthasarathy, M., Lambert, D. L. & Tomkin, J., 1983. *Mon. Not. R. astr. Soc.*, **203**, 1063.

Percy, J. R., Coffin, B. L., Drukier, G. A., Ford, R. P., Plume, R., Richer, M. G. & Spalding, R., 1988. *Publs. astr. Soc. Pacif.*, **100**, 1555.

Peters, G. J., 1982. *Be Stars, IAU Symp. No. 98*, eds. Jaschek, M. & Groth, H.-G., p. 331, Reidel, Dordrecht, Holland.

Peters, G. J., 1989. *Algols, IAU Coll. No. 107*, ed. Batten, A. H., p. 9, Kluwer Academic Publishers, Dordrecht, The Netherlands.

Peters, G. J. & Polidan, R. S., 1984. *Astrophys. J.*, **283**, 745.

Piirola, V., 1980. *Astr. Astrophys.*, **90**, 48.

Plavec, M. J., 1976. *Be and Shell Stars, IAU Symp. No. 70*, ed. Slettebak, A., p. 439, Reidel, Dordrecht, Holland.

Plavec, M. J., 1983. *Astrophys. J.*, **275**, 251.

Plavec, M. J., 1987. *Physics of Be Stars, IAU Coll. No. 92*, eds. Slettebak, A. & Snow Jr., T. P., p. 451, Cambridge University Press, Cambridge, England.

Prendergast, K. H. & Taam, R. E., 1974. *Astrophys. J.*, **189**, 125. (Paper PT).

Press, W. H., Flannery, B. P., Teukolsky, S. A. & Vettering, W. T., 1988. *Numerical Recipes*, p. 108, Cambridge University Press, Cambridge, England.

Prinja, R. K., 1989. *Mon. Not. R. astr. Soc.*, **241**, 721.

Rees, P. C. T., 1987. Private communication.

Rees, P. C. T., *S.E.R.C. STARLINK User Note, No. 37*, 1987.

Richards, M. T., Mochnacki, S. W. & Bolton, C. T., 1988. *Astr. J.*, **96**, 326.

Różyczka, M., 1988. *Acta. Astr.*, **38**, 175.

Różyczka, M. & Schwarzenberg-Czerny, A., 1986. *Acta. Astr.*, **37**, 141.

Rudy, R. J. & Kemp, J. C., 1976. *Astrophys. J.*, **207**, L125.

Rudy, R. J. & Kemp, J. C., 1978. *Astrophys. J.*, **221**, 200.

Rybicki, G. B. & Hummer, D. G., 1978. *Astrophys. J.*, **219**, 654.

Schull, J. M. & van Steenberg, M., 1982. *Astrophys. J. Suppl.*, **48**, 95.

Schuster, W. J. & Alvarez, M., 1983. *Publs. astr. Soc. Pacif.*, **95**, 35.

Schwarz, H. E. & Clarke, D., 1984. *Astr. Astrophys.*, **132**, 370.

Shakovshoi, N. M., 1965. *Soviet Astr.*, **8**, 833.

Shakura, N. I. & Sunyaev, R. A., 1973. *Astr. Astrophys.*, **24**, 337.

Slettebak, A., 1976. *Be and Shell Stars, IAU Symp. No. 70*, ed. Slettebak, A., p. 123, Reidel, Dordrecht, Holland.

Slettebak, A., 1982. *Astrophys. J. Suppl.*, **50**, 55.

Smith, K. C., 1989. Private communication.

Snow Jr., T. P., Peters, G. J. & Mathieu, R. D., 1979. *Astrophys. J. Suppl.*, **39**, 359.

Sobolev, V. V., 1960. *The Moving Envelopes of Stars*, Harvard University Press, Cambridge, U.S.A. (English translation).

Sørensen, S.-A., Matsuda, T. & Sakurai, T., 1974. *Astrophys. & Space Sci.*, **33**, 465.

Spitzer Jr., L., 1978. *Physical Processes in the Interstellar Medium*, p. 174, Wiley, New York, U.S.A.

Stewart, R. T., Slee, O. B., White, Graeme L., Budding, E., Coates, D. W., Thompson, K. & Bunton, J. D., 1989. *Astrophys. J.*, **342**, 463.

Stickland, D., 1990. Private communication.

Struve, O., 1931. *Astrophys. J.*, **73**, 94.

Struve, O., 1944. *Astrophys. J.*, **99**, 222.

Svechnikov, A. M., 1973. *Perem, Zvezdy*, **18**, 525.

Tassoul, J.-L. & Tassoul, M., 1973. *Astrophys. J.*, **359**, 155.

Taylor, A. R., Waters, L. B. F. M., Bjorkman, K. S. & Dougherty, S. M., 1990. *Astr. Astrophys.*, **231**, 453.

Tinbergren, J., 1982. *Astr. Astrophys.*, **105**, 53.

Ulrich, R. K. & Burger, H. L., 1976. *Astrophys. J.*, **206**, 509.

Warner, B. & Peters, W., 1972. *Mon. Not. R. astr. Soc.*, **160**, 15.

Waters, L. B. F. M., Coté, J. & Lamers, H. J. G. L. M., 1987. *Astr. Astrophys.*, **185**, 206.

White, N. E., Culhane, J. L., Parmer, A. N., Kellett, B. J., Kahn, S., van den Oord, G. H. J. & Kuijpers, J., 1988. *Astrophys. J.*, **301**, 262.

Zahn, J. P., 1966. *Astr. Astrophys.*, **29**, 565.

Appendix A

IUE spectra

A.1 Introduction

This appendix contains the processed *IUE* spectral regions covering the wavelengths where the resonance lines of the N^{+4}, C^{+3}, Si^{+3}, and Al^{+2} ions are located. The contribution of the photosphere has been divided out (see section 2.4) leaving line profiles due to the circumstellar material alone. Note that the continuum is quite flat away from the lines (particularly for N^{+4}) demonstrating the quality of the photospheric division. The spectra are listed in phase order where the phase has been derived from Koubský's 1980 ephemeris (see page 34). The spectra have been rectified so that the continuum level, I_c, is set at unity, the small vertical tick-marks represent $0.1\,I_c$, and the rest-wavelengths of the doublets (listed in table 2.1) are marked at the top of each figure by two vertical lines.

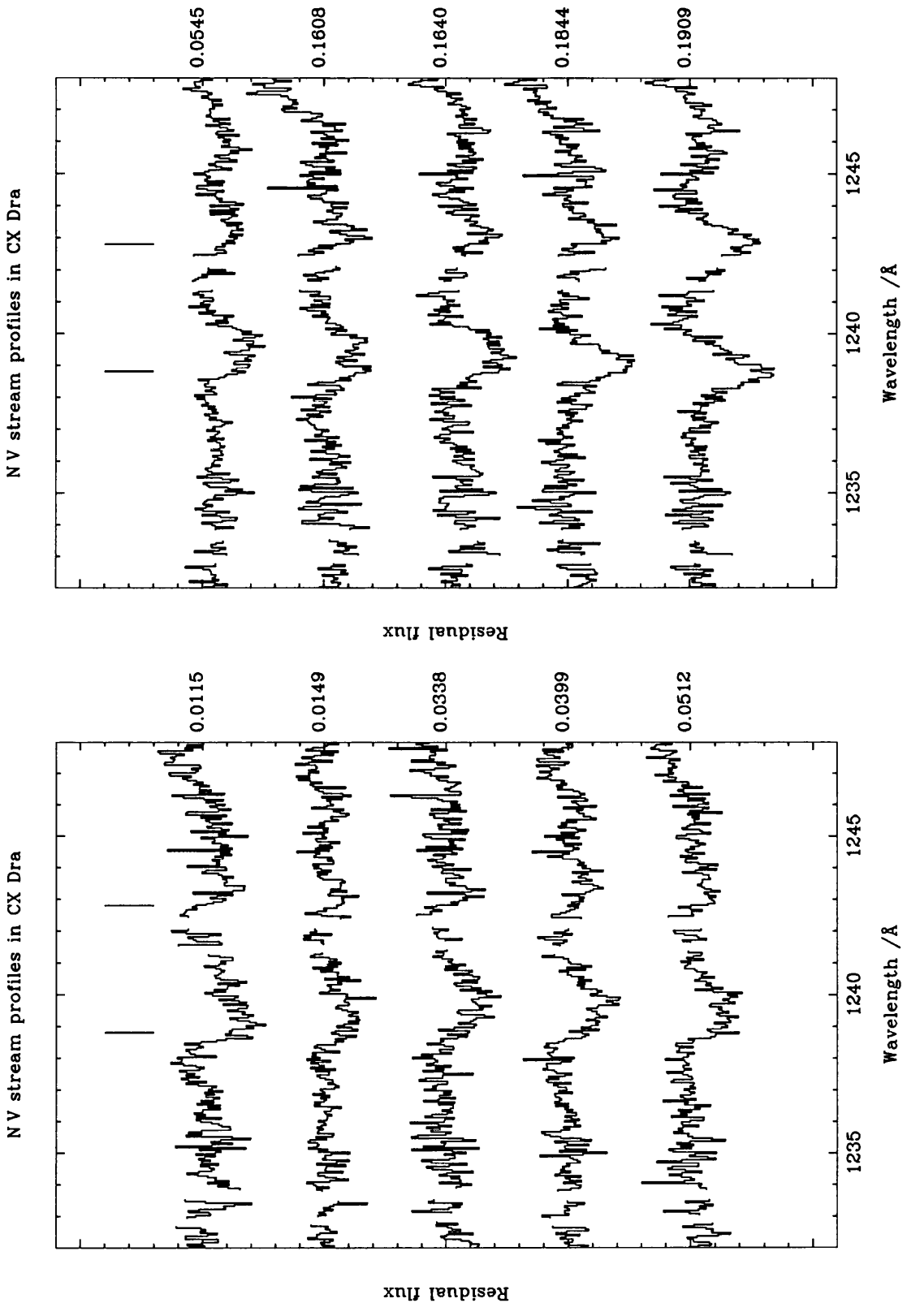

Figure A.1: *The N V spectral region.*

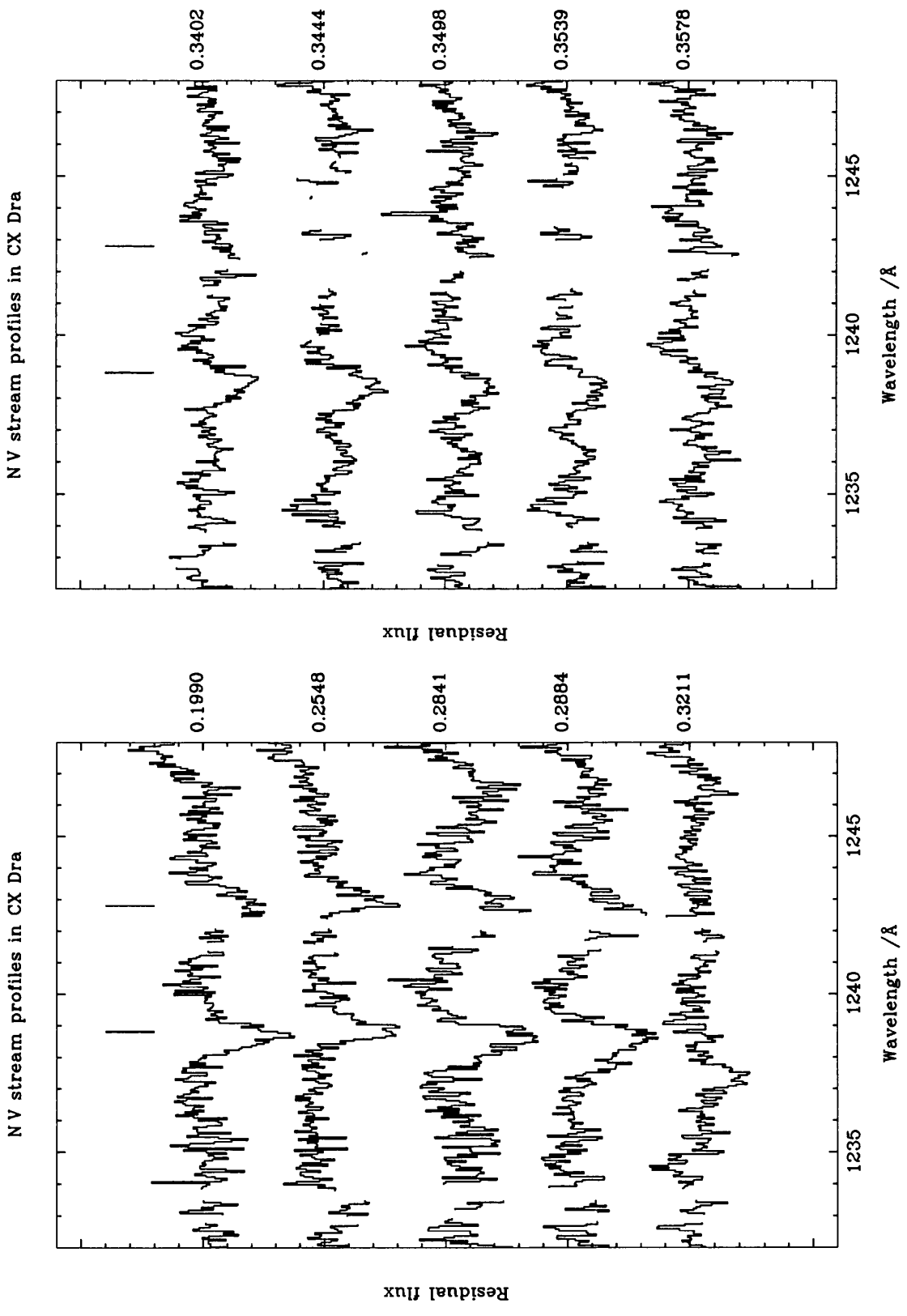
N V stream profiles in CX Dra
0.1990
0.2548
0.2841
0.2884
0.3211
Residual flux
1235
1240
1245
Wavelength /Å
N V stream profiles in CX Dra
0.3402
0.3444
0.3498
0.3539
0.3578
Residual flux
1235
1240
1245
Wavelength /Å

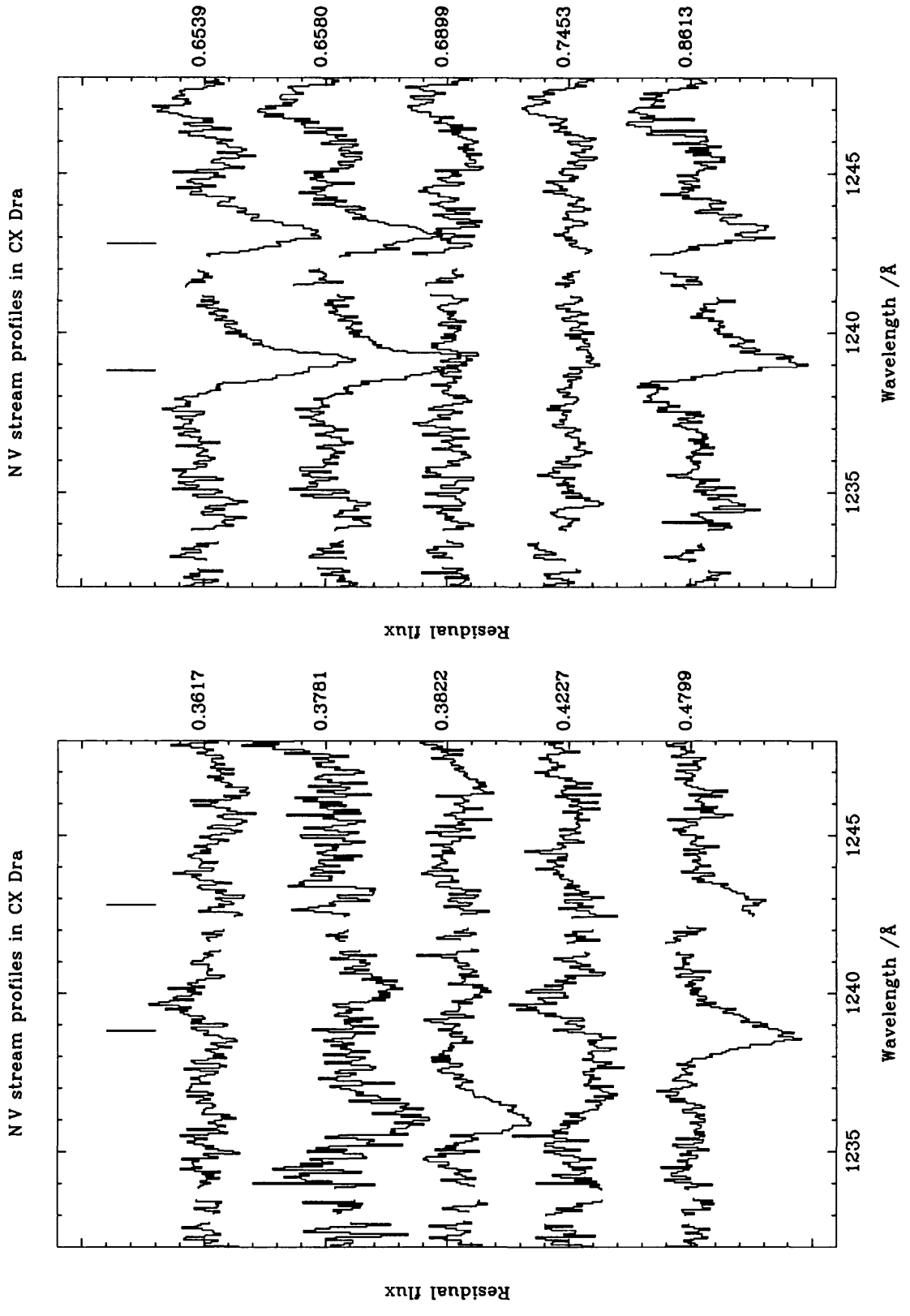
N V stream profiles in CX Dra
0.3617
0.3781
0.3822
0.4227
0.4799
Residual flux
1235
1240
1245
Wavelength /Å
N V stream profiles in CX Dra
0.6539
0.6580
0.6889
0.7453
0.8613
Residual flux
1235
1240
1245
Wavelength /Å

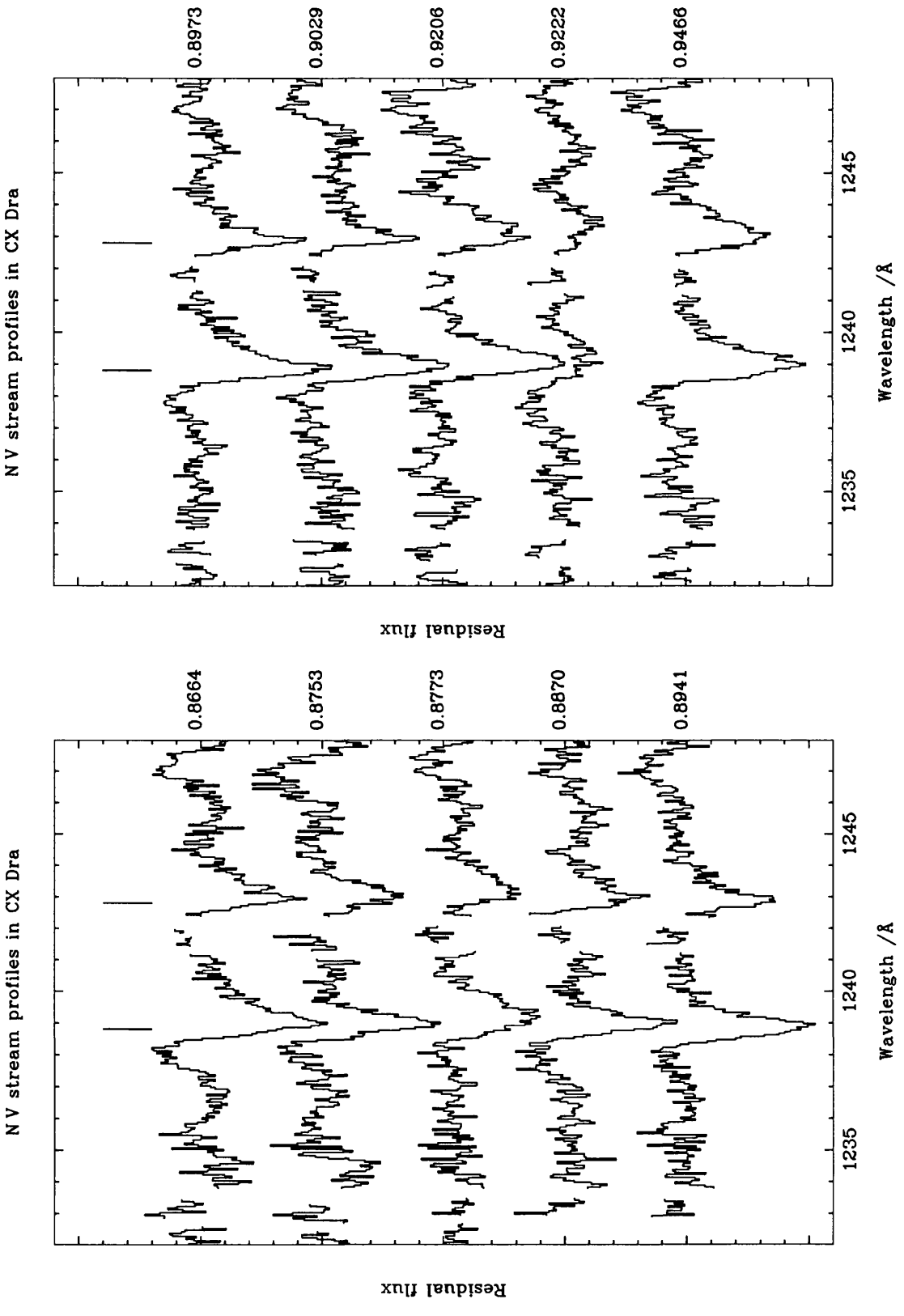
N V stream profiles in CX Dra
0.8664
0.8753
0.8773
0.8870
0.8941
Residual flux
1235
1240
1245
Wavelength /Å
N V stream profiles in CX Dra
0.8973
0.9029
0.9206
0.9222
0.9466
Residual flux
1235
1240
1245
Wavelength /Å

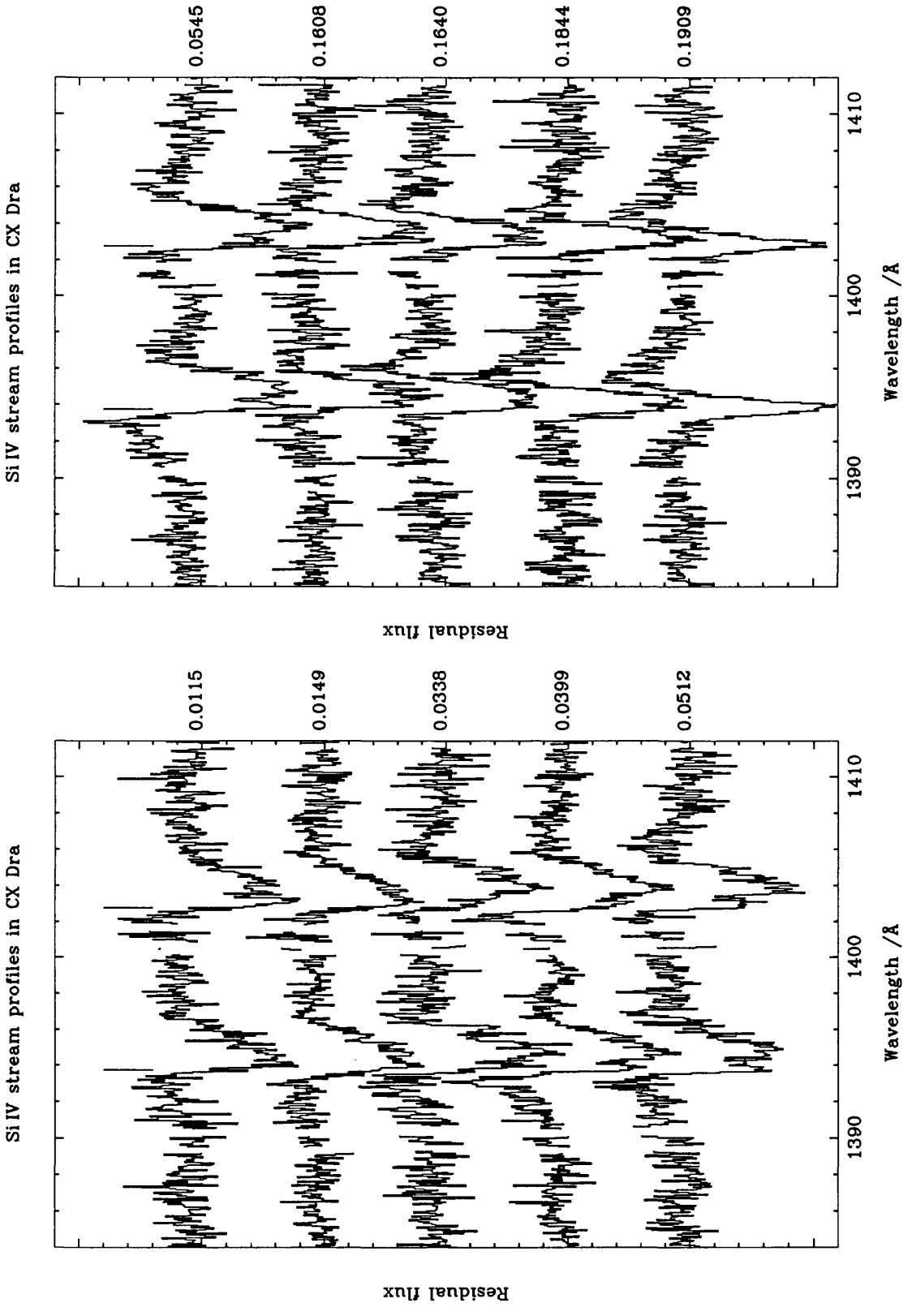

Figure A.2: *The Si IV spectral region.*

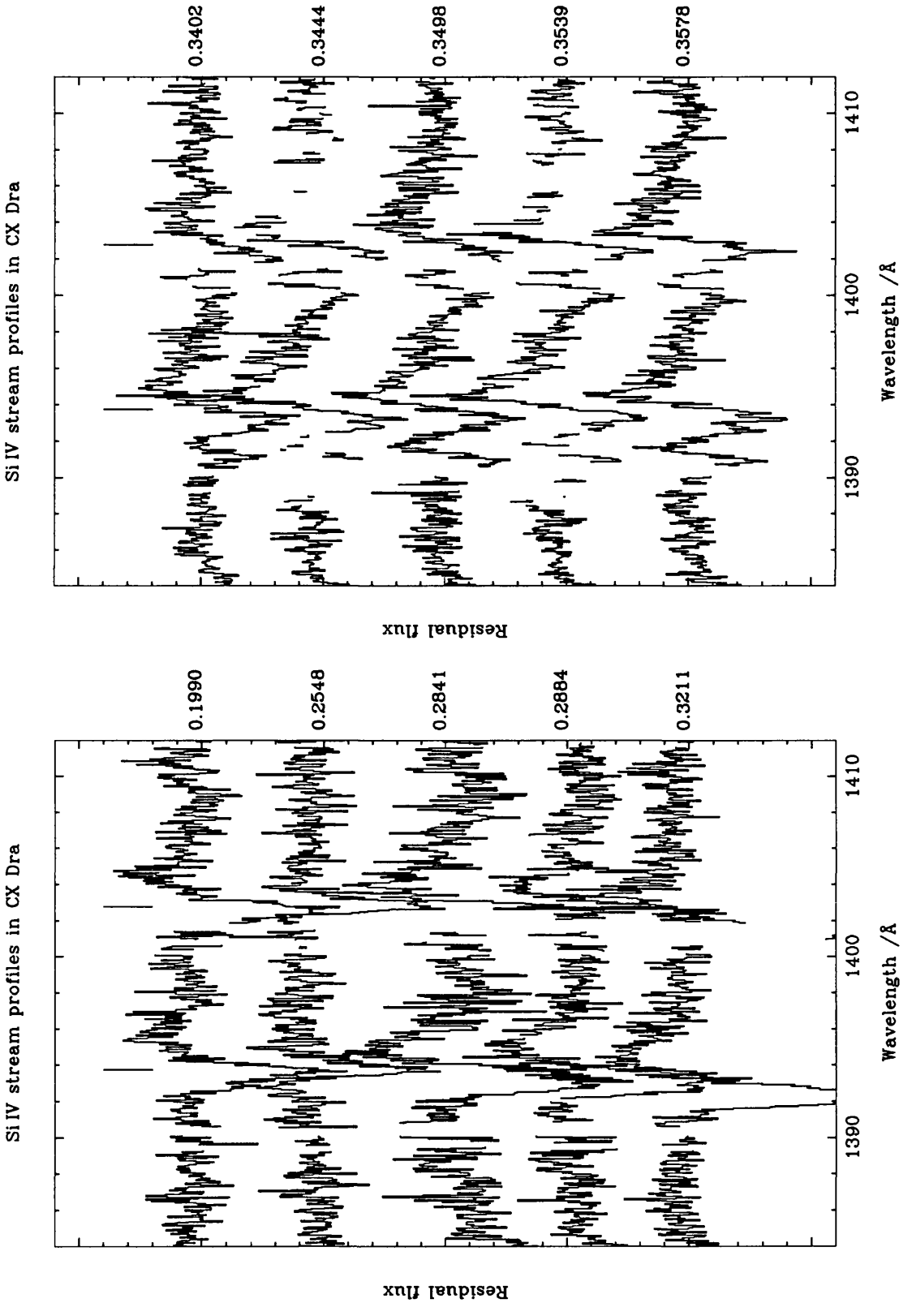
Si IV stream profiles in CX Dra
0.1990
0.2548
0.2841
0.2884
0.3211
Residual Flux
1390
1400
1410
Wavelength /Å
Si IV stream profiles in CX Dra
0.3402
0.3444
0.3498
0.3539
0.3578
Residual Flux
1390
1400
1410
Wavelength /Å

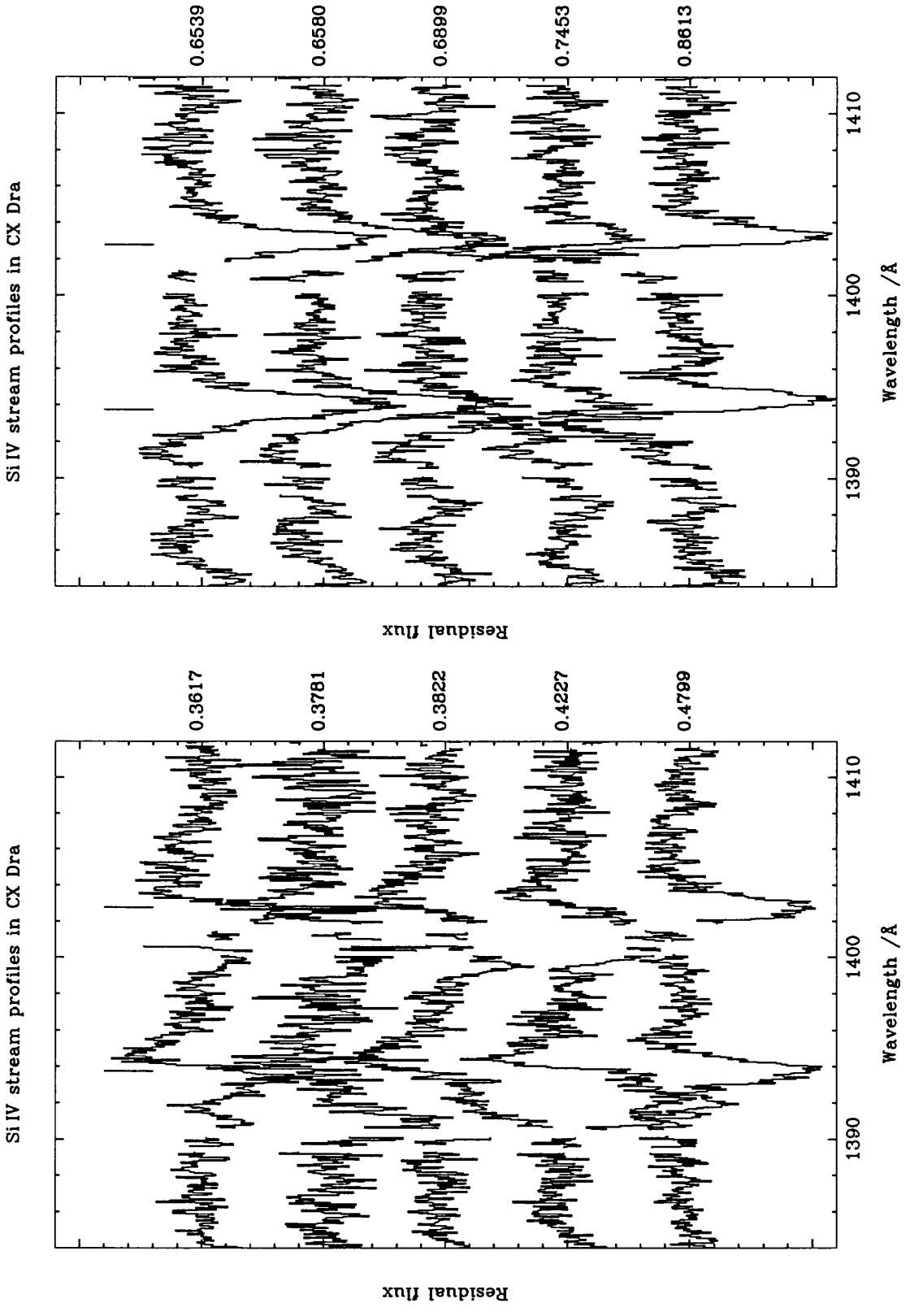
Si IV stream profiles in CX Dra
0.6539
0.6580
0.6899
0.7453
0.8613
Residual Flux
1390
1400
1410
Wavelength /Å
Si IV stream profiles in CX Dra
0.3617
0.3781
0.3822
0.4227
0.4799
Residual Flux
1390
1400
1410
Wavelength /Å

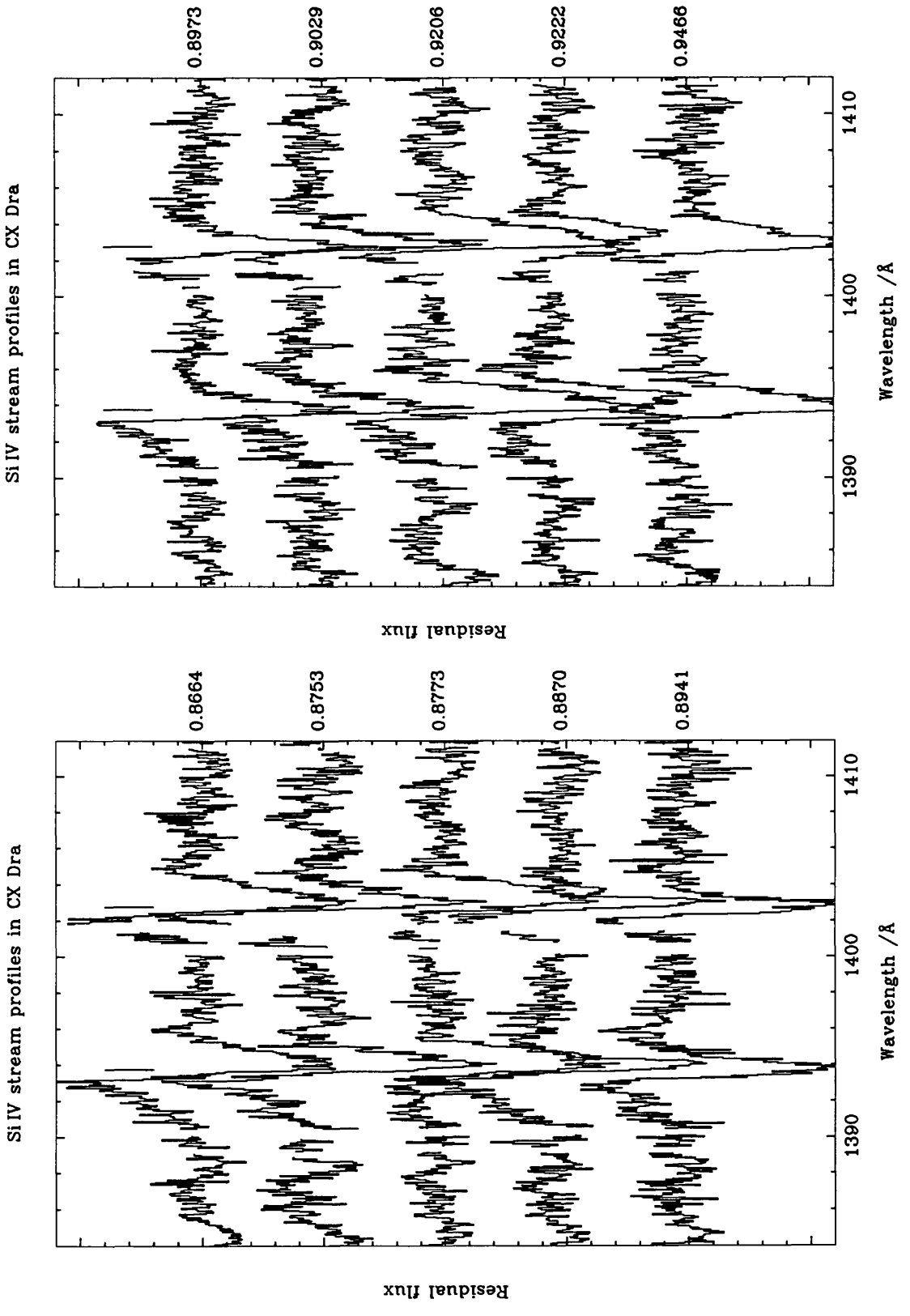
Si IV stream profiles in CX Dra
0.8664
0.8753
0.8773
0.8870
0.8941
Residual flux
1390
1400
1410
Wavelength /Å
Si IV stream profiles in CX Dra
0.8973
0.9029
0.9206
0.9222
0.9466
Residual flux
1390
1400
1410
Wavelength /Å

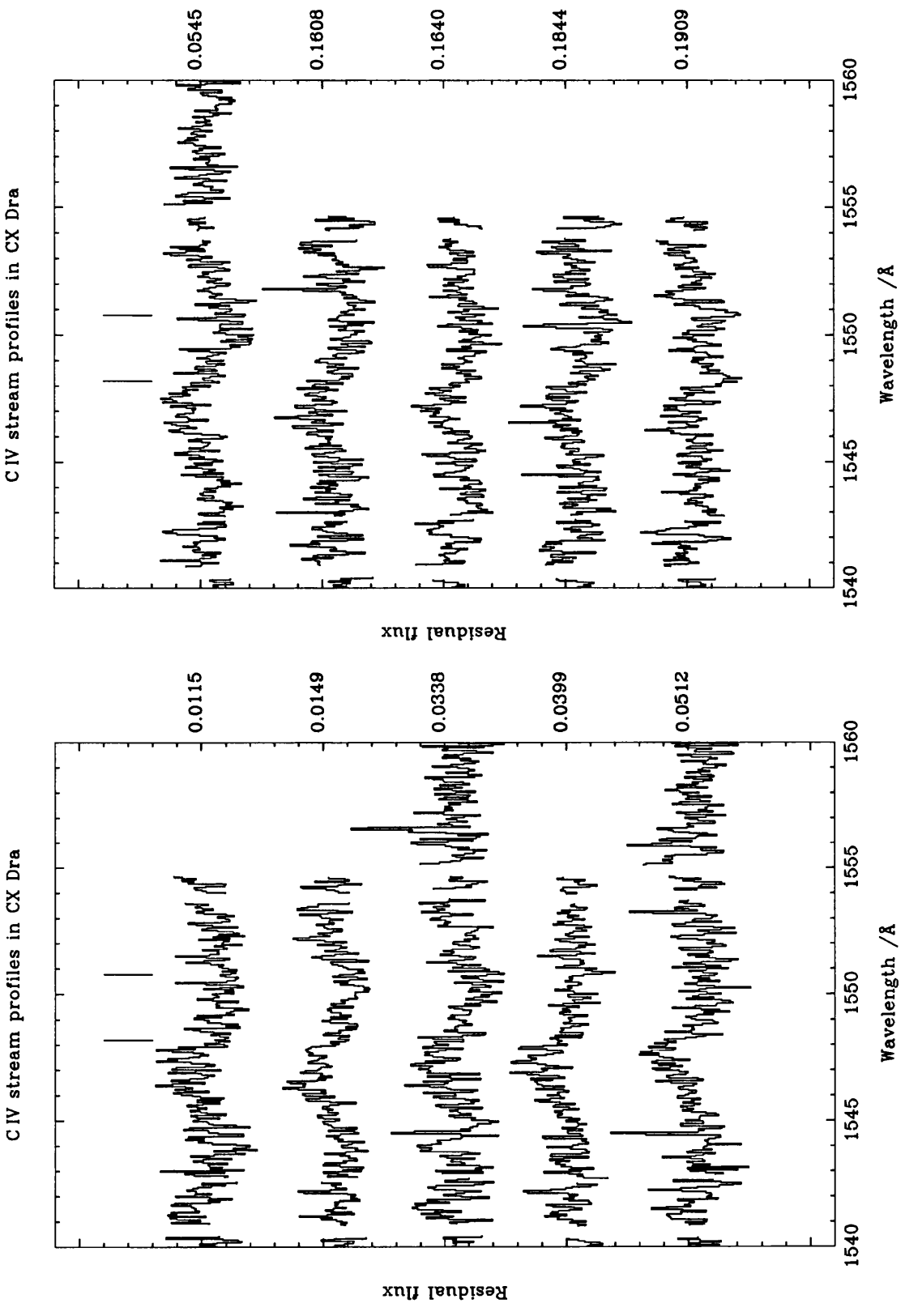

Figure A.3: *The C IV spectral region.*

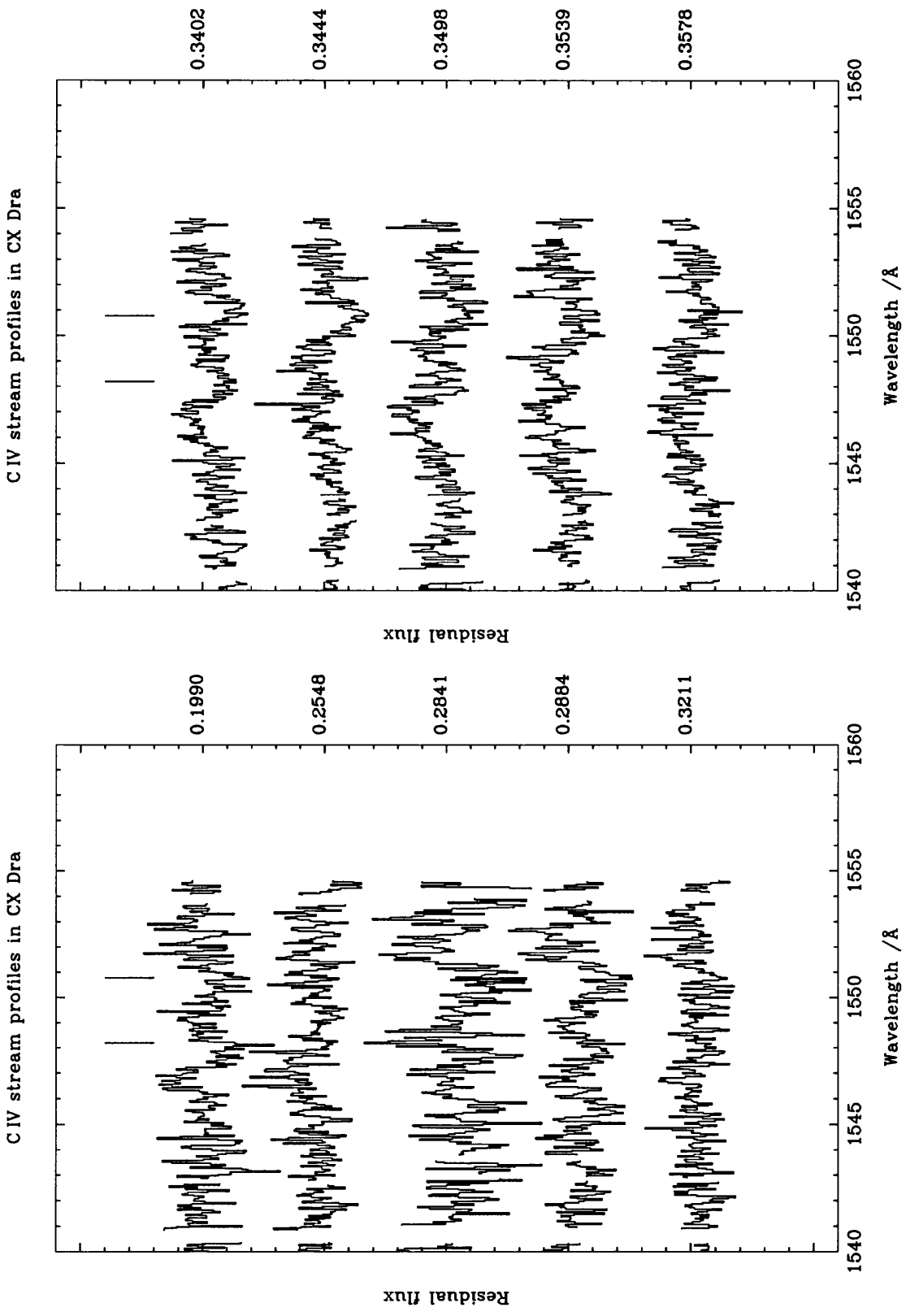
C IV stream profiles in CX Dra
0.1990
0.2548
0.2841
0.2884
0.3211
Residual flux
1540
1545
1550
1555
1560
Wavelength /Å
C IV stream profiles in CX Dra
0.3402
0.3444
0.3498
0.3539
0.3578
Residual flux
1540
1545
1550
1555
1560
Wavelength /Å

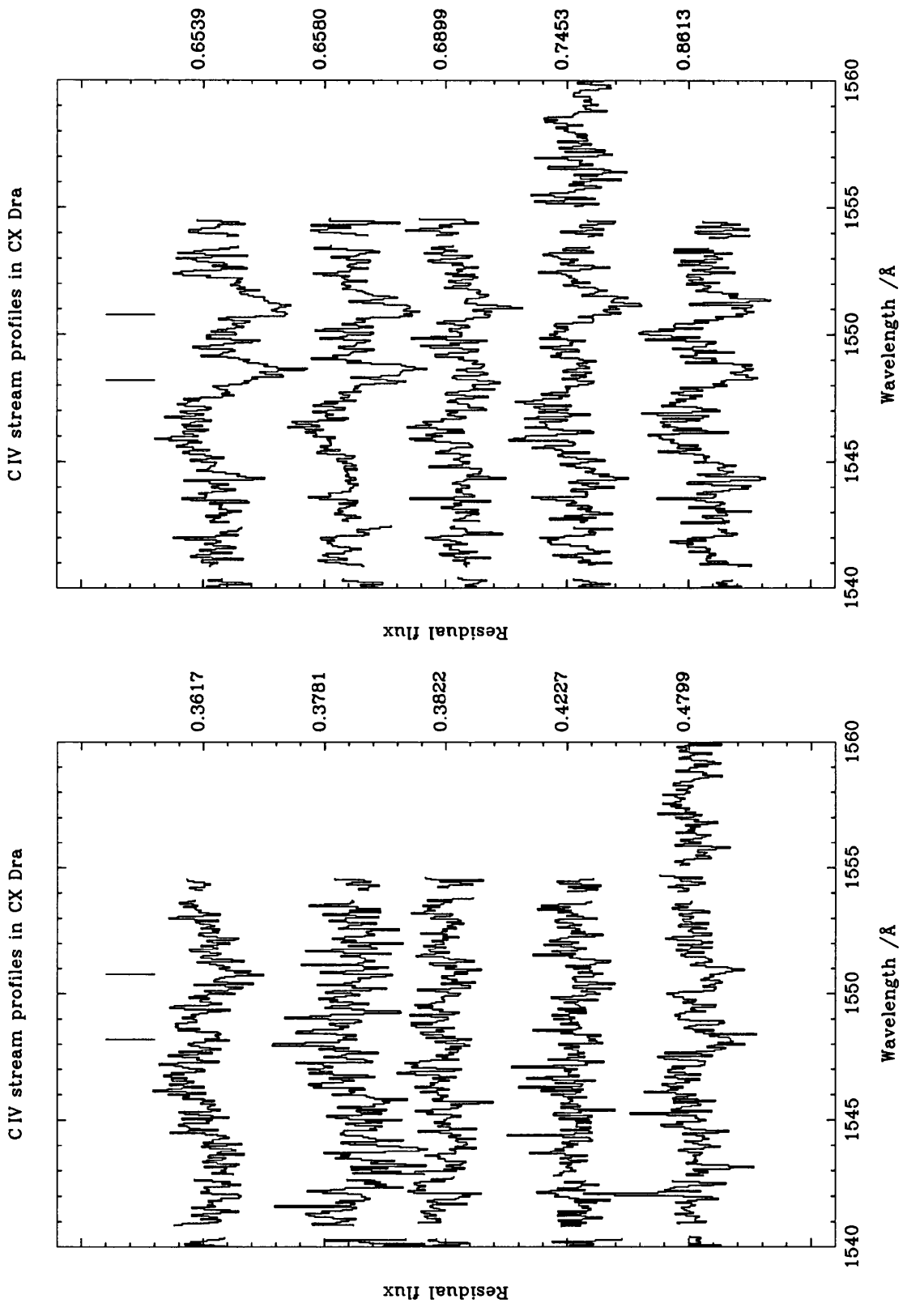
C IV stream profiles in CX Dra
0.6539
0.6580
0.6899
0.7453
0.8613
Residual flux
1540
1545
1550
1555
1560
Wavelength /Å
C IV stream profiles in CX Dra
0.3617
0.3781
0.3822
0.4227
0.4799
Residual flux
1540
1545
1550
1555
1560
Wavelength /Å

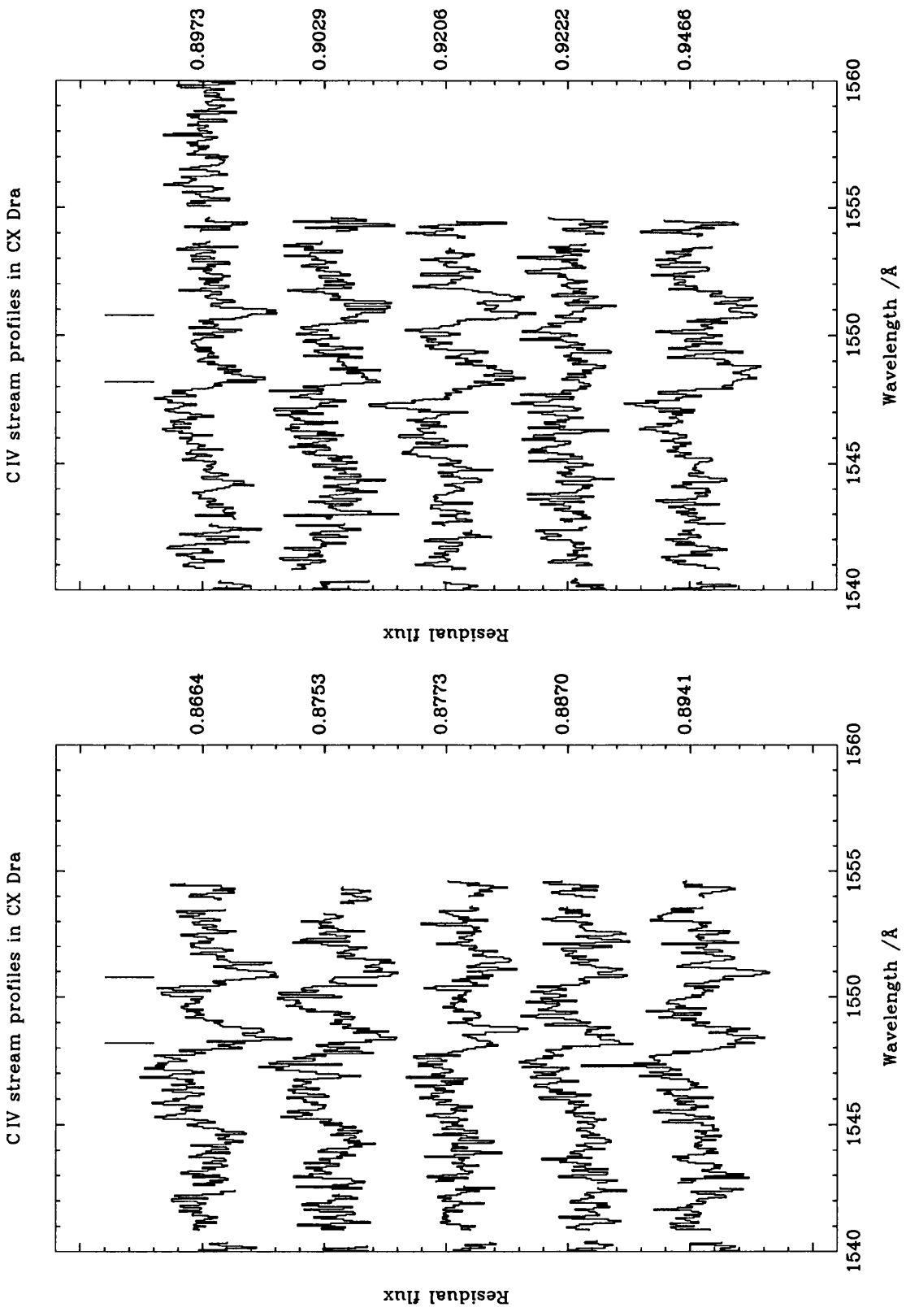
C IV stream profiles in CX Dra
0.8664
0.8753
0.8773
0.8870
0.8941
Residual flux
1540
1545
1550
1555
1560
Wavelength /Å
C IV stream profiles in CX Dra
0.8973
0.9029
0.9206
0.9222
0.9466
Residual flux
1540
1545
1550
1555
1560
Wavelength /Å

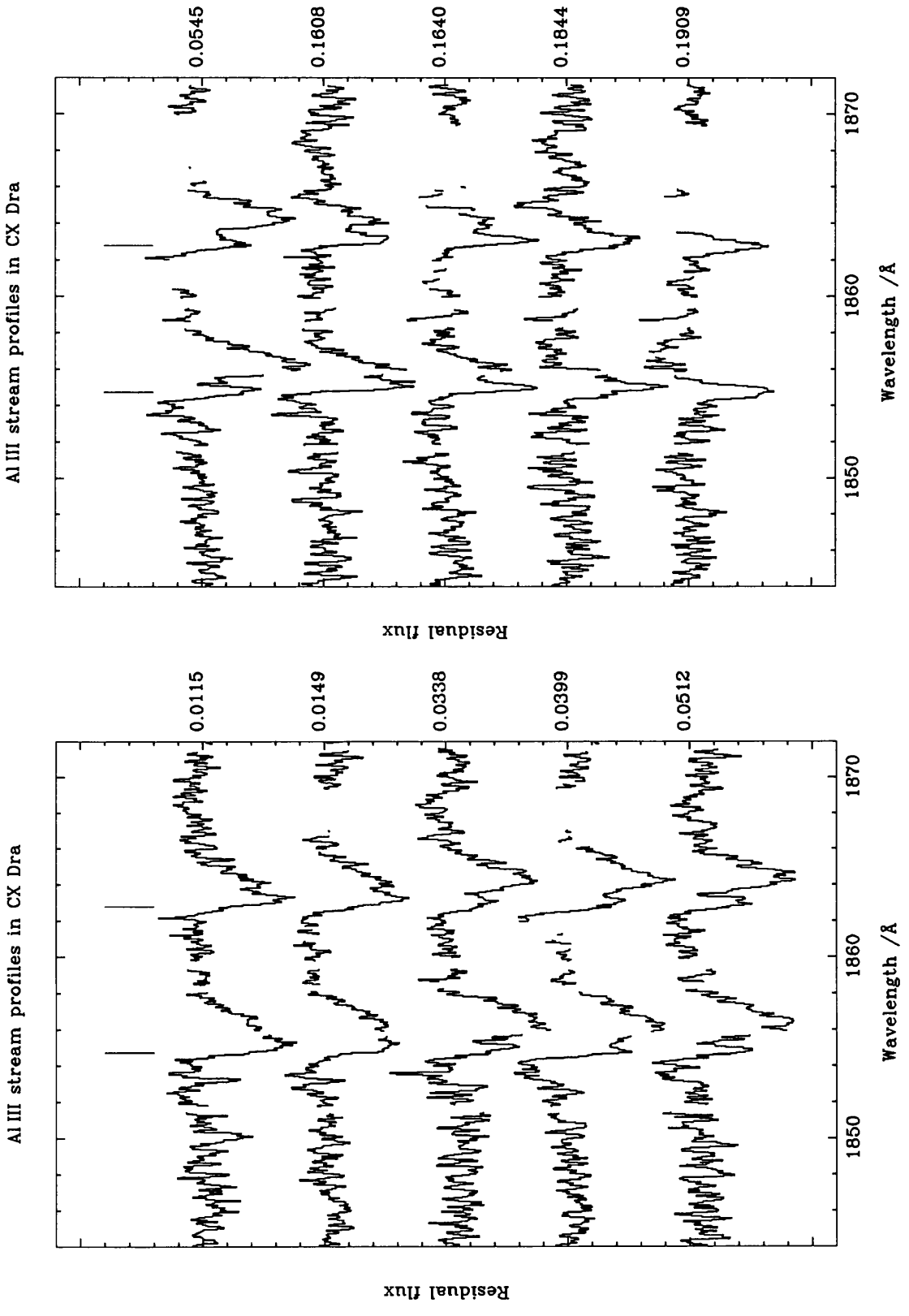

Figure A.4: *The AlIII spectral region.*

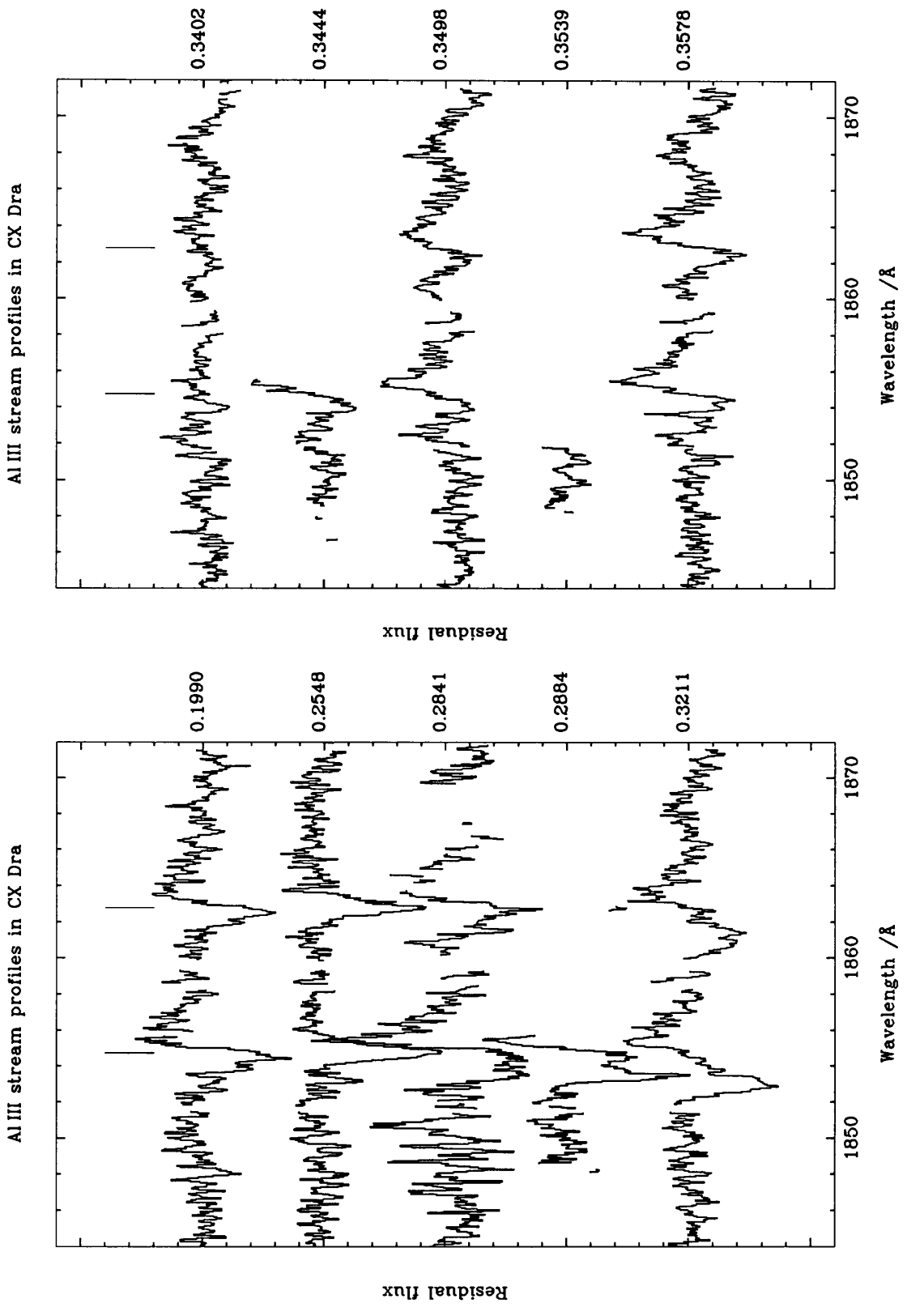
Al III stream profiles in CX Dra
0.1990
0.2548
0.2841
0.2884
0.3211
Residual flux
1850
1860
1870
Wavelength /Å
Al III stream profiles in CX Dra
0.3402
0.3444
0.3498
0.3539
0.3578
Residual flux
1850
1860
1870
Wavelength /Å

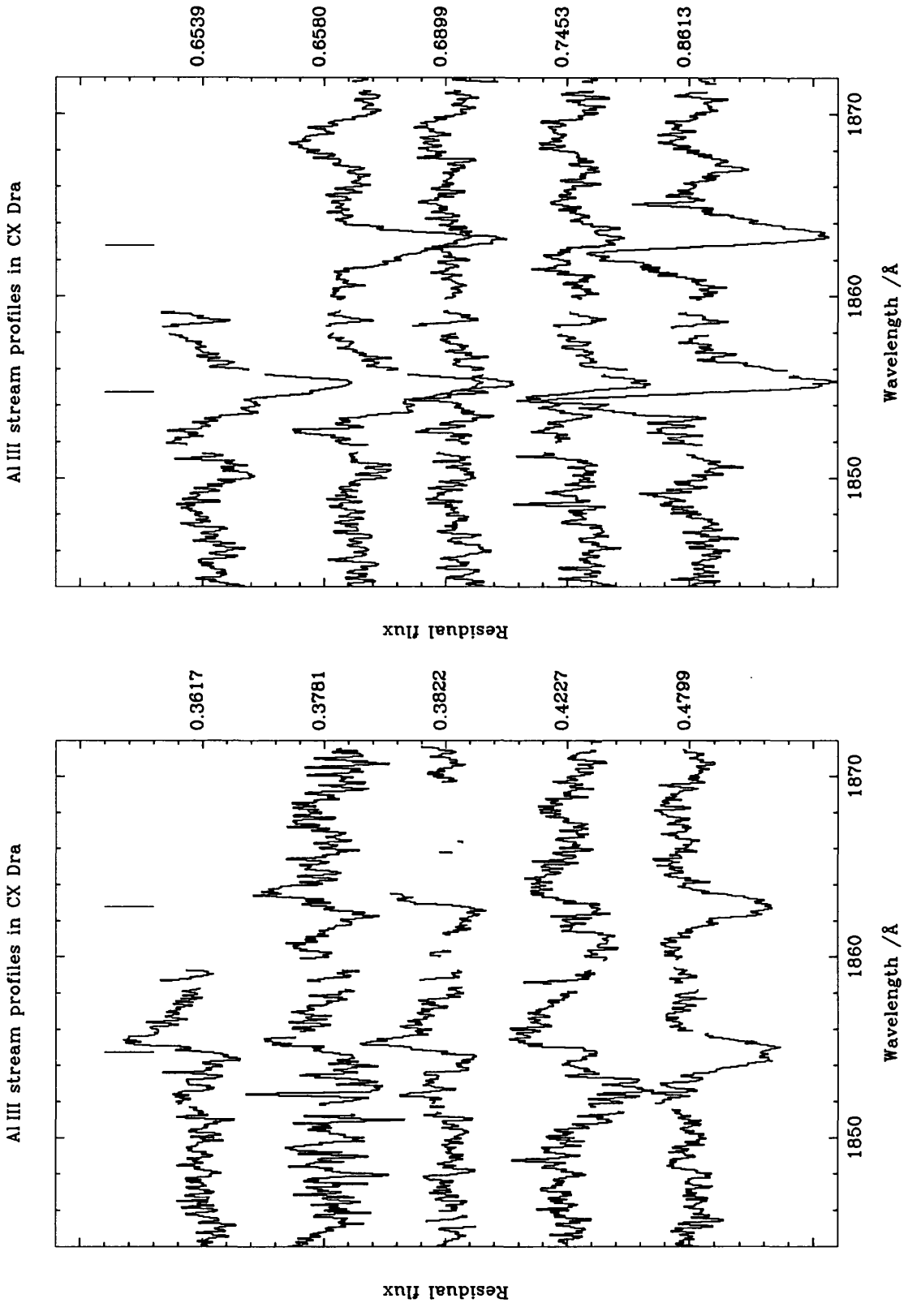
Al III stream profiles in CX Dra
0.6539
0.6580
0.6899
0.7453
0.8613
Residual flux
1850
1860
1870
Wavelength /Å
Al III stream profiles in CX Dra
0.3617
0.3781
0.3822
0.4227
0.4799
Residual flux
1850
1860
1870
Wavelength /Å

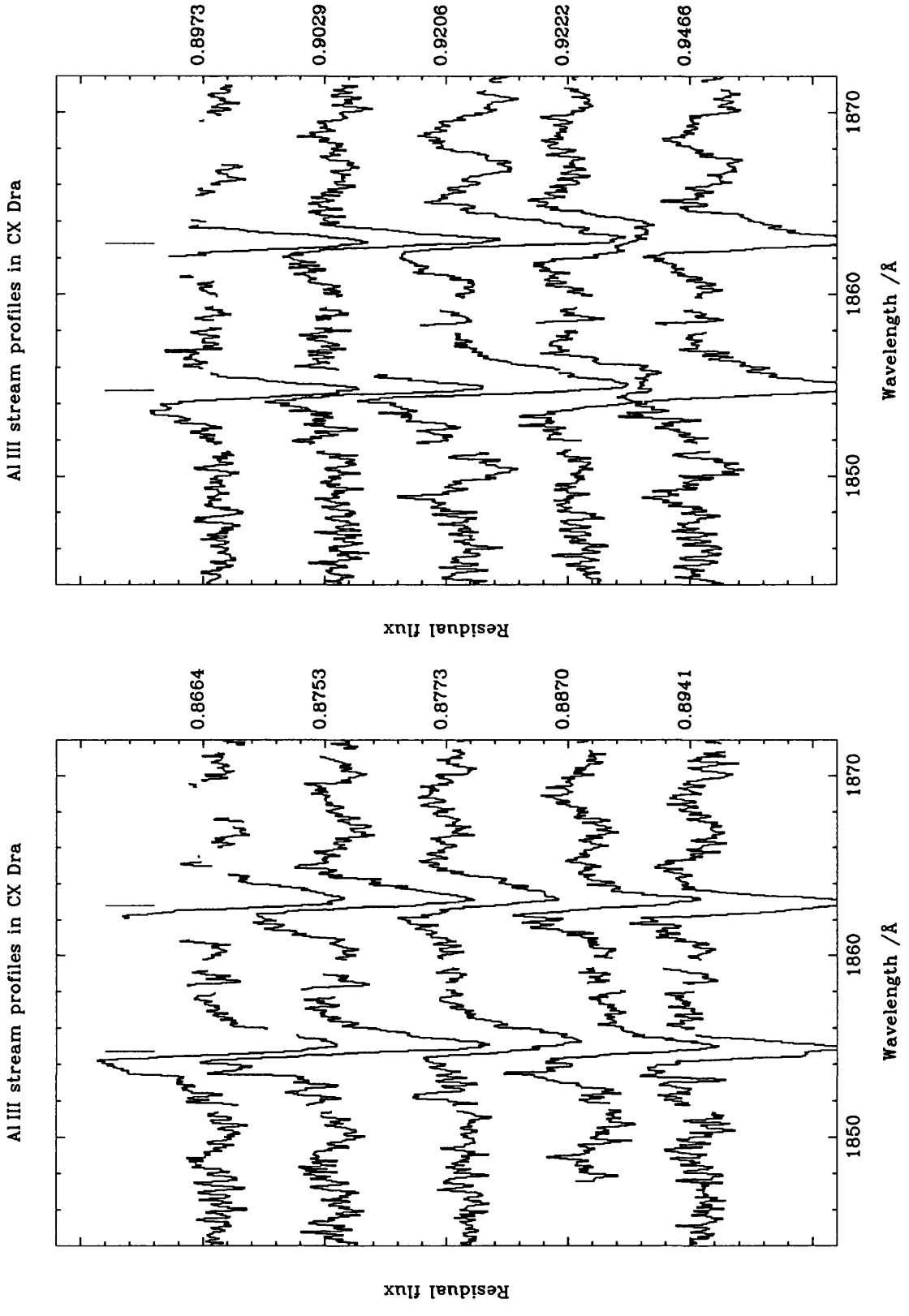
Al III stream profiles in CX Dra
0.8664
0.8753
0.8773
0.8870
0.8941
Residual flux
1850
1860
1870
Wavelength /Å
Al III stream profiles in CX Dra
0.8973
0.9029
0.9206
0.9222
0.9466
Residual flux
1850
1860
1870
Wavelength /Å

Appendix B

Journal of observations

B.1 Introduction

This appendix contains the journal of observations extracted from the World Data Centre archive. All images were taken with the Short-Wavelength Prime (SWP) camera in high-dispersion mode (HIRES) through the large aperture of the *IUE* spacecraft. The phases are derived from Koubský's 1980 ephemeris.

SWP number	HJD − 2440000	Phase	Exposure time /s
8599	4328.9544	0.4799	434
8634	4331.9126	0.9222	420
9981	4484.1281	0.6539	329
9982	4484.1558	0.6580	300
9993	4485.9142	0.9206	300
9996	4486.0885	0.9466	300
10068	4492.3853	0.8870	300
10242	4511.1538	0.6899	300
14703	4826.2381	0.7453	300
19930	5463.2444	0.8773	350
20430	5526.0365	0.2548	310
20727	5567.0385	0.3781	300
20728	5567.0662	0.3822	600
20757	5570.2740	0.8613	300
20758	5570.3081	0.8664	600
20761	5570.4935	0.8941	300
20762	5570.5150	0.8973	600
20763	5570.5525	0.9029	300
20774	5571.2796	0.0115	300
20775	5571.3025	0.0149	600
20777	5571.4289	0.0338	300
20778	5571.4699	0.0399	600
20780	5571.5456	0.0512	300
20781	5571.5678	0.0545	600
20794	5572.2797	0.1608	300

(Continued overleaf)

SWP number	HJD − 2440000	Phase	Exposure time /s
20795	5572.3012	0.1640	600
20797	5572.4373	0.1844	300
20798	5572.4811	0.1909	600
20800	5572.5352	0.1990	300
20808	5573.1054	0.2841	330
20809	5573.1339	0.2884	570
20847	5577.0639	0.8753	310
21486	5647.6896	0.4227	350
28912	6658.2373	0.3402	480
28913	6658.2658	0.3444	900
28914	6658.3019	0.3498	460
28915	6658.3290	0.3539	900
28916	6658.3554	0.3578	420
28917	6658.3818	0.3617	420
29499	6725.0702	0.3211	480

Table B.1: *Journal of IUE observations.*

Addendum I

The PT model: an investigation

Felix qui potuit rerum cognoscere causas.

Virgil — Georgies, II. 490 (70–19 B.C.*)*

I.1 Introduction

A number of points which are in need of clarification have been identified concerning the material of chapter 4. They are listed below.

1. There is an obvious lack of any test of the conservation of both angular momentum and energy in the PT models.

2. The point at which the returning stream reconnects with the stream from the L1 point has no apparent shock as *would* be expected to occur between two jets of supersonic material colliding obliquely. This is suggestive of the presence of some dissipative mechanism (possibly numerical in origin) which should not be operating. The possibility that energy is being exchanged between the

kinetic energy in the mass-motions of the gas and the thermal pool should be investigated.

3. The width of the stream, particularly near the Lagrangian point, seems overly large. Simple models notionally indicate that the width should be of the order of the product of the sound speed and the free-fall time (typically $0.04\,a\Omega$ and $1.0\,\Omega^{-1}$ respectively), i.e. $0.04\,a$ or 2–3 grid cells. These back-of-the-envelope values are in good agreement with the analysis of Lubow and Shu (1976, table 3). Inspection of figures 4.1 and 4.4 reveals that the model streams are approximately twice as wide as this. The most likely explanation is that the PT models have supersonic values for the viscosity, or in the notation of Shakura and Sunyayev (1973), $\alpha \gg 1$. Is this the case?

I.2 Investigation

I.2.1 Conservation of energy and angular momentum

Tests on the conservation of energy and angular momentum were made for two cases: when only one particle is present in the grid and when the mass-flow is represented by many particles. The first case tests the model in the limit of ballistic streaming.

The single-particle models are run in comparison with the ballistic calculations from chapter 3. Figures I.1 and I.2 show the values of the angular momentum and of the Jacobian energy as functions of time for models of U Cep (using the parameters of section 4.3 and $\Delta t = 0.02$). The rapid rise in the value of the angular momentum as the particle approaches the primary is due to the absorption by the particle of orbital angular momentum from the system.

It is readily apparent that, in the single particle case, neither the angular momentum nor the Jacobian are strictly conserved as there are significant differences between the two models, although the Jacobian fares better than the angular momentum. One reason for this might be that the assumption that the force on a particle is constant over a timestep does not accurately reproduce the correct tra-

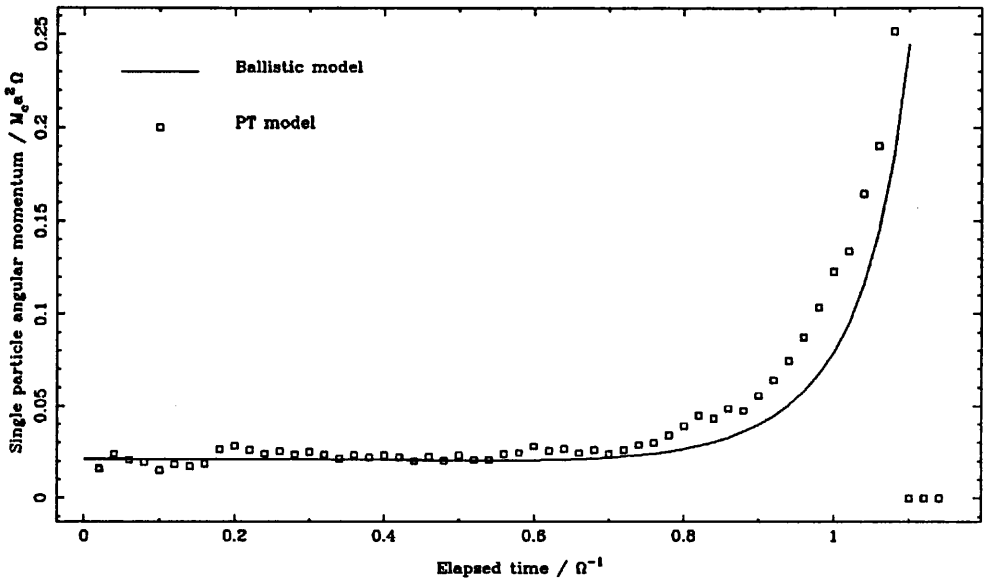

Figure I.1: *Comparison of the angular momentum of a single particle under the PT and ballistic models.*

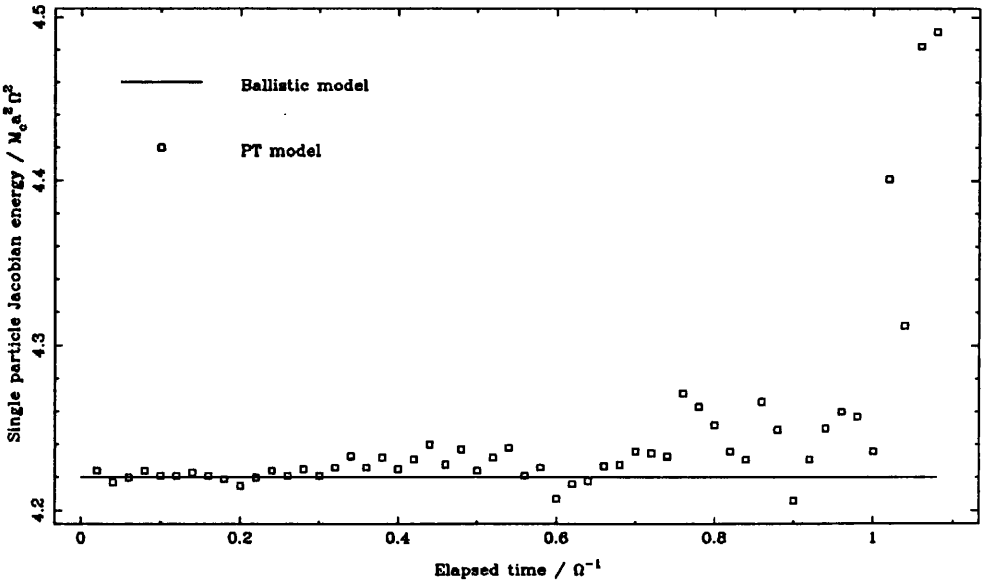

Figure I.2: *Comparison of the Jacobian energy of a single particle under the PT and ballistic models.*

jectory. It is likely that the particle would finish the timestep displaced *outwards* from the primary (as the trajectory is concave *inwards*), thus increasing its angular momentum.

Figures I.3 and I.4, however, compare the true trajectory and the 'constant-force' trajectory for U Cep and CX Dra respectively. The excellent agreement between the two model curves demonstrates that this mechanism cannot be responsible for the non-conservation. Although the error *is* cumulative, it does not grow sufficiently large to disturb the trajectory significantly.

More revealing are figures I.5 and I.6 which show the deviations of the PT model as fractions of the ballistic model. The important point is that whilst the angular momentum deviates by up to 60 %, the Jacobian energy is conserved to an accuracy of 6 %. If errors in the computation of the particle *velocities* were responsible, the energy (dependent on the square of the velocity) might reasonably be expected to deviate more strongly than the angular momentum (which only depends on the velocity in a linear sense). There is an implication in these results that it is the positions of the particles that are being wrongly calculated.

Consider that as the particle trajectories are approximated by a straight line (the constant force assumption), and the stream is generally concave towards the primary, at the end of each timestep it is probable that the particles will be slightly displaced outwards. This implies that the probability distribution for the next generation of particles is shifted outwards too. This is important: it is because the probability distribution becomes displaced that the stream gains angular momentum. The individual calculations themselves may be quite accurate, but because the subsequent generation of particles is produced from a distorted random distribution, shifts of this kind become magnified. The Jacobian energy is generally dominated by the kinetic energy which involves no spatial dependence, thus it is largely immune to these effects (except when the potential energy contribution becomes large near the primary).

To test this, a 'distorted' ballistic model was run which displaced the particle by

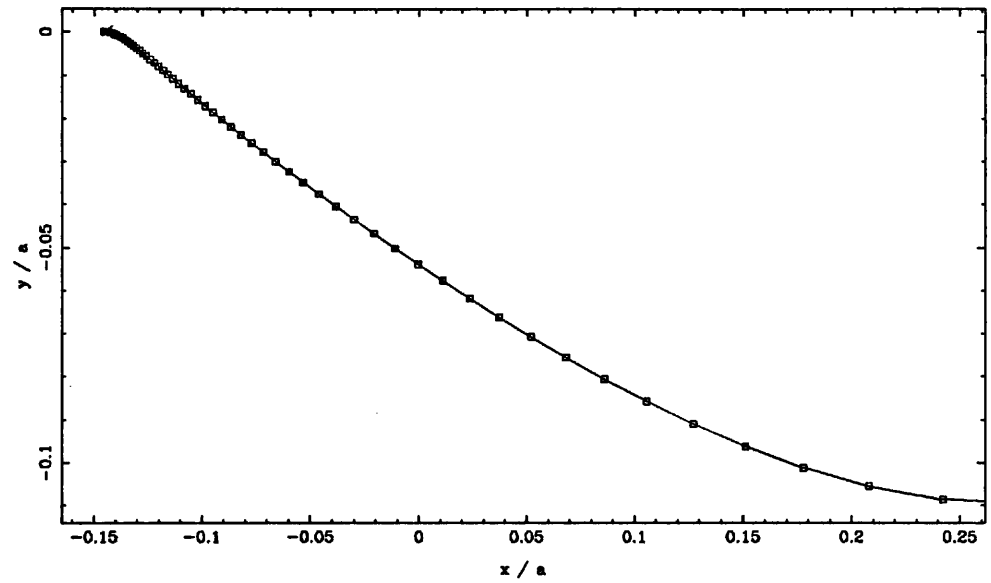

Figure I.3: *Comparison of the trajectory of a single particle computed 'exactly' (□) and the vectors* $\Delta\mathbf{r}$*, calculated under the 'constant-force' assumption for U Cep.*

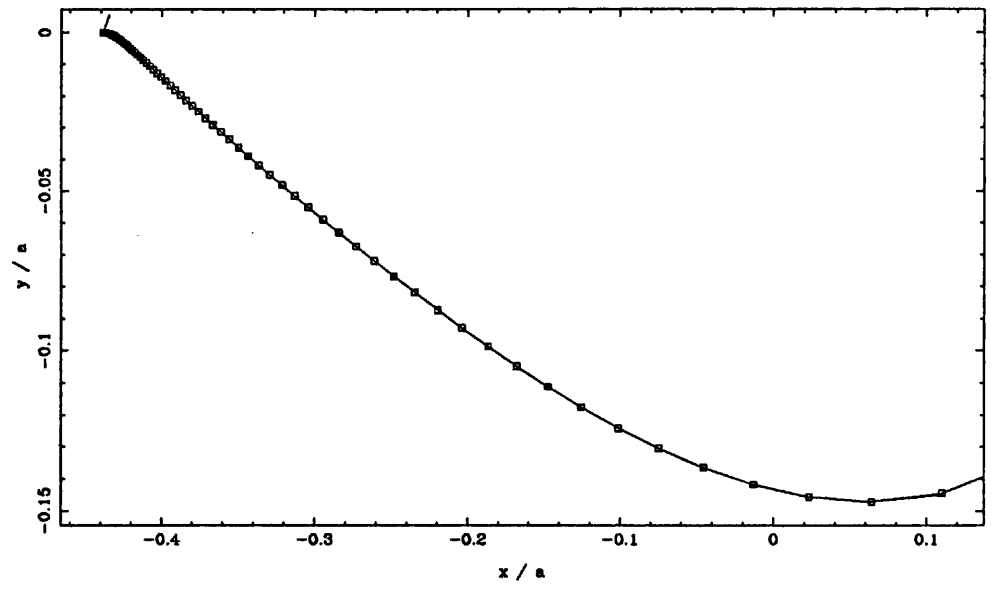

Figure I.4: *Comparison of the trajectory of a single particle computed 'exactly' (□) and the vectors* $\Delta\mathbf{r}$*, calculated under the 'constant-force' assumption for CX Dra.*

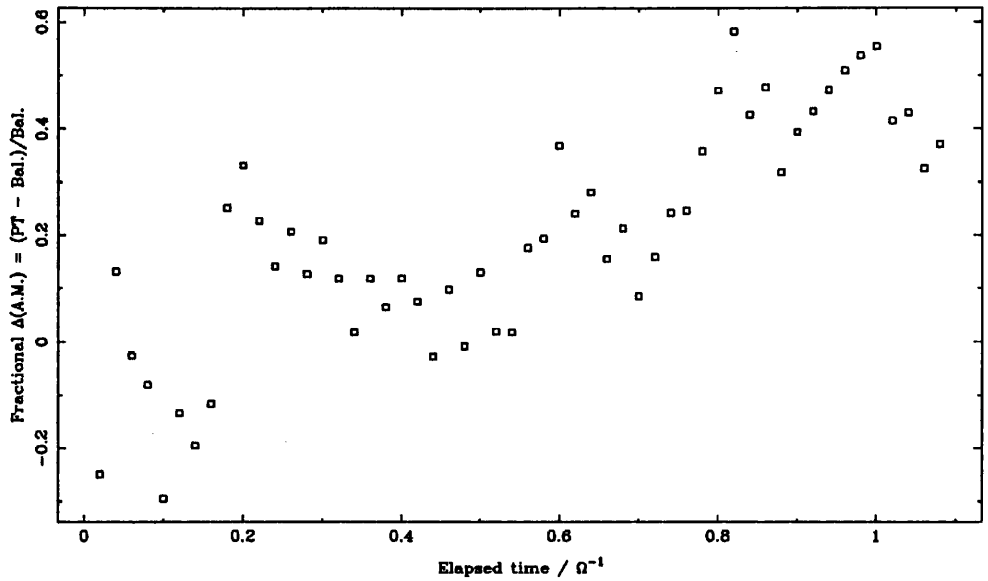

Figure I.5: *Fractional differences between the angular momentum calculations shown in figure I.1.*

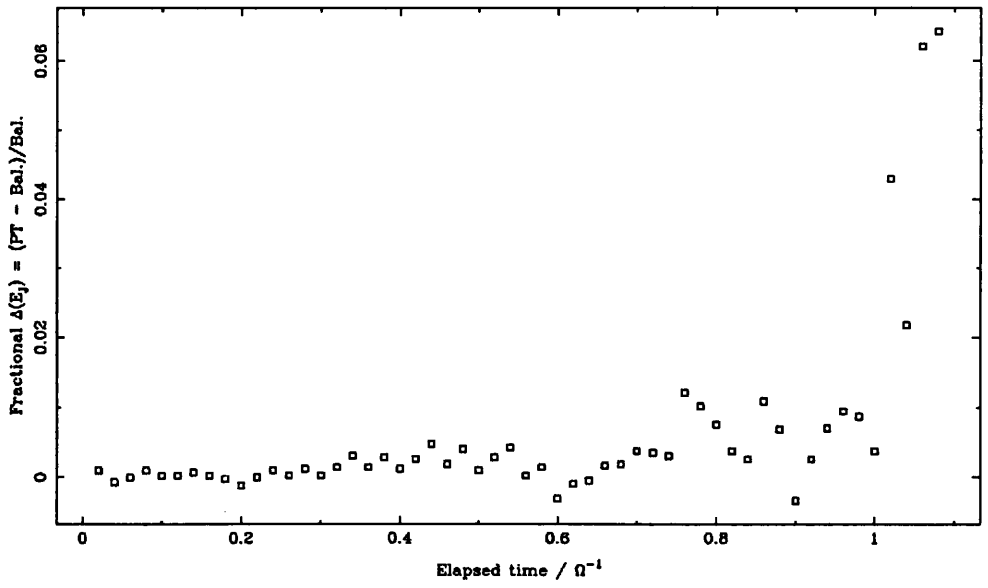

Figure I.6: *Fractional differences between the Jacobian energy calculations shown in figure I.2.*

a fixed amount in the y-direction (approximately perpendicular to the flow) at the end of each timestep. It was found that the displacement needed to bring this model into agreement with *both* the angular momentum and Jacobian energies of the PT models was only 5 % of the size of a PT grid-cell per timestep (see figures I.7 and I.8). That the shapes of both curves are accurately reproduced is strong evidence that these displacements are the cause of the non-conservation in the PT models. It is probable that this effect can be removed by retaining the positions of each particle at the end of the timestep (making it more like the particle-in-cell models of Lin and Pringle, 1976) but retaining the 'thermalizing' process of PT whereby the particles are still assigned new, randomly-generated velocities.

PT model runs with bursts of 1000 particles are impossible to interpret as there are particles in many different stages of infall at any one moment, smearing out the individual values for the interesting quantities.

I.2.2 Dissipation

Figure I.6 demonstrates that the Jacobian is conserved to within 6 % over the entire infall time of the test particle. For most of this time it is conserved to better than 1 %. This indicates that there is *no* significant anomalous generation of energy because of the numerical scheme employed.

Plots of the change in thermal energy against that in the mass-flow energy for each of 628 timesteps (e.g. figure I.9) show an axisymmetric distribution indicating that there is *no* systematic transfer of energy from one pool to the other. (The few outliers in figure I.9 are due to statistical fluctuations which leave zero particles in a grid cell).

Simulations using the PT scheme, of two supersonic flows colliding at right-angles show a very broad region of heating surrounding the impact region (see figures I.10 and I.11). Specifically, a region of greater width than would be expected from such a shock. Evidently, the heat energy is being dissipated very rapidly. When the timestep is reduced, this width decreases in some proportion, indicating that the

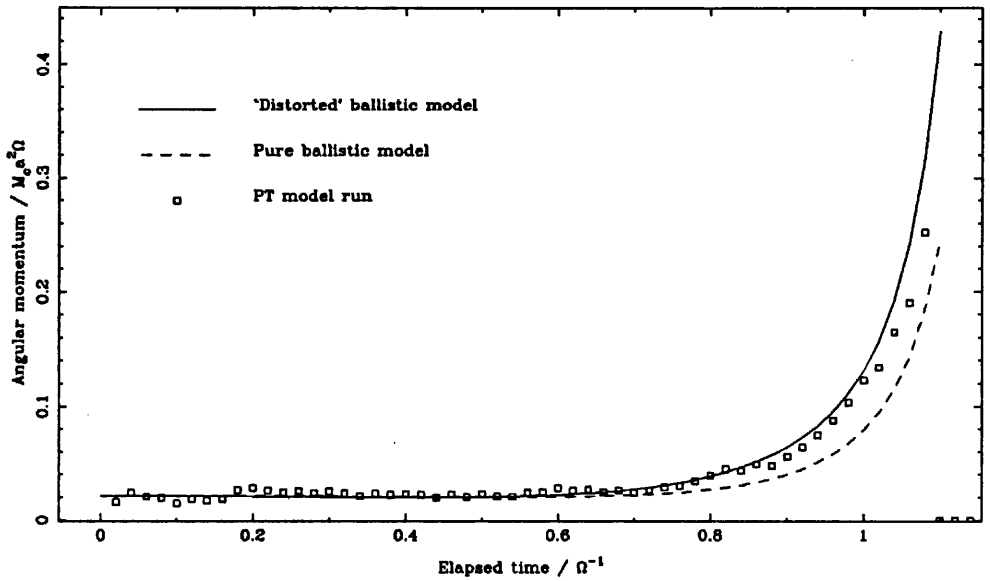

Figure I.7: *Reproduction of the PT angular momentum by small ($\lesssim 0.05\, l_{\rm cell}$) shifts each timestep.*

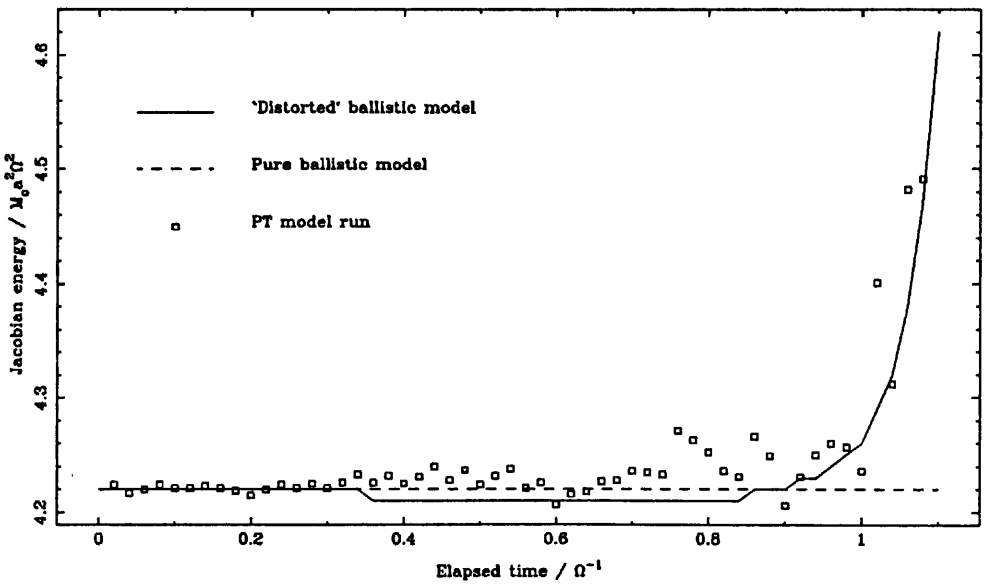

Figure I.8: *Reproduction of the PT Jacobian energy by small ($\lesssim 0.05\, l_{\rm cell}$) shifts each timestep.*

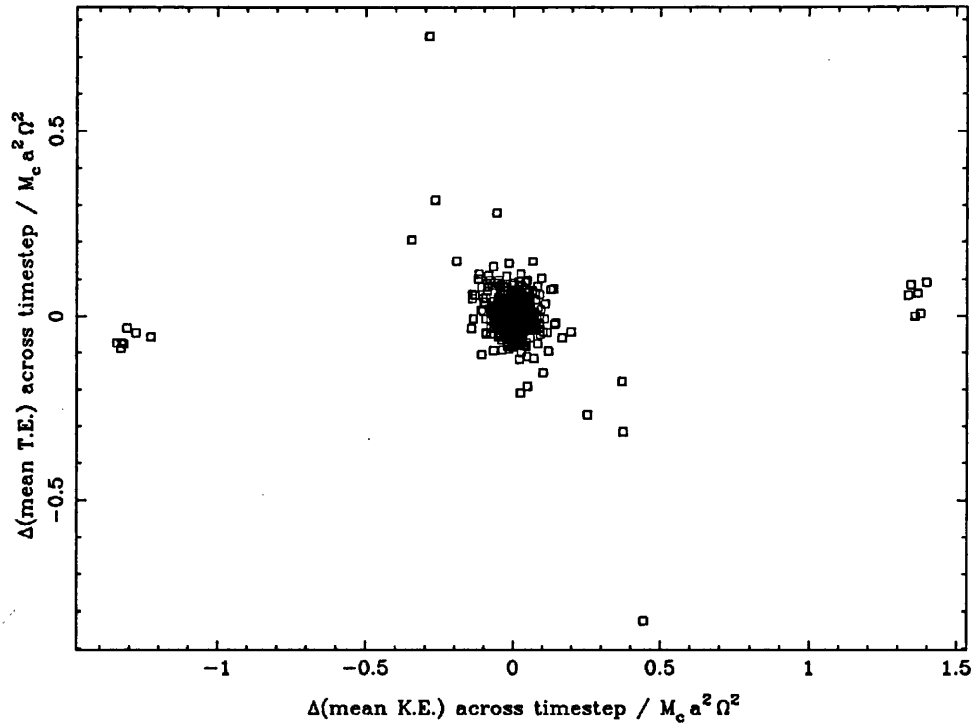

Figure I.9: *An example of the lack of correlation between the instantaneous energy changes in the mass flow and thermal pools.*

viscous transport is responsible.

In summary then, the cause of the rapid dissipation of shock heat observed in the PT scheme is large value of the viscosity which enables the energy to be easily transported over large distances, and *not* by a defect in the numerical scheme employed.

I.2.3 The nature and size of the PT viscosity

Careful consideration of the viscous process under the PT scheme reveals that the interaction has two characteristic scales instead of one (see figure I.12). Particles travelling with a speed greater than $v_{\rm crit} = l_{\rm cell}/\Delta t$ can transmit their local properties (i.e. energy and momentum) over distances $l = v\,\Delta t$. Particles whose speed is less than $v_{\rm crit}$ interact with all other particles within a range $l_{\rm cell}$. In reality, these two

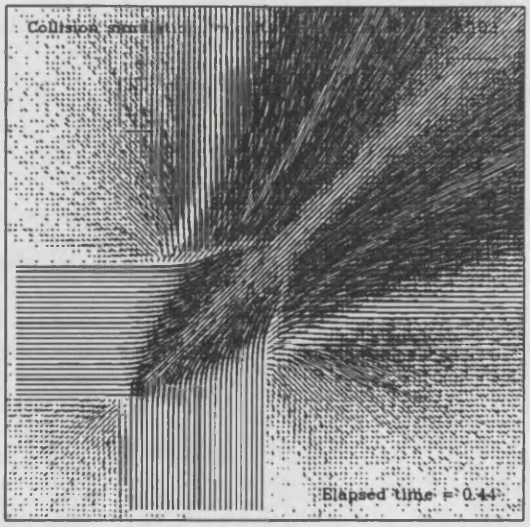

Figure I.10: *The simulated velocity structure of two supersonic jets colliding at right-angles.*

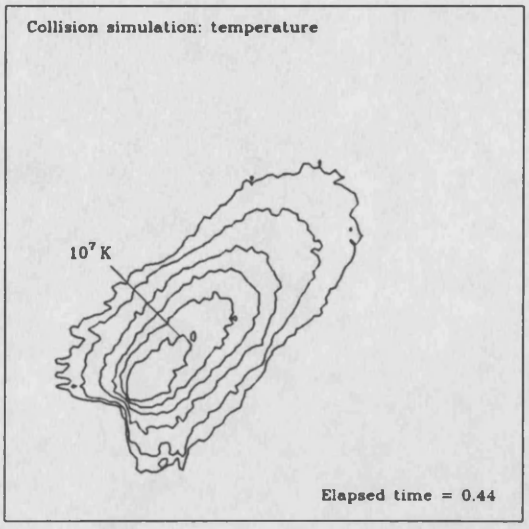

Figure I.11: *The temperature structure of the simulation in figure I.10. Note the large half-width produced by the high viscous dissipation.*

lengths are statistically equal to each; in the PT scheme, this can never be so. Thus in any one grid cell, there are particles which experience different values of the viscosity. The equivalent values of $\alpha = v\, l_{\rm visc}/c_{\rm s}\, H$ (cf. Shakura & Sunyayev, 1973) are typically 100 and 1 for $l_{visc} = v\Delta t$ and $l_{\rm cell}$ respectively, in the models considered here. The viscosity is therefore substantially supersonic.

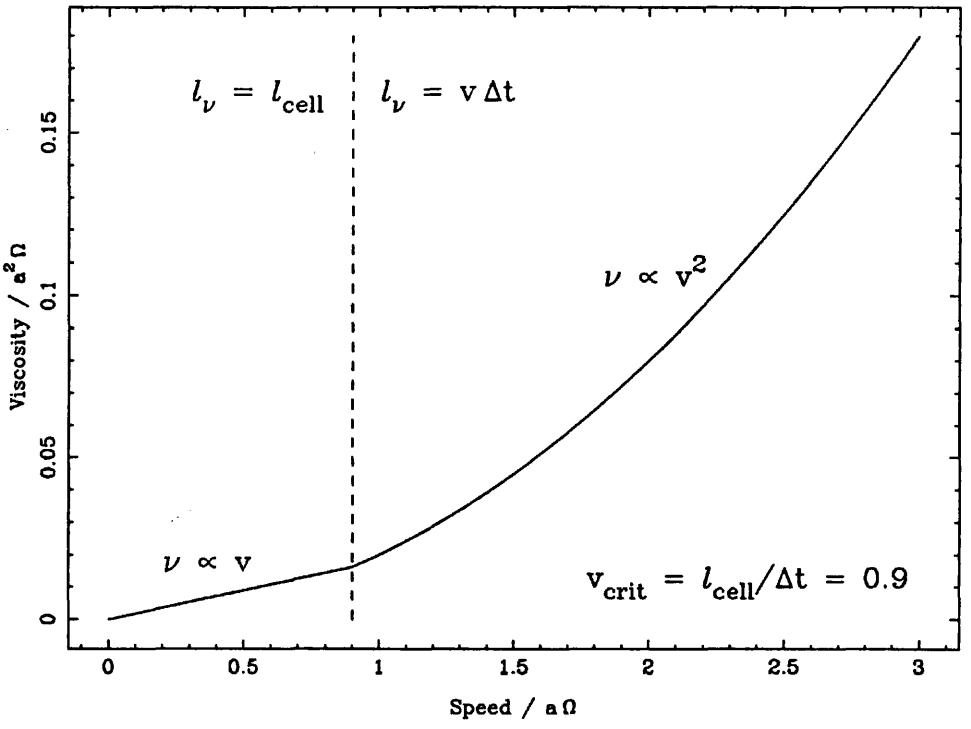

Figure I.12: *The viscosity experienced by a particle as a function of the its speed.*

The lower regime ($v < v_{\rm crit}$) is a consequence of the adopted mechanism for introducing viscosity, i.e. the imposition of a grid in order to 'bin' the particles. The upper regime is a consequence of using a constant timestep.

(Interestingly though, use of the PT scheme on flows *parallel or perpendicular to the grid axes,* makes the viscosity anisotropic. Consider the two components of a laminar flow moving rapidly along the x-axis. The speed in the x-direction is large and so the dominant viscous length is $v\Delta t$. Perpendicular to this, the speed is *much* smaller, a thermal value. This means that $l_{\rm cell}$ is the dominant length

in the y-direction. Consequently, altering Δt or $l_{\rm cell}$ independently will cause the viscosity to change parallel or perpendicular to the flow. It is for this reason that the stream contracts in width much more noticeably when $l_{\rm cell}$ is altered, than when Δt is changed).

In this case, as in all cases of astrophysical interest, the proposed viscosity is greater by many orders of magnitude than simple molecular viscosity, and, it should be stressed, as with all numerical viscosity schemes, the PT scheme is no more than a parameterization of an *unknown* physical process.

I.3 Discussion

In conclusion, the above tests indicate that the cause of the non-conservation of both angular momentum and energy is the fact that the particle positions are generated *randomly* from a distribution which becomes slightly skewed, and that the dissipation of the shock energy in the reconnecting stream is entirely ascribable to the large (supersonic) values of the viscosity which rapidly transport energy out of the shock region, and not to a correlation between the mass-motion and thermal energy changes.

This is in agreement with Whitehurst (private communication) who has found that the large timestep "impos[es] an implausibly efficient viscous transport mechanism." Comparative models constructed under a different numerical scheme (see Whitehurst R., 1988. *Mon. Not. R. Ast. Soc.*, **233**, 35 for details) indicate that the stream computed under the PT scheme *is* wider for the above reason although their performance at supersonic α-values could not be tested. It has been suggested (Whitehurst, private communication) that the only way to produce an escaping jet of material in the CX Dra system is to either begin with an overly-large stream at the Lagrangian point, or to have a smaller primary and a larger mass-ratio.

In their perturbation analysis, Lubow and Shu (1975) explicitly state that "...all matter-carrying streamlines must cross [the Roche surface] in an ϵ neighbourhood of L1." As ϵ is the local speed of sound, this is precisely equivalent to the calculation of

section I.1. Without postulating some *ad hoc* mechanism therefore, it is difficult to see how to achieve the desired widening the stream as it crosses the inner Lagrangian point.

The size of the primary is necessarily poorly-determined as CX Dra is a single-lined (non-eclipsing) spectroscopic binary, and only the mass function is known. Given Koubský's estimate of $M_1 = 7\,\mathrm{M}_\odot, r_1 = 4.60\,\mathrm{R}_\odot$, the fractional radius of the primary can be as small as 0.1353, a 10 % reduction on the value adopted in chapter 4, for an inclination of $i = 20°$. However, this inclination would result in a Q-U locus for CX Dra which is very nearly circular, flatly contradicting the observations (see figure 6.1). Allen (1973, p. 209) gives the radius of a B2.5 V Main Sequence star as $6.20\,\mathrm{R}_\odot$ which makes the problem worse. Even if CX Dra was mis-classified by a temperature sub-class (i.e. B3.5 V) this only brings r_1 down to $4.65\,\mathrm{R}_\odot$. In short, there seems no way to simultaneously reduce the size of the primary and increase the mass-ratio to the point where the stream can avoid complete accretion.

As the *IUE* observations strongly indicate that a streamer of material *is* escaping in the direction of motion of the primary, it appears that either some effect (e.g. magnetism) is deflecting the stream or the effective viscosity really is supersonic. The former option has been discussed fully in section 4.1.1 and must remain a possible solution, awaiting further evidence for or against it, whilst the latter may have an explanation in the following:

The inner 'edge' of the infalling stream will be travelling faster than the outer 'edge' because of the differing trajectories which they describe, and consequently, the stream will be shearing as it falls. Lubow and Shu (1975, table 3) calculate that the gradient of the flow speed across the stream (that is, normal to the flow) varies from 2 at the Lagrangian point to $\sim O(10)$ (in dimensionless units) as the stream approaches the primary. As the local sound speed, ϵ, is typically much less than unity and the stream width is of order ϵ, this implies that the shearing is supersonic. Under these conditions, it is highly probable that the flow will become turbulent (Landau & Lifshitz, 1959, *Fluid Mechanics*, § 30, p. 116) and "may be... described

as having a 'turbulent viscosity' $\nu_{\rm turb}$ which differs from the true kinematic viscosity ν." (ibid., p. 119). The ratio of these two coefficients is the Reynolds number of the flow, Re.

Taking $\nu_{\rm turb} \sim vL$ (where v and L are the characteristic speed and length scales of the turbulence) and using $\nu = \alpha c_{\rm s} H$, then

$$\mathrm{Re} = \frac{\nu_{\rm turb}}{\nu} = \frac{vL}{\alpha c_{\rm s} H}$$

or, rearranging,

$$\alpha\,\mathrm{Re} = \left(\frac{v}{c_{\rm s}}\right)\left(\frac{L}{H}\right) \equiv \alpha_{\rm turb}$$

implying that the viscosity that is deduced from observations is the turbulent viscosity, and is greater than the true kinematic viscosity a factor equal to the Reynolds number of the flow.

In fully-turbulent flows, the Reynolds number is much greater than 10^3–10^4. This means that if the viscosity required to produce an escaping streamer in CX Dra is due to turbulence and is of the order of $\alpha_{\rm turb} \sim 100$, it is still possible to have the true kinematic viscosity parameter $\alpha < 1$. Thus, the problem of a supersonic viscosity is overcome by allowing for the fact that the flow is unlikely to be laminar (Re = 1). Such a reduction in the value of the true kinematic viscosity is, of course, applicable to all situations where turbulence may be the dominant source of viscosity (e.g. CVs).

I.4 Conclusions

Given the possibility that the stream is supported by some as yet unquantifiable process instead of possessing a supersonic viscosity, and hence that the mass-distribution derived in chapter 4 may be too broad, it is important to consider the implications of a thinner stream for the results of chapters five and six.

The most important part of the stream in determining the fit of synthetic profiles

and polarization data to the observations is the dense, central core of the infalling stream. This region deviates little from the Lubow and Shu pseudo-ballistic solution and so any results are likely to be affected in only two ways.

Firstly, the extra width of the stream will contribute more slow-moving material to the synthetic profile. Its removal may make the synthetic profile slightly more shallow, requiring a greater abundance and/or a larger inclination to produce a better fit to the observations. This effect is expected to be minimal as the fraction of slow-moving material in the stream is small.

Secondly, the greater width (but *not* height) of the stream will serve to increase the estimate of the Lagrangian mass-loss rate by a factor of approximately 2. The Q-U loci are dominated by the values of the shape factors γ_3 and γ_4. If the stream shrinks in width, the former will increase slightly and the latter will be reduced. This makes the computed Q-U loci more circular and the variations of smaller amplitude. The net effect (once the mass loss rate is corrected for) will be a slightly worsened fit in the case of Algol and a slightly higher derived inclination for CX Dra to allow for these changes.

Finally then, the *IUE* observations of CX Dra strongly favour the presence of a stream escaping the system at phase $\phi \sim 0.3$. If it is assumed that the *infalling* part of the stream is of low viscosity and only escapes past the primary by virtue of an unknown mechanism, then the results of chapters five and six are altered to the extent that a small increase in the derived abundances should be expected and the mass loss rate at the Lagrangian point should be approximately doubled. However, it is possible to account for the observations once it is realised that the viscosity is not due to the 'standard' kinematic processes but is due to turbulence in the flow. Inherent in the assumption of $\alpha < 1$ is the further assumption that the flow is laminar. This is an extremely unlikely situation, and its rejection enables the viscosity to be greater by a factor exceeding 10^3, bringing it into a regime which is modelled well by the PT scheme (once the anomalous angular momentum generation is removed).